

FETCH-MIPS
A Coupled Computational Multiphase Flow and Neutron-Radiation
Transport Model

**Phase II: Theory and application of the FETCH-MIPS model to
coupled behavior of MIPS-type reactor systems with boiling fissile
solutions**

Imperial Consultants

Project No:

EA01050

The Babcock & Wilcox Company

PO Number:

4900004624-4

Date:

Dec 2012

Author:

C.C. Pain, J.L.M.A. Gomes, A. Buchan,
M.D. Eaton, A.J.H. Goddard, G.J. Gorman,
D. Pavlidis, M.M.R. Williams
Applied Modelling and Computation Group
Department of Earth Science and Engineering
Imperial College, London

Contract Manager:

Ms Christine Ung

Executive Summary

This draft Topical Report, by Imperial College London's (ICL) consultancy ICON Ltd, is produced so that B&W may consider its suitability for review, by the United States Nuclear Regulatory Commission (NRC) of the Imperial College computer model FETCH-MIPS, for research and design of MIPS-related reactor systems. FETCH-MIPS is a 'virtual reactor' 2D/3D transient coupled model for fissile solution reactors with within-vessel cooling coils and control rods and is fundamentally-based as far as is feasible. The report presents work on establishing a boiling modelling capability within the FETCH-MIPS model. This report is one of six Reports:

- (i) A Description of the FETCH-MIPS code for 'virtual reactor' modelling of fissile solution reactors of the MIPS type.
- (ii) Justification for SUPO as a Modelling Benchmark and Demonstration of the Application of the FETCH-MIPS Code to the SUPO reactor.
- (iii) Demonstration application of the FETCH-MIPS code to coupled steady-state and transient behaviour of MIPS-type reactor systems.
- (iv) Neutronics aspects of the FETCH-MIPS code for modelling MIPS-type reactor systems.
- (v) Three-dimensional Simulations of the Medical Isotope Production System (MIPS) using the FETCH code.
- (vi) Phase II: Theory and application of the FETCH-MIPS model to coupled behaviour of MIPS-type reactor systems with boiling fissile solutions.

Contents

1	Introduction	8
1.1	Report aims	8
1.2	Physics of fissile solutions with cooling coil heat extraction	8
1.2.1	Formation of radiolytic gases	8
1.2.2	Physics of radiolytic gas and vapour bubbles	8
1.2.3	Immersed surfaces and nucleation	9
1.2.4	Fissile liquid-cooling coil heat transfer coefficient and effect on power	9
1.3	Report contents	10
2	Two-Fluid Model Equations for Boiling	11
2.1	Conservation of mass	11
2.2	Conservation of momentum	11
2.3	Internal energy conservation	13
2.3.1	Equations for implicit treatment of temperature	14
2.3.2	Calculating both temperature and internal energy in general	16
2.4	The Multi-component Flow Submodel	17
2.4.1	The Gas Phase Multi-Components	17
2.4.2	Radiolytic gas modelling	19
2.4.3	Radiolytic gas bubble modelling and parameterizations of rate of radiolytic gas production	19
3	Parameterizations for Multi-Phase Fluid Exchanges with Boiling	22
3.1	Multi-phase energy exchange	23
3.2	Interface mass and heat transfer	23
3.2.1	Simple expression for vapour production/condensation	23
3.2.2	Interface Stefan condition for mass transfer from heat transfer	23
3.2.3	Implementation of heat exchange due to vapourization/condensation	24
3.2.4	Heat transfer for liquid-vapour in bubbly flows	26
3.2.5	Vapour generation/condensation in the presence of non-condensable radiolytic gases	27
4	Comparison of FETCH-MIPS and RELAP equations and parameterizations	28
4.1	Motivation for use of RELAP models within FETCH	28
4.2	Internal energy equations	28
4.3	Momentum equations	29
4.4	Heat and mass transfer parameterizations	29

5 Modelling Results with Boiling	30
5.1 Volumetric boiling experiments	30
5.2 CRAC geometry homogeneous boiling simulations with netronics coupling	34
5.2.1 Time variation graphs	34
5.2.2 Snapshots of spatial distributions	40
5.3 CRAC 43 simulation with boiling	56
5.3.1 Bubbles	56
5.3.2 Dynamics	56
5.3.3 Advection processes	57
5.3.4 Free surface waves	57
5.4 440kW MIPS simulation with boiling	63
5.4.1 RZ MIPS configuration	63
5.4.2 Time variation graphs	65
5.4.3 Snapshots of pipe water temperature for the MIPS reactor	76
5.4.4 Snapshots of spatial distributions of the MIPS reactor	81
5.5 FETCH-MIPS applied to a postulated accident	93
6 Conclusions	96

List of Tables

List of Figures

1	Parameterization of saturation vapour temperature against pressure.	30
2	Volume fraction of vapour versus time. MMR Williams (2011) [1] theory and Greenfield et al (1954) experiments in which red circles = the experiment with 17.1kW and black circles= the experiment with 4.8kW. The FETCH-MIPS vapour fraction is taken at 12.5 cm height.	32
3	Maximum temperature versus time for FETCH-MIPS and the two volumetric heating experiments performed by Greenfield et al (1954).	33
4	Power versus time for varying step reactivities and for the CRAC 38 geometry and solution.	35
5	Maximum liquid temperature versus time for varying step reactivities and for the CRAC 38 geometry and solution.	36
6	Maximum pressure deviation from atmospheric pressure versus time for varying step reactivities and for the CRAC 38 geometry and solution.	37
7	Maximum liquid velocity versus time for varying step reactivities and for the CRAC 38 geometry and solution.	38
8	Maximum gas velocity versus time for varying step reactivities and for the CRAC 38 geometry and solution.	39
9	For the 1.9\$ step reactivity insertion and CRAC geometry and solution the snapshots of volume fraction at various instances in time.	41
10	For the 1.9\$ step reactivity insertion and CRAC geometry and solution the snapshots of liquid temperature at various instances in time.	42
11	For the 1.9\$ step reactivity insertion and CRAC geometry and solution the snapshots of normalized vapour concentration at various instances in time.	43
12	For the 1.9\$ step reactivity insertion and CRAC geometry and solution the snapshots of normalized radiolytic gas in gas phase concentration at various instances in time.	44
13	For the 1.9\$ step reactivity insertion and CRAC geometry and solution the snapshots of liquid velocity and volume fraction at various instances in time.	45
14	For the 2.1\$ step reactivity insertion and CRAC geometry and solution the snapshots of volume fraction at various instances in time.	46
15	For the 2.1\$ step reactivity insertion and CRAC geometry and solution the snapshots of liquid temperature at various instances in time.	47
16	For the 2.1\$ step reactivity insertion and CRAC geometry and solution the snapshots of normalized vapour concentration at various instances in time.	48
17	For the 2.1\$ step reactivity insertion and CRAC geometry and solution the snapshots of normalized radiolytic gas in gas phase concentration at various instances in time.	49

18	For the 2.1\$ step reactivity insertion and CRAC geometry and solution the snapshots of liquid velocity and volume fraction at various instances in time.	50
19	For the 2.3\$ step reactivity insertion and CRAC geometry and solution the snapshots of volume fraction at various instances in time.	51
20	For the 2.3\$ step reactivity insertion and CRAC geometry and solution the snapshots of liquid temperature at various instances in time.	52
21	For the 2.3\$ step reactivity insertion and CRAC geometry and solution the snapshots of normalized vapour concentration at various instances in time.	53
22	For the 2.3\$ step reactivity insertion and CRAC geometry and solution the snapshots of normalized radiolytic gas in gas phase concentration at various instances in time.	54
23	For the 2.3\$ step reactivity insertion and CRAC geometry and solution the snapshots of liquid velocity and volume fraction at various instances in time.	55
24	Left: K_{eff} against temperature - just the neutron temperature effect and the total effect (including density changes with temperature assuming atmospheric pressure) on K_{eff} of temperature changes. Right: K_{eff} against fissile liquid height at atmospheric pressure and a temperature of 20 Deg. C.	59
25	Fission power versus time for the CRAC 43 experiment taken from T. SCHULENBERG and J. DOHLER 1986 [2]	60
26	Fission power versus time for the CRAC 43 experiment taken from T. SCHULENBERG and J. DOHLER 1986, [2].	61
27	Temperature Deg. C. versus time for the CRAC 43 experiment taken from T. SCHULENBERG and J. DOHLER 1986, [2]. The position of the temperature measurement is indicated in the cylinder.	62
28	Geometry of the MIPS reactor used in the FETCH-MIPS model. Dark Blue: fuel solution; Red: gas; Yellow: Graphite; Light Blue: Water Reflector; Grey: Control rods	64
29	Power versus time for the MIPS reactor.	66
30	Maximum liquid temperature versus time for the MIPS reactor.	67
31	Maximum normalized vapour concentration versus time for the MIPS reactor.	68
32	Maximum normalized radiolytic gas concentration in the gas phase versus time for the MIPS reactor.	69
33	Water pipe outlet temperature and water mean temperature versus time for the MIPS reactor.	70
34	Mean heat transfer coefficient with the pipe versus time for the MIPS reactor.	71
35	Control rod tip position (distance of tip from the base of the fluid filled cavity of MIPS) versus time. The control rod comes in from the top of the reactor.	72
36	Maximum pressure versus time for the MIPS reactor.	73

37	Maximum liquid and gas velocity versus time for the MIPS reactor.	74
38	Automatic time step size versus time for the MIPS reactor.	75
39	Water temperature in each of the 12 cooling coil pipes versus distance along each pipe for the MIPS reactor at t=150 seconds.	77
40	Water temperature in each of the 12 cooling coil pipes versus distance along each pipe for the MIPS reactor at t=200 seconds.	78
41	Water temperature in each of the 12 cooling coil pipes versus distance along each pipe for the MIPS reactor at t=250 seconds.	79
42	Water temperature in each of the 12 cooling coil pipes versus distance along each pipe for the MIPS reactor at t=280 seconds.	80
43	Snapshots of liquid volume fraction at various instances in time for the MIPS reactor with boiling.	82
44	Snapshots of liquid volume fraction at various instances in time for the MIPS reactor with boiling.	83
45	Snapshots of liquid temperature (close to the gas temperature) at various instances in time for the MIPS reactor with boiling. The temperature of the legend has been limited to between 95 Deg and the maximum temperature over the last 20 seconds of the simulation.	84
46	Snapshots of liquid temperature (close to the gas temperature) at various instances in time for the MIPS reactor with boiling. The temperature of the legend has been limited to between 95 Deg and the maximum temperature over the last 20 seconds of the simulation.	85
47	Snapshots of maximum normalized concentration of vapour (akin to vapour volume fraction) at various instances in time for the MIPS reactor with boiling.	86
48	Snapshots of maximum normalized concentration of vapour (akin to vapour volume fraction) at various instances in time for the MIPS reactor with boiling.	87
49	Snapshots of maximum normalized radiolytic gas concentration (akin to radiolytic gas volume fraction) in the gas phase at various instances in time for the MIPS reactor with boiling.	88
50	Snapshots of maximum normalized radiolytic gas concentration (akin to radiolytic gas volume fraction) in the gas phase at various instances in time for the MIPS reactor with boiling.	89
51	Snapshots of liquid velocity as well as liquid volume fraction at various instances in time for the MIPS reactor with boiling.	90
52	Snapshots of liquid velocity as well as liquid volume fraction at various instances in time for the MIPS reactor with boiling.	91

53	Snapshots of delayed neutron precursor concentration at t=27.9 s for the MIPS reactor with boiling. Delayed group 1 has a half life of 55 seconds and delayed group 6 has a half life of 0.2 seconds. The shortest lived delayed group 6 shows the power distribution in the reactor.	92
54	Snapshots of liquid volume fraction at various instances in time for the MIPS reactor and with boiling with a large reactivity insertion applied during 'steady' conditions.	94
55	Snapshots of liquid volume fraction at various instances in time for the MIPS reactor and with boiling with a large reactivity insertion applied during 'steady' conditions.	95

1 Introduction

1.1 Report aims

This report extends the MIPS reactor model using the newly developed FETCH-MIPS model to include boiling. Detailed spatial resolution modelling has been performed here (albeit in RZ coordinates) using FETCH-MIPS in order to gain confidence in the results and resolve much of the physics.

Fissile solutions with internal fission heating are challenging to understand, and model, because of the complex multi-phase flow and heat transfer physics involved which may include boiling.

This report develops a modelling method for boiling and demonstrates its abilities with some applications. The model is based on a multi-fluid approach, in which one phase represents the liquid, and the second phase the gas phase which includes radiolytic gases, vapour and air. In each fluid phase a set of conservation equations for mass, energy and momentum are solved with appropriate interphase exchange terms coupling the fluid phases.

1.2 Physics of fissile solutions with cooling coil heat extraction

Here the physics of fissile solutions with cooling coil heat extraction is discussed. This includes: the formation mechanism of radiolytic gases; the physics of radiolytic gas and vapour bubbles; immersed surfaces and nucleation; and fissile liquid-cooling coil heat transfer coefficient and effect on power.

1.2.1 Formation of radiolytic gases

For every fission event a certain quantity of heat energy and radiolytic gases are generated. The energetic fission fragments split up some of the liquid molecules to form radiolytic gases. Although the energy deposited with fission is deposited in a small region with large temperatures and pressures (if continuum mechanics are valid) this quickly dissipates. The radiolytic gases are dissolved in the solution due to the surface tension forces quickly collapsing any micro-bubbles. However, micro-bubbles generated larger than a certain size may grow to produce radiolytic gas bubbles of the order of 0.4mm in diameter. This expansion occurs on a very short time-scale on the order of 1.0×10^{-5} seconds. The expansion or collapse of micro-bubbles depends on the concentration of dissolved radiolytic gases, which provides a diffusion process of dissolved radiolytic gas concentration via Brownian motion, through the concentration boundary layer around the bubble and into it. This critical concentration is generally determined via Henry's law and depends on the local pressure and temperature of the solution.

1.2.2 Physics of radiolytic gas and vapour bubbles

For slow transients it is generally a good approximation to assume that any concentration of deposited radiolytic gases appears in bubble form instantly. However, for more rapid transients, with short

time scales of the order of 0.1 seconds or less, the rate at which radiolytic gas bubbles is formed in the solution can become very important. For low fission rate densities, since the micro-bubbles are produced along fission fragment tracks, this rate of production of radiolytic gases can be assumed proportional to the fission rate. However, for rapid transients the fission rate density is high and there is a complex interaction between the fission fragment wakes and the micro-bubbles, e.g., the fission fragments may break up micro-bubbles before they can expand. Since this process has largely unquantified physics it is generally parametrised by using experimental data. This is the approach taken in the FETCH-MIPS model. When boiling occurs the radiolytic gas bubbles can provide the nucleation sites for the generation of vapour or mixed vapour-radiolytic gas bubbles. Thus, there is a complex relationship between the interaction of radiolytic gases and vapour. For example the reduction if the concentration of vapour in bubbles, due to the presence of radiolytic gases, provides an diffusion inhibiting mechanism, within the bubbles, which suppresses both the rate of heat and mass transfer of vapour too and from bubbles. This rate of radiolytic gas and vapour gas production is important because it determines the negative reactivity feedback associated with gas production which can be a dominant effect in, for example, step reactivity insertions.

1.2.3 Immersed surfaces and nucleation

The bubbles may also be nucleated on immersed surfaces, such as cooling coils or containers, as the imperfections in the surfaces form very small cavities which trap gases and in which radiolytic gas or vapour bubbles can be nucleated. This is referred to as heterogeneous nucleation of bubbles and the nucleation within the body of the fissile solution homogeneous nucleation. The case of solution boiling away from the internal structures (the case examined here) is referred to as homogeneous boiling and is the focus of the attention here as boiling is suppressed around the immersed cooling coils due to the fact that they cool the solution locally and is thus ignored. We have also examined the role of immersed surface for the nucleation rate of radiolytic gas bubbles in a previous report and due to the fact that this rate has not been found to be important in steady state conditions as once the solution becomes supersaturated with radiolytic gases all subsequent radiolytic gas appears in bubble form and is relatively rapid.

1.2.4 Fissile liquid-cooling coil heat transfer coefficient and effect on power

The bubbles often provide the dominant buoyancy forces which move the fissile solution. They will also rise out of the solution with slip velocities between the solution and the bubbles. Eventually, they will rise out of the solution but, they may become trapped, due to the turbulence of the fissile solution.

The speed of the solution past the cooling coils provides a dominant mechanism for increasing heat transfer between the cooling coils and the fissile solution. Thus, heat transfer coefficients are often increased in the presence of radiolytic gas and vapour bubbles, as their resulting buoyancy forces moves

the liquid relatively quickly. Thus, if there is a rapid transient with fast moving solution (e.g., generated as a result of a step reactivity insertion) then there will be a relatively large heat transfer coefficient, although the time scales on which this operates can be small, which will effect the heat transfer to the cooling water in the helicoidal pipe system. The cooling water will generally heat up as it passes through the cooling coils, as often the water will be cooler than the fissile solution surrounding the cooling coils. Although the dissipating temperature and liquid velocities are highly non-uniform, the cooling water temperature often increases approximately linearly with distance along the pipes. This linear behaviour is reduced however, when the temperature of the cooling coil water approaches that of the fissile liquid, simply because the heat transfer rate is locally proportional to $h(T_l - T_w)$ in which h is the heat transfer coefficient. Eventually, when the system reaches steady state the heat energy extracted by the cooling coils plus the energy losses (e.g., to the surrounding and evaporation) will be balanced by the fission heat energy.

Thus, given the heat transfer coefficient of the system, very simple models can be constructed to help us understand the heat transfer mechanisms (e.g. the analytical model developed in previous FETCH-MIPS reports). However, the heat transfer coefficient determination is complex and requires detailed modelling that can only be provided by the FETCH-MIPS model.

1.3 Report contents

We first present the modelling method; both the conservation equations and constitutive equations used to parameterize the coupling between the fluid phases. Results from a benchmark boiling experiments is then presented for validation. Followed by the application to fissile solutions in cylinders with step reactivity insertions to explore the basic physics of boiling within fissile solutions. This is followed by the application of FETCH-MIPS to model the French CRAC 43 criticality experiment which had solution boiling. This is followed by application to the MIPS system for 'steady conditions' and a 440kW power output and its application to a postulated accident scenario.

2 Two-Fluid Model Equations for Boiling

In this section we present the governing multi-phase fluid equations and modelling assumptions, see [3],[4]. The basic assumption is that the system can be modelled using a two-fluid model, one-phase representing liquid and the second phase representing steam. Gas phase is assumed to be compressible and behaves as an ideal gas and the liquid phase is slightly compressible. For liquid-gas systems here the gas phases (radiolytic gases-hydrogen-, air/nitrogen, steam) are lumped together and modelled as one fluid phase.

2.1 Conservation of mass

The continuity equations for phase k are expressed by

$$\frac{\partial}{\partial t} (\alpha_k \rho_k) + \nabla \cdot (\alpha_k \rho_k v_k) = - \sum_{k'} (G_{kk'} - G_{k'k}) = \sum_{k'} \Gamma_{kk'} = \Gamma_k \quad (1)$$

in which $\Gamma_{kk'} = -(G_{kk'} - G_{k'k})$ and where α_k is the volume fraction of phase k , v_k is velocity of phase k . The subscripts k in the equation above refer to each of the fluid phases, i.e. when subscripts $k = l$ indicate the liquid phase and $k = g$ indicates the gas phase. The subscript k' is attached to variables associated with the phase other than the phase k in two phase flow. Here $G_{kk'}$ is the mass transfer from phase k to k' .

Air, hydrogen and steam are assumed to behave as ideal gases, i.e.,

$$\rho_{gc} = \frac{MW_{gc}}{R} \frac{p_g}{T_g} \quad (2)$$

where MW_{gc} , R , p_g and T_g are the molecular weight for gas component c , universal gas constant, gas pressure and temperature, respectively. The density of the liquid phase is defined as

$$\rho_l = \rho_0 + \frac{1}{\bar{c}^2} (p - p_0) + \beta_{l,exp} (T_l - T_0) \quad (3)$$

where \bar{c} is the isentropic sonic speed and $\beta_{l,exp}$ is the liquid expansion coefficient.

2.2 Conservation of momentum

The momentum equation is expressed by,

$$\begin{aligned} \frac{\partial}{\partial t} (\alpha_l \rho_l v_l) + \nabla \cdot (\alpha_l \rho_l v_l v_l) &= -\alpha_l \nabla p + \nabla \cdot (\tau_l) \\ &\quad + \alpha_l \rho_l g + \Sigma_{drag} (v_g - v_l) + \Gamma_l v_l^I + S_{ul}, \end{aligned} \quad (4)$$

$$\begin{aligned} \frac{\partial}{\partial t} (\alpha_g \rho_g v_g) + \nabla \cdot (\alpha_g \rho_g v_g v_g) &= -\alpha_g \nabla p + \nabla \cdot (\tau_g) \\ &\quad + \alpha_g \rho_g g + \Sigma_{drag} (v_l - v_g) + \Gamma_g v_g^I + S_{ug}, \end{aligned} \quad (5)$$

where Σ_{drag} is the inter-facial drag coefficient, p is the shared pressure of all phases; g is the gravitational acceleration, τ_k is viscous stress tensor. The terms $\Gamma_l v_l^I, \Gamma_g v_g^I$ represent the change of momentum due to phase change in which v_l^I, v_g^I are the averaged velocities of the liquid-vapour/gas interface. In non-conservative form the momentum equations become (using the continuity equation 1):

$$\begin{aligned} \alpha_l \rho_l \left(\frac{\partial}{\partial t} v_l + v_l \cdot \nabla v_l \right) &= -\alpha_l \nabla p + \nabla \cdot (\tau_l) \\ &+ \alpha_l \rho_l g + \Sigma_{drag} (v_g - v_l) + \Gamma_l (v_l^I - v_l) + S_{ul}, \end{aligned} \quad (6)$$

$$\begin{aligned} \alpha_g \rho_g \left(\frac{\partial}{\partial t} v_g + v_g \cdot \nabla v_g \right) &= -\alpha_g \nabla p + \nabla \cdot (\tau_g) \\ &+ \alpha_g \rho_g g + \Sigma_{drag} (v_l - v_g) + \Gamma_g (v_g^I - v_g) + S_{ug}. \end{aligned} \quad (7)$$

The viscous stress tensor is given by

$$\tau_k = \mu_k \frac{1}{2} [\nabla v_k + (\nabla v_k)^T] \quad (8)$$

where the superscript 'T' denotes the transpose of ∇v_k . A constant viscosity μ_k is only applicable when the volume fraction α_k is near unity and phase k is continuous and well connected. When it is not, it is assumed, for simplicity, that $\mu_k = \alpha_k \mu_k^*$ for some constant μ_k^* which is a parameterization of viscosity, it is in effect an eddy viscosity. The liquid-vapour interface velocities v_l^I, v_g^I will be approximated by $v_l^I = v_l, v_g^I = v_g$ in this work. However, although common practice [5, 6], it should be pointed out that this results in a non-conservative contribution to momentum since on summation of the momentum exchange terms in the conservation equations 5 the result is not zero. It is normally assumed that the drag terms sum to zero and, in fact, most of the correlations for drag determined in the literature have been developed with that assumption, so its difficult to use anything else. However, conservation requires the summation over phases of both the drag and interface momentum exchange due to phase change equal zero (assuming for the time being they are the only momentum exchange terms or more likely that the other momentum exchange terms sum to zero separately). Choosing a single interface velocity $v^I = v_l^I = v_g^I$ is a way to achieve conservation of the phase change term individually, that is $\Gamma_l v^I + \Gamma_g v^I = -\Gamma_g v^I + \Gamma_g v^I = 0$. Some choices of interface velocity are: the mean velocity $v^I = \frac{1}{2}(v_l^I + v_g^I)$; mass weighted average $v^I = \frac{1}{\alpha_l \rho_l + \alpha_g \rho_g} (\alpha_l \rho_l v_l + \alpha_g \rho_g v_g)$; expansion weighting $v^I = v_l$ if $\Gamma_g \geq 0$ else $v^I = v_g$. The latter and $v_l^I = v_l, v_g^I = v_g$ have been found to result in stable schemes in FETCH-MIPS.

2.3 Internal energy conservation

The equations for internal energy (e_l, e_g) balance of the liquid and gas phases, in conservative form, are:

$$\begin{aligned} \left(\frac{\partial}{\partial t} (\alpha_l \rho_l e_l) + \nabla \cdot v_l \alpha_l \rho_l e_l \right) &= \nabla \cdot (\alpha_l \kappa_l \nabla \cdot T_l) - p \left(\frac{\partial \alpha_l}{\partial t} + \nabla \cdot \alpha_l v_l \right) \\ &+ \Sigma_{rad} (T_g - T_l) + \Sigma_{vap_l} (T_s - T_l) + \Gamma_{lv} h_l^I + \Omega_{wl} + S_l, \end{aligned} \quad (9)$$

$$\begin{aligned} \left(\frac{\partial}{\partial t} (\alpha_g \rho_g e_g) + \nabla \cdot v_g \alpha_g \rho_g e_g \right) &= \nabla \cdot (\alpha_g \kappa_g \nabla \cdot T_g) - p \left(\frac{\partial \alpha_g}{\partial t} + \nabla \cdot \alpha_g v_g \right) \\ &+ \Sigma_{rad} (T_g - T_l) + \Sigma_{vap_g} (T_s - T_g) + \sum_{c=1}^3 \Gamma_{gc} h_{gc}^I + \Omega_{wg} + S_g, \end{aligned} \quad (10)$$

It will be convenient to write:

$$e_l = \bar{e}_l + \hat{e}_l, \quad e_g = \bar{e}_g + \hat{e}_g, \quad (11)$$

in which the interface values of the enthalpies are h_l^I and h_{gc}^I (here it is assumed $h_l^I = h_l^s$ and $h_{gc}^I = h_{gs}^s$, that is the saturation values of the liquid and gas enthalpies) for the liquid and gas components and \bar{e}_l, \bar{e}_g are invariant constants which set the internal energy level. These are arbitrary up to a point of enabling one of these to be set to any value. Here $\bar{e}_g = 0$. The mass transfer to the liquid due to vapour condensation or vapour production is Γ_{lv} . The term $\Sigma_{rad} (T_g - T_l)$ is the heat exchange between the liquid and the radiolytic gases and $\Sigma_{vap_l} (T_s - T_l)$ is the heat exchange between the liquid and the vapour-liquid interface and $\Sigma_{vap_g} (T_s - T_g)$ the heat exchange between the gas and the vapour-liquid interface in which the interface is assumed to be at the saturation temperature T_s . The index c identifies the gas component being considered: air, radiolytic gases (hydrogen) or vapour.

Using the latent heat definition:

$$L_e(T_s) = e_g(T_s) - e_l(T_s) \quad (12)$$

in which L_e is the latent heat expressed in terms of the difference in internal energies between the vapour/gas and liquid phases as opposed to the commonly used latent heat definition of the difference between enthalpies:

$$L_h(T_s) = h_g(T_s) - h_l(T_s) = (e_g(T_s) + \frac{p_s}{\rho_{g_s}}) - (e_l(T_s) + \frac{p_s}{\rho_{l_s}}) \quad (13)$$

$$= L_e(T_s) + \frac{p_s}{\rho_{g_s}} - \frac{p_s}{\rho_{l_s}} \quad (14)$$

in which p_s, T_s are the saturation temperatures and pressures. Equation 12 is satisfied for any any matching set p_s, T_s e.g. p_{s0}, T_{s0} , thus:

$$L_e(T_{s0}) = e_g(T_{s0}) - e_l(T_{s0}) \quad (15)$$

and from equations 11:

$$L_e(T_{s0}) = \hat{e}_g(T_{s0}) - \bar{e}_l - \hat{e}_l(T_{s0}), \quad (16)$$

and thus:

$$\bar{e}_l = -L_e(T_{s0}) - \hat{e}_g(T_{s0}) - \hat{e}_l(T_{s0}) = -L_{e0}, \quad (17)$$

which provides a definition of L_{e0} . Using this definition of \bar{e}_l the thermal energy equations become:

$$\begin{aligned} \left(\frac{\partial}{\partial t} (\alpha_l \rho_l \hat{e}_l) + \nabla \cdot v_l \alpha_l \rho_l \hat{e}_l \right) &= \nabla \cdot (\alpha_l \kappa_l \nabla \cdot T_l) - p \left(\frac{\partial \alpha_l}{\partial t} + \nabla \cdot \alpha_l v_l \right) \\ &\quad + \Sigma_{rad}(T_g - T_l) + \Sigma_{vap_l}(T_s - T_l) \\ &\quad + \Gamma_{lv} h_l^s + \Gamma_l L_{e0} + \Omega_{wl} + S_l, \end{aligned} \quad (18)$$

$$\begin{aligned} \left(\frac{\partial}{\partial t} (\alpha_g \rho_g \hat{e}_g) + \nabla \cdot v_g \alpha_g \rho_g \hat{e}_g \right) &= \nabla \cdot (\alpha_g \kappa_g \nabla \cdot T_g) - p \left(\frac{\partial \alpha_g}{\partial t} + \nabla \cdot \alpha_g v_g \right) \\ &\quad + \Sigma_{rad}(T_l - T_g) + \Sigma_{vap_g}(T_s - T_g) \\ &\quad + \sum_{c=1}^3 \Gamma_{gc} h_{gc}^s + \Omega_{wg} + S_g, \end{aligned} \quad (19)$$

Equation 19 in non-conservative form:

$$\begin{aligned} \alpha_l \rho_l \left(\frac{\partial}{\partial t} \hat{e}_l + v_l \cdot \nabla \hat{e}_l \right) &= \nabla \cdot (\alpha_l \kappa_l \nabla \cdot T_l) - p \left(\frac{\partial \alpha_l}{\partial t} + \nabla \cdot \alpha_l v_l \right) \\ &\quad + \Sigma_{rad}(T_g - T_l) + \Sigma_{vap_l}(T_s - T_l) \\ &\quad + \Gamma_{lv} h_l^s - \Gamma_l(\hat{e}_l - L_{e0}) + \Omega_{wl} + S_l, \end{aligned} \quad (20)$$

$$\begin{aligned} \alpha_g \rho_g \left(\frac{\partial}{\partial t} \hat{e}_g + v_g \cdot \nabla \hat{e}_g \right) &= \nabla \cdot (\alpha_g \kappa_g \nabla \cdot T_g) - p \left(\frac{\partial \alpha_g}{\partial t} + \nabla \cdot \alpha_g v_g \right) \\ &\quad + \Sigma_{rad}(T_l - T_g) + \Sigma_{vap_g}(T_s - T_g) \\ &\quad - \sum_{c=1}^3 \Gamma_{lc} h_{gc}^s - \Gamma_g \hat{e}_g + \Omega_{wg} + S_g, \end{aligned} \quad (21)$$

where Σ_{rad} and Ω_{wk} are the interphase and the volumetric wall-phase- k heat transfer coefficient, respectively.

2.3.1 Equations for implicit treatment of temperature

FETCH-MIPS solves directly for temperature, which is convenient, as it enables heat exchanges between the phases and diffusion terms, that depend explicitly on temperature, to be treated implicitly. To do this we use:

$$\hat{e}_l = C_{pl} T_l + \tilde{\hat{e}}_l - C_{pl} \tilde{T}_l, \quad \hat{e}_g = C_{pg} T_g + \tilde{\hat{e}}_g - C_{pg} \tilde{T}_g, \quad (22)$$

in which the tilde represents the explicit treat of the associated variables. A simple approximation to \hat{e}_l , \hat{e}_g is:

$$\hat{e}_l = C_{p_l} T_l, \quad \hat{e}_g = C_{p_g} T_g. \quad (23)$$

Equations 23 is often a reasonable approximation and the reason why solving for temperature in FETCH-MIPS is so effective. In addition, for each gas component h a similar approximation to 23 can be used, that is:

$$e_{gc} = \hat{e}_{gc} = C_{p_{gc}} T_g, \quad (24)$$

and thus:

$$\hat{e}_g = C_{p_g} T_g = \frac{1}{\sum_c \alpha_{gc} \rho_{gc}} \sum_c \alpha_{gc} \rho_{gc} \hat{e}_{gc} = \frac{1}{\sum_c \alpha_{gc} \rho_{gc}} \sum_c \alpha_{gc} \rho_{gc} C_{p_{gc}} T_g, \quad (25)$$

and thus:

$$C_{p_g} = \frac{1}{\sum_c \alpha_{gc} \rho_{gc}} \sum_c \alpha_{gc} \rho_{gc} C_{p_{gc}}, \quad (26)$$

in which $\alpha_{gc}, \rho_{gc}, e_{gc}$ are the gas volume fraction, density and internal energy of component h respectively, $C_{p_{gc}}$ is the heat capacity of component c of the gas phase, C_{p_l} is the heat capacity of component c of the liquid phase, and C_{p_l}, C_{p_g} are the heat capacities of the liquid and gas phases at constant pressure. From equation 11 and measuring T in Deg. C. then $\bar{e}_l = -L_e = -L_{e0}$ in which L_e is determined at $T_s = 0$ Deg. C.

The energy equations take a form in which the gas phase energy equation is made from the summation of the conservation equations for each of the gas components (air, hydrogen, steam):

$$\begin{aligned} C_{p_l} \rho_l \alpha_l \frac{D_{u_l} T_l}{Dt} &= -p \left(\frac{\partial \alpha_l}{\partial t} + \nabla \cdot \alpha_l v_l \right) - \rho_l \alpha_l \left(\frac{D_{u_l} \tilde{e}_l}{Dt} - C_{p_l} \frac{D_{u_l} \tilde{T}_l}{Dt} \right) \\ &\quad + \nabla \cdot (\alpha_l \kappa_l \nabla T_l) + \Sigma_{rad} (T_g - T_l) + \Sigma_{vap_l} (T_s - T_l) \\ &\quad + \Gamma_{lv} h_l^s + L_{e0} \Gamma_l - C_l T_l \Gamma_l + \Omega_{wl} + S_l, \end{aligned} \quad (27)$$

$$\begin{aligned} \sum_{c=1}^3 C_{p_{gc}} \rho_{gc} \alpha_{gc} \frac{D_{u_g} T_g}{Dt} &= -p \left(\frac{\partial \alpha_g}{\partial t} + \nabla \cdot \alpha_g v_g \right) - \sum_{c=1}^3 \rho_{gc} \alpha_{gc} \left(\frac{D_{u_g} \tilde{e}_{gc}}{Dt} - C_{p_{gc}} \frac{D_{u_g} \tilde{T}_g}{Dt} \right) \\ &\quad + \sum_{c=1}^3 \nabla \cdot (\alpha_{gc} \kappa_{gc} \nabla T_g) + \Sigma_{rad} (T_l - T_g) + \Sigma_{vap_g} (T_s - T_g) \\ &\quad + \sum_{c=1}^3 \Gamma_{gc} h_{gc}^s - \sum_{c=1}^3 C_{gc} T_g \Gamma_{cg} + \Omega_{wg} + S_g \end{aligned} \quad (28)$$

where c represents the gas phase (=1 (air), =2 (hydrogen), and =3 (steam)). The tilde indicates that the associated terms are treated explicitly but using their latest values during an iteration cycle. All the heat

capacities in the above equations will be assumed to be constant and spatially invariant in the below. Using

$$\frac{D_{u_l}\rho_l\alpha_l(\tilde{e}_l - C_{p_l}\tilde{T}_l)}{Dt} = 0, \quad (29)$$

$$\sum_{c=1}^3 \rho_{gc}\alpha_{gc} \frac{D_{u_g}(\tilde{e}_{gc} - C_{p_{gc}}\tilde{T}_g)}{Dt} = 0, \quad (30)$$

the energy equations 27, 28 become:

$$\begin{aligned} C_{p_l}\rho_l\alpha_l \frac{D_{u_l}T_l}{Dt} &= -p \left(\frac{\partial\alpha_l}{\partial t} + \nabla \cdot \alpha_l v_l \right) \\ &+ \nabla \cdot (\alpha_l \kappa_l \nabla T_l) + \Sigma_{rad}(T_g - T_l) + \Sigma_{vap_l}(T_s - T_l) \\ &+ \Gamma_{lv}h_l^s + L_{e0}\Gamma_l - C_l T_l \Gamma_l + \Omega_{wl} + S_l, \end{aligned} \quad (31)$$

$$\begin{aligned} C_{p_g}\rho_g\alpha_g \frac{D_{u_g}T_g}{Dt} &= -p \left(\frac{\partial\alpha_g}{\partial t} + \nabla \cdot \alpha_g v_g \right) \\ &+ \nabla \cdot (\alpha_g \kappa_g \nabla T_g) + \Sigma_{rad}(T_l - T_g) + \Sigma_{vap_g}(T_s - T_g) \\ &+ \sum_{c=1}^3 \Gamma_{gc}h_{gc}^s - C_{p_g}T_g\Gamma_g + \Omega_{wg} + S_g. \end{aligned} \quad (32)$$

It is now easy to see the effect of latent heat. On summing these two equations the interface heat exchange terms disappear, due to the interface Stefan condition (see section 3.2.2), leaving the term $L_{e0}\Gamma_l$ acting as a sink when boiling ($\Gamma_g = -\Gamma_l > 0$) and relaxing the liquid temperature towards T_s .

2.3.2 Calculating both temperature and internal energy in general

If one has access to more complex T, ρ, h, e relationships, for example, from tabulated data, e.g. steam tables, then both temperature and internal energy are needed with the above approach. Temperature is also needed for determining the nuclear cross section sets which depend on temperature.

Using the chain rule the enthalpy change for phase j :

$$dh_j = \left(\frac{\partial h_j}{\partial T_j} \right)_p dT_j + \left(\frac{\partial h_j}{\partial p} \right)_T dp \quad (33)$$

and thus

$$dh_j = C_{p_j}(T_j, p) dT_j + \left(\nu_j(T_j, p) - T_j \left(\frac{\partial \nu_j}{\partial T_j} \right)_p (T_j, p) \right) dp \quad (34)$$

and thus integrating between a reference state T_{jR}, p_R and some state T_j, p gives

$$h_j(T_j, p) - h_j(T_{jR}, p_R) = \int_{T_R}^T C_{p_j}(z, p) dz + \int_{p_R}^p \left(\nu_j(T_j, z) - T_j \left(\frac{\partial \nu_j}{\partial T_j} \right)_p (T_j, z) \right) dz. \quad (35)$$

These equations can then be inverted for temperature T_j or used to obtain either e_j, h_j in the implicit treatment of temperature in the previous section. The FETCH-MIPS approach solves for temperature directly using equations 27, 28 and equation 34 or 35 can then be applied to determine $e_j = h_j - \frac{p}{\rho_j}$. The approach taken by RELAP, see [7], uses a direct approach for determining temperature and involves an extrapolation process:

$$\tilde{T}_l^{n+1} = \tilde{T}_l^n + \left(\frac{\partial T_l}{\partial p} \right)_{e_l}^n (p^{n+1} - p^n) + \left(\frac{\partial T_l}{\partial e_l} \right)_p^n (e_l^{n+1} - e_l^n), \quad (36)$$

$$\tilde{T}_l^{n+1} = \tilde{T}_l^n + \left(\frac{\partial T_g}{\partial p} \right)_{e_g}^n (p^{n+1} - p^n) + \left(\frac{\partial T_g}{\partial e_g} \right)_p^n (e_g^{n+1} - e_g^n), \quad (37)$$

in which

$$\left(\frac{\partial T_l}{\partial e_l} \right)_p = \frac{1}{C_{p_l} - \nu_l \beta_l p}, \quad \left(\frac{\partial T_g}{\partial e_g} \right)_p = \frac{1}{C_{p_g} - \nu_g \beta_g p}, \quad (38)$$

and

$$\left(\frac{\partial T_l}{\partial p} \right)_{e_l} = \frac{p \nu_l k_l - T_l \nu_l \beta_l}{(C_{p_l} - \nu_l \beta_l p) \nu_l^2}, \quad \left(\frac{\partial T_g}{\partial p} \right)_{e_g} = \frac{p \nu_g k_g - T_g \nu_g \beta_g}{(C_{p_g} - \nu_g \beta_g p) \nu_g^2}, \quad (39)$$

in which the n indicates the time level, and for phase j : ν_j is the specific volume; β_j is the isobaric thermal expansion coefficient K^{-1} ; k_j is the thermal conductivity.

2.4 The Multi-component Flow Submodel

Multi-phase multi-component models for the simulation of flow and transport processes in multi-component gas flows are used widely in various technical application fields. It is characterized by the flow of more than one fluid phase (e.g., air, hydrogen, steam) and the transport of components in the fluid phases. Many multi-phase multi-component processes are strongly affected by non-isothermal effects, in particular when processes such as evaporation/condensation play a dominant role. For the description of temperature-dependent processes, transitions of components between the phases, coupled with an exchange of thermal energy, have to be taken into account in addition to the flow of the individual phases. Therefore, the formulation of a mathematical/numerical model requires an idealization of the physical processes in such a way that the natural systems are simplified but, at the same time, the characteristic properties of the processes in a system are maintained. In this work, air, hydrogen and steam are mixed in thermodynamical equilibrium. In the following sections the multi-component balance in the gas phase is introduced and its relationship with the equations of state and thermal properties used for each of the particles are presented.

2.4.1 The Gas Phase Multi-Components

Consider a closed system with C components (different gases) in the gas phase (their masses are known and can be represented as $m_1, m_2, \dots, m_{C-1}, m_C$) where there is no mass and energy transferred

to the neighborhood. The volume fraction of the gas phase is represented by

$$\alpha_g = \sum_{c=1}^C \alpha_{gc} \quad (40)$$

although α_g is calculated by solving the continuity equation for the gas and where c is the component of the gas phase, i.e., in this work, air, hydrogen, steam. Thus, the mass balance of each component of the gas phase is:

$$\rho_g = \frac{\sum_{c=1}^C \rho_{gc} \alpha_{gc}}{\alpha_g}. \quad (41)$$

The continuity equation may be rewritten for each component of the gas phase as

$$\frac{\partial}{\partial t} (\rho_{gc} \alpha_{gc}) + \nabla \cdot (\alpha_{gc} \rho_{gc} v_g) = G_{lc} - G_{cl}, \quad \forall c \in \{1, 2, 3\}. \quad (42)$$

Therefore, the multi-component mass balance for each gas may be represented by

$$\frac{\partial \hat{\alpha}_{gc}}{\partial t} + \nabla \cdot v_g \hat{\alpha}_{gc} = \frac{G_{lc} - G_{cl}}{\rho_{gc_0}}, \quad \forall c \in \{1, 2, 3\} \quad (43)$$

where $\hat{\alpha}_{gc}$ is the normalized concentration of gas h and

$$\hat{\alpha}_{gc} = \frac{\rho_{gc} \alpha_{gc}}{\rho_{gc_0}}, \quad (44)$$

in which ρ_{gc_0} is a typical value of ρ_{gc} . The summation of equation 52 gives (using equations 40 and 41) the continuity equation for the gas phase, equation 1 or:

$$\frac{\partial}{\partial t} (\rho_g \alpha_g) + \nabla \cdot (\alpha_g \rho_g v_g) = \sum_c (G_{lc} - G_{cl}) = G_{lg} - G_{gl}. \quad (45)$$

In the following C_{pgc} and κ_{gc} are the heat capacity and thermal conductivity of each gas component c ($=1, 2, 3$, for air, hydrogen, steam). C_{pg} is the bulk heat capacity of the solid phase

$$C_{pg} \rho_g \alpha_g = \sum_{c=1}^3 C_{gc} \rho_{gc} \alpha_{gc}. \quad (46)$$

Thus

$$C_{pg} = \frac{\sum_{c=1}^3 C_{pgc} \rho_{gc} \alpha_{gc}}{\rho_g \alpha_g}. \quad (47)$$

The thermal diffusion of the gas phase is expressed as

$$\nabla \cdot (\alpha_g \kappa_g \nabla T_g) = \sum_{c=1}^3 \nabla \cdot (\alpha_{gc} \kappa_{gc} \nabla T_g) \quad (48)$$

where $\alpha_g \kappa_g$ is the effective thermal conductivity of the gas phase. Thus:

$$\kappa_g = \frac{\sum_{c=1}^3 \alpha_{gc} \kappa_{gc}}{\alpha_g}. \quad (49)$$

2.4.2 Radiolytic gas modelling

The concentration of radiolytic gas is given by:

$$\frac{\partial C_{lr}}{\partial t} + \nabla \cdot v_l C_{lr} = S_{rad} - (G_{lr} - G_{rl}) - \Gamma_{rad} \quad (50)$$

in which r indicates the radiolytic gas field (mostly hydrogen), C_{lr} is the dissolved radiolytic gas concentration in solution, S_{rad} is the source of dissolved radiolytic gas from fission which it is proportional to the fission rate here. In addition, the mass transfer rate of radiolytic gas from the solution to the gas phase and visa versa is:

$$G_{lr} = \max\{0, \mathcal{X}(C_{lr} - \alpha_l C_0)\}, \quad G_{rl} = -\min\{0, \mathcal{X}(C_{lr} - \alpha_l C_0)\}. \quad (51)$$

in which C_0 is the concentration of radiolytic gases dissolved in the liquid solution at which radiolytic gases start to diffusion into radiolytic gas bubbles which is determined from Henrey's law, see next subsection and the FETCH-MIPS manual [8]. Thus from equation 52 the equation for the advection of radiolytic gas in the gas phase is:

$$\frac{\partial \hat{\alpha}_{gr}}{\partial t} + \nabla \cdot v_g \hat{\alpha}_{gr} = \frac{G_{lr} - G_{rl} + \Gamma_{rad}}{\rho_{gr0}}. \quad (52)$$

When the fissile liquid turns to vapour the radiolytic gases dissolved in the liquid turn are released. Suppose the vapour production rate is Γ_{gv} then the corresponding radiolytic gas in the gas phase production rate is:

$$\Gamma_{rad} = \frac{C_{lr}}{\alpha_l \rho_l} \Gamma_{gv} \quad (53)$$

and thus the steam content in the production rate is $\Gamma_{steam} = \Gamma_{gv} + \Gamma_{rad}$.

2.4.3 Radiolytic gas bubble modelling and parameterizations of rate of radiolytic gas production

The pressure in the solution p_∞ is related to the concentration C_0 at the bubble surface via Henry's law:

$$p_{rad} \approx p_\infty + \frac{2\gamma}{R} = H(T_g)C_0 \quad (54)$$

in which γ is the surface tension coefficient, p_∞ is the pressure of the solution in the vicinity of the bubble, p_{rad} is the partial pressure of the gas inside the bubble for the gas under consideration e.g. hydrogen, R is the bubble radius and H Henry's constant. The ideal gas equation relating temperature pressure and density of the gas is

$$p_{rad} = K_{rad}\rho_{rad}T_g, \quad (55)$$

where ρ_{rad} is the radiolytic gas density.

The spherically symmetric momentum equation for an incompressible inviscid liquid is

$$\rho \left(\frac{\partial q}{\partial t} + q \frac{\partial q}{\partial x} \right) = - \frac{\partial p}{\partial x}$$

in which p, ρ, q, t, x are the pressure, density, radial velocity, time and spherical radius respectively. Integrating the associated incompressible continuity equation $\frac{\partial x^2 q}{\partial x} = 0$ between the $x = 0$ and a bubble radius R gives the velocity $q = \frac{R^2 \dot{R}}{x^2}$. Placing this expression into the momentum equation above and integrating again one obtains the Rayleigh-Plesset equation for a bubble:

$$(p_{rad} - \frac{2\gamma}{R} - p_\infty)/\rho = R \ddot{R} + \frac{3}{2} \dot{R}^2 \quad (56)$$

This equation governs the dynamics of a radiolytic gas bubble in an incompressible liquid.

In addition the concentration C of dissolved gas in the incompressible liquid is given by

$$\frac{\partial C}{\partial t} + q \frac{\partial C}{\partial x} = \frac{1}{x^2} \frac{\partial}{\partial x} \left(D_{rad} x^2 \frac{\partial C}{\partial x} \right) + S \quad (57)$$

where the source S is from the deposition of radiolytic gases due to fission processes and D_{rad} is the binary diffusion coefficient of radiolytic gases taken as hydrogen, typically given by $D_{rad} = 6.3 \times 10^{-4} \text{ cm}^2 \text{s}^{-1}$ at room temperature and pressure is approximately proportional to $\frac{T_g^{3/2}}{p_{rad}}$ otherwise. Generalisation of this equation for compressible liquids can be found in [9].

One can calculate the concentration C_{in} of gas inside the bubble from

$$\int_{\Gamma} D_{rad} \frac{\partial C}{\partial n} d\Gamma = \int_V \rho_{rad} \frac{\partial C_{in}}{\partial t} d\Omega \quad (58)$$

in which Γ and V are the bubble surface and volume respectively. The derivative on the liquid side of the bubble $\frac{\partial C}{\partial n}$ is calculated from C obtained from equation 57 above. Alternatively, one could use approximate correlations of the form $D_{rad} \frac{\partial C}{\partial n} = h(C - C_0)$ in which h is the concentration transfer coefficient, see [10].

In summary, to calculate the bubble radius with time the following operations are required: 1) Calculate C_{in} from equation 58; 2) Calculate p_{rad} from C_{in} and R using equations 55 and 58 ; 3) Calculate C from equations 57 using C_0 from equation 54 as a boundary condition; Note that eventually $\frac{\partial C}{\partial n} = 0$ with $C_{in} \neq C_0$.

Suppose C_∞ is the concentration far from the bubble (taken from the FETCH-MIPS numerical model for example). Then the above bubble model can be initialised with the following equilibrium conditions: $C = C_\infty, p_{rad} = H(T_g)C_0, C_{in} = \frac{p_{rad}}{K_{rad}T}, \dot{R} = \ddot{R} = 0, R = 2 \times 10^{-5} \text{ cm}$ - the size of a typical micro-bubble.

To calculate the bubble radius R after a pressure change the above model can be highly simplified by assuming equilibrium conditions, that is: $C_0 = C_\infty, p_{rad} = H(T_g)C_0$. The bubble radius can then

be computed from $R = \frac{2\gamma}{p_{rad} - p_\infty}$. There will be a need to diffuse gas to or from the bubble so that $C_{in} = \frac{p_{rad}}{K_{rad}T}$.

Various authors [11, 12, 13, 14, 15] have suggested that bubbles are nucleated along fission tracks. These bubbles have a radius less than $r_0 = 2 \times 10^{-5}\text{cm}$ and many bubbles are nucleated close to this size. The smaller bubbles collapse very quickly due to surface tension forces, say on a time scale of 10^{-9} seconds depending on how close they are to the value of the critical concentration of radiolytic gas C_0 at which gases start to diffuse into bubbles. This saturation is given by Henry's law $p_{rad} \approx p_\infty + \frac{2\gamma}{r_0} = H(T_g)C_0$ which relates the partial pressure p_{rad} of radiolytic gas (hydrogen) in a bubble of radius r_0 to the concentration of radiolytic gas at the bubble surface. However, bubbles of radius r smaller than r_0 can be nucleated for concentrations C (greater than C_0) given by $p_{rad} \approx p_\infty + \frac{2\gamma}{r} = H(T_g)C$. Thus any excess concentration C of dissolved gas above C_0 will result in the growth of nucleated bubbles of radius greater than r . The pressure p_{rad} in the bubble, assuming equilibrium conditions, is given by, $p_{rad} - \frac{2\gamma}{r} = p_\infty$. Thus the initial sizes of the nucleated bubbles is of crucial importance in determining the volume of gas in bubbles. The distribution of nucleated bubble sizes is often assumed to vary as $\frac{1}{r^2}$ below an initiated bubble size r_0 . On integrating the bubbles produced by an excess concentration C above C_0 , the result is that the number of bubbles that, once nucleated, will grow is proportional to

$$H(T_g)(C - C_0).$$

In fact often $H(T_g)$ is left out of this expression (assumed constant), see Hetrick [11], Mather [13, 14]. Clearly distributions other than $\frac{1}{r^2}$ may offer a more accurate representation of nucleated bubble sizes. However, the $\frac{1}{r^2}$ correlation appropriately makes the number of smaller bubbles larger than the number of larger bubbles. Another natural distribution is to make the volume occupied by the smaller bubbles the same as that of the larger bubbles.

Using the assumption that nucleation of bubbles occurs along fission tracks, it is not unreasonable to presume that the number of nucleated bubbles per unit volume is equal to $\nu H(T_g)(C - C_0)$, where ν is the number of fissions per unit volume. It is usually a good assumption that the nucleated bubbles expand, instantaneously, to their final bubble radius r again given by Henry's law since they reach their final volume on time scales of 10^{-8} seconds. These bubbles occupy a volume given by the ideal gas equation, say. The equation for concentration of dissolved radiolytic gases take the form

$$\frac{\partial \alpha_l C}{\partial t} + \nabla \cdot u_l \alpha_l C = S_l^c + F_l^c$$

in which u_l is the liquid phase velocity, α_l is the liquid volume fraction, $\alpha_l C$ is the dissolved radiolytic gas concentration, S_l^c is the source of dissolved radiolytic gas due to deposition of radiolytic gas from fission processes and F_l^c is the sink of dissolved radiolytic gas as the gas appears in bubble form.

In this work we use the following expression for the exchange of radiolytic gas between the phases

$$F_l^c = \mathcal{X}(C_l - C_0). \quad (59)$$

A suitable function for \mathcal{X} has been obtained by correlating pressures with experiments, see [3] and also with the guidance of Mather [12, 13, 14]. The following \mathcal{X} is used here

$$\mathcal{X} = \mathcal{H}(C_l - C_0)\alpha_l \hat{\mathcal{X}}(C_l) \quad (60)$$

in which we have correlated $\hat{\mathcal{X}}$ to match the pressure traces of experimental results using

$$\hat{\mathcal{X}}(C_l) = N(C_l - \hat{C}_0)^n \quad (61)$$

in which \hat{C}_0 is the gas diffusion threshold at ambient temperature and zero solution pressure, so the pressure in the micro-bubbles of radius $r_0 = 2 \times 10^{-2}$ cm, is from surface tension only (assumed to be 7 bars). \mathcal{H} is the Heavyside function in the above equation, its use prevents modeled radiolytic gas in the form of bubbles from dissolving back into the liquid. The scalars N and n in equation 61 are correlated to match the shape and magnitude of the pressures (using a least squares procedure) generated in SILENE experiments (see [3]), with the result that $N = 4.71 \times 10^{16}$ and $n = 3$. As the fission rate increases therefore, the quantity of gas in bubbles sharply increases, and results in a sharp increase in the pressure with all delayed and prompt supercritical step reactivities - in the case of dilute Pu transients then prompt criticality may be reached although the transient may have begun as delayed critical. This gas expands the liquid increasing the neutron leakage and resulting in a negative neutron feedback effect, which in turn reduces the fission rate and therefore the pressure of the system due to expansion of nucleated bubbles. The result is a sharp pressure peak.

Bubble sizes will then vary due to the changing pressure and concentration of dissolved gas in solution. This occurs by both changes in volume due to pressure and changes in the concentration of radiolytic gas at the bubble surface. These changes in bubble sizes can again be assumed to occur instantaneously as they occur on a short time scale compared to the time scales on which significant changes in fission rate occur. However, there are other bubble mechanisms, such as the destruction of micro-bubbles by fission fragments and bubble coalescence, both of which can reduce the net quantity of radiolytic gas in bubbles. In addition, as boiling is approached, the quantity of water vapor in bubbles sharply increases and eventually water vapor partial pressure swamps that of radiolytic gas in bubbles. This results in an increase of diffusion of hydrogen via Henry's law, into bubbles. Mather [12] assumed that this water vapor is at the saturated vapor pressure at the given temperature and pressure in the bubbles.

3 Parameterizations for Multi-Phase Fluid Exchanges with Boiling

The exchanges that occur at the interface between the fluids are discussed in this section. This is linked intimately with the averaging process, which injects uncertainties; thus, closure relations are sought based on empirical correlations.

3.1 Multi-phase energy exchange

Temperature exchange occurring at the interface between phases is modelled with the term $\gamma = \hat{a}_{lg}\hat{k}_{lg}$, i.e., the volumetric interphase heat transfer, where \hat{a}_{lg} is the volumetric surface at which energy (or mass) transfer occurs. The heat transfer coefficient is calculated by the Ranz-Marshall correlation valid for spherical bubbles or particles,

$$Nu = \frac{\hat{k}_{lg}d_b}{D} = 2 + 0.6Re^{\frac{1}{2}}Pr^{\frac{1}{3}}. \quad (62)$$

where $Nu, Re \in [0, 200]$ and $Pr \in [0, 250]$ are the dimensionless Nusselt, Reynolds and Prandtl numbers, respectively. d_b is the bubble diameter and D the thermal diffusivity. There is a strong analogy between heat and mass transfer (due to the similarity of the boundary layer scale equations) and thus the Nu number has similar correlations to the Sherward number.

3.2 Interface mass and heat transfer

3.2.1 Simple expression for vapour production/condensation

For simplicity, the model was initially tested with very simple expressions for the mass transfer before proceeding to physically based parameterizations. The simple expression for the interphase mass exchange, that was used for the vapour production is: $G_{l3} = W \mathcal{H}(T_l - T_{l,sat}) \alpha_l \rho_{g30}$, where W is the inverse time constant for bubble production. In this work, $W=1\times 10^{-2}s^{-1}$. This time scale is the smallest that can be resolved by FETCH-MIPS in a typical FETCH-MIPS transient and does not necessarily accurately represent reality. \mathcal{H} is the Heaviside function. For condensation: $G_{3l} = W \mathcal{H}(T_{g,sat} - T_g) \hat{\alpha}_g \rho_{g30}$. \mathcal{H} is replaced by a sigmoid function here of a particular width h_{wid} (e.g. 2 Deg. C.) so that the boiling correlation acts more smoothly which helps the iterative solvers to converge. ρ_{g30} is a representative water vapour density at boiling and similarly ρ_{l0} is a representative liquid density at boiling.

Once the basic structure of FETCH-MIPS was developed using this simplest possible parameterization more rigorous correlations were introduced for heat transfer based on RELAP bubbly solutions models, see [7]. The mass exchange terms between the phases were then determined from the heat transfer based on the interface Stefan condition.

3.2.2 Interface Stefan condition for mass transfer from heat transfer

The interface Stefan condition for mass transfer from heat transfer is determined by considering the thermal energy equation over the interface between the liquid and vapour/gas and ignoring storage terms in the equations. See reviews of interfacial mass exchange rate modelling, [16], [17]. The Stefan condition is parameterized here by summing the heat transfer and mass transfer terms for vapour in the energy equations and setting this balance to zero:

$$\Sigma_{vap_l}(T_s - T_l) + \Sigma_{vap_g}(T_s - T_g) + \Gamma_{gv}L_h = 0 \quad (63)$$

in which we have used the latent heat

$$\Gamma_{gv} h_{gv}^s + \Gamma_{lv} h_l^s = \Gamma_{gv} (h_{gv}^s - h_l^s) = \Gamma_{gv} L_h \quad (64)$$

also $\Gamma_{gv} = -\Gamma_{lv}$ and thus the mass transfer rate Γ_{gv} is determined from:

$$\Gamma_{gv} = -\frac{\Sigma_{vap_l}(T_s - T_l) + \Sigma_{vap_g}(T_s - T_g)}{L_h}. \quad (65)$$

It now only remains to determine the heat transfer coefficients $\Sigma_{vap_l}, \Sigma_{vap_g}$.

3.2.3 Implementation of heat exchange due to vapourization/condensation

Limiting the magnitude of the heat transfer based on time scales that can be resolved

When producing vapour we want to avoid producing more vapour than there is available which has an upperbound on Γ_{gv} of $\frac{\alpha_l \rho_l}{\Delta t}$. This is also used as a basis to limit the value of Γ_{gv} . Similarly, when condensing then a further constraint is added to ensure we don't remove more vapour than is available which has an upper bound of $\frac{\alpha_g \rho_{gv}}{\Delta t_{ref}}$. Similarly, the maximum value of the mass transfer that can be resolved within a time interval Δt_{ref} is $\frac{\rho_{gv}}{\Delta t_{ref}}$. Combining these constraints and when $T_l > T_s$ (vapourizing contribution - see equation 65) the maximum mass transfer rate for the liquid phase contribution is:

$$\Gamma_{gv_{max}}^l = \min\left\{\frac{\rho_{gv}}{\Delta t_{ref}}, \frac{\alpha_l \rho_l}{\Delta t}\right\}, \quad (66)$$

else (condensing contribution - see equation 65):

$$\Gamma_{gv_{max}}^l = \frac{\rho_{gv}}{\Delta t_{ref}}, \quad (67)$$

When $T_g > T_s$ (vapourizing contribution - see equation 65):

$$\Gamma_{gv_{max}}^g = \min\left\{\frac{\rho_{gv}}{\Delta t_{ref}}, \frac{\alpha_l \rho_l}{\Delta t}\right\}, \quad (68)$$

else (condensing contribution - see equation 65):

$$\Gamma_{gv_{max}}^g = \frac{\rho_{gv}}{\Delta t_{ref}}. \quad (69)$$

The value of Δt_{ref} can be chosen based on a multiple of the time step size. Here $\Delta t_{ref} = 0.01$ seconds is used.

Thus the maximum value of the heat transfer for the liquid and gas are:

$$\Sigma_{vap_l_{max}} = \frac{\Gamma_{gv_{max}}^l L_h}{\max\{\varepsilon, |T_s - T_l|\}}, \quad (70)$$

$$\Sigma_{vap_g_{max}} = \frac{\Gamma_{gv_{max}}^g L_h}{\max\{\varepsilon, |T_s - T_g|\}}, \quad (71)$$

for a small ε e.g. $\varepsilon = 10^{-5}$.

Implicitness when solving for temperature of each phase separately

The liquid and gas phase exchange terms due to vapourization/condensation are for the liquid:

$$\Sigma_{vap_l}(T_s - T_l) + \Gamma_{lv}h_l^s + L_{e0}\Gamma_l, \quad (72)$$

and the gas:

$$\Sigma_{vap_g}(T_s - T_g) + \Gamma_{gv}h_g^s. \quad (73)$$

Inserting the expression for $\Gamma_{gv} = -\Gamma_{gv}$:

$$\Sigma_{vap_l}(T_s - T_l) + \frac{\Sigma_{vap_l}(T_s - T_l) + \Sigma_{vap_l}(T_s - T_g)}{L_h}(h_l^s + L_{e0}), \quad (74)$$

$$\Sigma_{vap_g}(T_s - T_g) + \frac{\Sigma_{vap_l}(T_s - T_l) + \Sigma_{vap_l}(T_s - T_g)}{L_h}h_g^s. \quad (75)$$

To help increase the implicitness of the method we collect the terms from these expressions that operate on T_l and T_g respectively to yield:

$$\sigma_l = \Sigma_{vap_l} + \Sigma_{vap_l} \frac{(h_l^s + L_{e0})}{L_h}, \quad (76)$$

$$\sigma_g = \Sigma_{vap_g} - \Sigma_{vap_g} \frac{h_g^s}{L_h}, \quad (77)$$

and a good approximation to this is:

$$\sigma_l = \Sigma_{vap_l}, \quad \sigma_g = \Sigma_{vap_g}. \quad (78)$$

The final internal energy equations solved with FETCH-MIPS are then:

$$\begin{aligned} C_{pl}\rho_l\alpha_l \frac{D_{u_l}T_l}{Dt} &= -p \left(\frac{\partial\alpha_l}{\partial t} + \nabla \cdot \alpha_l v_l \right) \\ &+ \nabla \cdot (\alpha_l \kappa_l \nabla T_l) + \Sigma_{rad}(T_g - T_l) + \sigma_l(\tilde{T}_l - T_l) \\ &+ \Sigma_{vap_l}(T_s - T_l) + \Gamma_{lv}h_l^s + L_{e0}\Gamma_l - C_l T_l \Gamma_l + \Omega_{wl} + S_l, \end{aligned} \quad (79)$$

$$\begin{aligned} C_{pg}\rho_g\alpha_g \frac{D_{u_g}T_g}{Dt} &= -p \left(\frac{\partial\alpha_g}{\partial t} + \nabla \cdot \alpha_g v_g \right) \\ &+ \nabla \cdot (\alpha_g \kappa_g \nabla T_g) + \Sigma_{rad}(T_l - T_g) + \sigma_g(\tilde{T}_g - T_g) \\ &+ \Sigma_{vap_g}(T_s - T_g) + \Gamma_{gv}h_g^s - C_{pg}T_g\Gamma_g + \Omega_{wg} + S_g. \end{aligned} \quad (80)$$

3.2.4 Heat transfer for liquid-vapour in bubbly flows

The inter-facial heat transfer in bulk fluid is determined from Σ_{vap_l} , Σ_{vap_g} which are parameterized for bubbly solutions as below as used by RELAP, see [7]. For now we assume all gas is vapour.

Super-heated liquid ($\Delta T_{sl} = T_s - T_l < 0$)

$$\Sigma_{vap_l} = \max\left\{\frac{k_f}{d_b} \frac{12}{\pi} \Delta T_{sl} \frac{\rho_l C_{pl}}{\rho_g L_h} \beta, \frac{k_l}{d_b} (2 + 0.74 Re_b^{0.5})\right\} a_{gl}, \quad (81)$$

in which the first part of the expression is from the Plessent-Zwick correlation and the second from a modified Lee-Ryley correlation and where the bubble Reynolds number is:

$$Re_b = \frac{(1 - \alpha_{bub}) \rho_l v_{slip} d_b}{\mu_l} = \frac{We \sigma (1 - \alpha_{bub})}{\mu_l (v_{slip}^2)^{0.5}}, \quad (82)$$

in which σ is the surface tension coefficient and the average bubble diameter is ($=0.5d_{max}$):

$$d_b = \frac{We \sigma}{\rho_l v_{slip}^2}, \quad (83)$$

with $We = 5$, $We \sigma = \max\{We \sigma, 10^{-10}\}$ N/m. $\beta = 1$ and the inter-facial area per unit volume is:

$$a_{gl} = \frac{3.6 \alpha_{bub}}{d_b}, \quad (84)$$

and $\alpha_{bub} = \max\{\alpha_g, 10^{-5}\}$ and the slip velocity is $v_{slip} = v_g - v_l$.

Sub-cooled liquid ($\Delta T_{sl} = T_s - T_l > 0$)

The modified Unal and Lahey expression is used:

$$\Sigma_{vap_l} = \max\{\Sigma_{vap_{lmax}}, \frac{F_5 L_h \rho_g \rho_l \alpha_g}{\rho_l - \rho_g}\}, \quad (85)$$

where

$$F_5 = 0.075 \quad \text{for } \alpha_{bub} \geq 0.25, \quad (86)$$

$$F_5 = 1.8 \varphi C \exp\{-45 \alpha_{bub}\} + 0.075 \quad \text{for } \alpha_{bub} < 0.25, \quad (87)$$

$$C = 65 - 5.69 \times 10^{-5} (p - 1 \times 10^5) \quad \text{for } p \leq 1.1272 \times 10^6 \text{ Pa}, \quad (88)$$

$$C = \frac{2.5 \times 10^9}{p^{1.418}} \quad \text{for } p > 1.1272 \times 10^6 \text{ Pa}, \quad (89)$$

$$\varphi = 1 \quad \text{for} \quad |v_{slip}| \leq 0.61m/s, \quad (90)$$

$$\varphi = (1.639344|v_{slip}|)^{0.47} \quad \text{for} \quad |v_{slip}| > 0.61m/s. \quad (91)$$

A maximum is imposed on Σ_{vap_l} for stability reasons by a number of codes, e.g. RELAP and COBRA, and this maximum is of the form:

$$\Sigma_{vap_l max} = 17539 \max\{4.724, 472.4\alpha_g\alpha_l\} \max\{0, \min\{1, \frac{\alpha_g}{0.1}\}\}. \quad (92)$$

Super-heated and sub-cooled gas/vapour:

$$\Sigma_{vap_g} = 10^4 a_{gl}. \quad (93)$$

3.2.5 Vapour generation/condensation in the presence of non-condensable radiolytic gases

Vapour production is greatly delayed in the presence of non-condensable gases like hydrogen generated from radiolysis. The approach taken here is to use a standard correlation for water homogeneous vapour production/condensation and to scale this rate by an experimentally determined value in order to take into account the presence of radiolytic gases. In this case we will amend the values of Σ_{vap_l} , Σ_{vap_g} according to Dalton's law ($p = p_v + p_{rad}$) and the partial pressure of the vapour p_v and radiolytic gases p_{rad} so they become:

$$\Sigma_{vap_l}' = \Sigma_{vap_l}, \quad (94)$$

$$\Sigma_{vap_g}' = \frac{p_v}{p} \Sigma_{vap_g}, \quad (95)$$

and

$$\Sigma_{rad}' = \frac{p_{rad}}{p} \Sigma_{rad}, \quad (96)$$

in which the partial pressure of radiolytic gas p_{rad} and the vapour p_v make up the bulk pressure so $p_v = p - p_{rad}$ in which in our case p_{rad} is determined from the ideal gas equation for radiolytic gas assumed to be hydrogen.

Assuming ideal gas behaviour then the radiolytic and vapour pressures are:

$$p'_{rad} = \frac{K_{rad} \frac{\alpha_{rad}}{\alpha_g} \rho_{rad}}{T_{kel}}, \quad p'_v = \frac{K_v \frac{\alpha_v}{\alpha_g} \rho_v}{T_{kel}}, \quad (97)$$

in which the temperature T_{kel} is measured in Kelvin. Now the partial pressure summation is assumed to be:

$$p = p_{rad} + p_v = \frac{\alpha_{rad}}{\alpha_g} p + \frac{\alpha_v}{\alpha_g} p, \quad (98)$$

with

$$p_{rad} = \frac{\alpha_{rad}}{\alpha_g} p, \quad p_v = \frac{\alpha_v}{\alpha_g} p. \quad (99)$$

Thus

$$\frac{p_{rad}}{p} = \frac{\alpha_{rad}}{\alpha_g}, \quad \frac{p_v}{p} = \frac{\alpha_v}{\alpha_g}, \quad (100)$$

with $\alpha_g = \alpha_{rad} + \alpha_v$.

It may be worth pointing out that substantial reductions in reductions of heat transfer rates, see for example [18] (page 371) where some 30% say reduction of heat transfer rates are observed in forced convection (85% in stagnant conditions) with 10% mass fractions of non-consensible air with steam.

4 Comparison of FETCH-MIPS and RELAP equations and parameterizations

4.1 Motivation for use of RELAP models within FETCH

RELAP is held in high regard internationally and is effectively used within the boiling models of the level one analysis conducted by MMR Williams, see [1]. For these reasons we have based the parameterizations used for the boiling models in FETCH-MIPS on those used by RELAP. In addition, the equations that are solved are very similar but differ in their detail.

4.2 Internal energy equations

For example, although FETCH-MIPS and RELAP use internal energy equations which are of the same form, FETCH-MIPS solves directly for temperature rather than internal energy. It does this in order to treat the diffusion of temperature and the phase heat transfer of internal energy implicitly (to enhance time step stability) as these are both expressed in terms of temperature. RELAP solves for internal energy and treats these two terms explicitly. Once internal energy is obtained in RELAP then the chain rule is used to determine temperature using an extrapolation process, see equations 36 and 37.

FETCH-MIPS also solves the internal energy equation in non-conservative form rather than the conservative form used in RELAP, although FETCH-MIPS has options for conservative forms of all equation sets. FETCH-MIPS does this because it has been found that the use of conservative form, although in theory can be equivalent at both the continuum and discrete levels, in practice it can lead to numerical

instability due to the fact that the system of equations in conservative form can be ill posed without dissipation, see [19]. This instability has been observed, in FETCH, despite the fact that the discrete equations in both forms are equivalent, because a numerically consistent discretization is used in FETCH, that is the discrete continuity equation is imbedded in the internal energy equation.

4.3 Momentum equations

The momentum equations are also of the same form in FETCH-MIPS and RELAP although again FETCH-MIPS has used a non-conservative form. This however is not numerically consistent so does not conserve momentum but is more stable as it does not generate sources and sinks of momentum due to the continuity equations not being tested over the velocity basis functions. FETCH-MIPS and RELAP use the same velocity for the liquid-vapour interface, which is the velocity of the current phase. Again this choice results in non-conservation of momentum for both models although we have found that conservative choices result in very similar results. Conservation of momentum is given a smaller priority than conservation of internal energy which is exactly satisfied in both models.

4.4 Heat and mass transfer parameterizations

Both models form parameterizations for heat transfer between the vapour and liquid phases and FETCH-MIPS models are based on RELAP's. Using the Stefan condition (an expression of internal energy conservation over the liquid-vapour interface) the mass transfer rates between the phases are then determined in both models. Both models limit the heat transfer rates between the phases primarily to limit the mass transfer rates between the phases and achieve numerically stable solutions. However, the details of this limiting are different. The main difference is that RELAP (for reasons we do not understand) multiplies the limiting functions by the heat transfer correlations to form the heat transfer correlations used in the numerical simulations. However, these limiting functions are expressions of the maximum amount of mass transfer that the numerical schemes can tolerate within one time step and still be stable and thus in FETCH-MIPS we use these as a maximum heat transfer rate allowed and adjust the heat transfer rates to respect this upper bound.

The presence of radiolytic gases in the gas phase can act to substantially reduce the rate at which vapour can be produced. It does this by reducing the diffusion coefficient in the gas phase side of the vapour-liquid interface. RELAP and FETCH-MIPS both use Dalton's law to reduce this coefficient according to the ratio of the partial pressure of the vapour and the total gas pressure. RELAP does this explicitly in terms of these pressures and FETCH-MIPS converts this to a ratio of vapour to gas volume fractions.

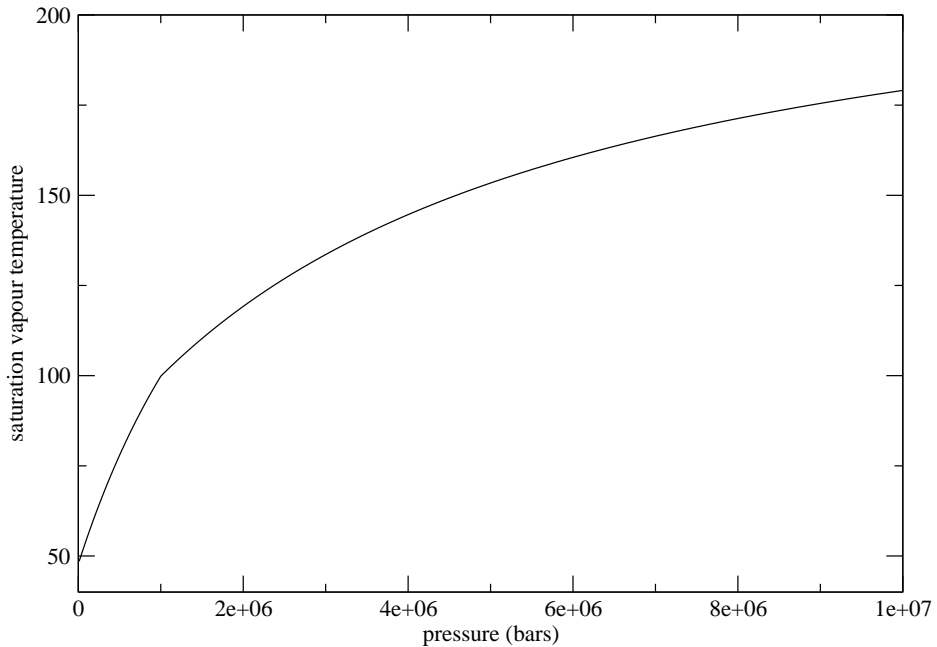


Figure 1: Parameterization of saturation vapour temperature against pressure.

5 Modelling Results with Boiling

This section presents five sets of FETCH-MIPS results: i) homogeneous boiling to help validate the boiling model; ii) homogeneous boiling with radiolytic gases applied using CRAC38 geometry and solution and varying step reactivity insertions; iii) a FETCH-MIPS's model of the CRAC43 transient with boiling; iv) application to MIPS with a 440KW power output. v) postulated accident within MIPS - step reactivity in 'steady state' conditions. Ideal gas behavior is used for all gas components here, air, vapour, radiolytic gas, along with constant heat capacities at constant pressures. A linear in temperature and pressure equation of state was used for the fissile solution density. The saturation temperature is parameterized with pressure as shown in figure 1, using two *tanh* functions meeting at 100 Deg. C.

5.1 Volumetric boiling experiments

Greenfield et al (1954) [20] conducted a detailed experimental and theoretical study of vapour production/boiling in a chamber due to volumetric heating. This is the only experiment, that we are aware of, that has been conducted involving homogenous superheating of liquids and thus it is natural for

us to use this to help validate FETCH boiling without the other complications associated with fissile solution criticality e.g. the presence of radiolytic gases. The heating is achieved by introducing an electrolyte in the water and discharging a current of electricity through it. Power densities of 4 to 17 kW have been produced. The experiments are detailed: Test section is of height 25 cm, width 9.5 cm and length 8.2 cm, the total volume is 1.95 litres. The mass of water is 1.95 kg. We treat the vessel used as a circular cylinder with a radius of 5 cm and a height of 50 cm filled with liquid up to 25cm. Our results are sensitive to the height of the solution due to changes in hydrostatic pressure effecting the saturation vapour temperature and the rise velocity of the vapour bubbles. The rise velocity feeds into the bubble size, as this is taken to be half the maximum diameter of a stable bubble, which determines the interface area density and therefore the rate of mass transfer between the phases.

The experiments first establish a steady state condition with a small super-heat and a small amount of vapour voidage; the power densities in this stage were in the range 0.2-0.9 kW/litre. This is followed by the introduction of a power pulse for a short duration of time. The cases we take use peak powers of 4.83 kW/litre and 17.1 kW/litre for 380 milliseconds. These two experiments were chosen for comparison purposes with FETCH as they represent two extreme's of the data set generated by Greenfield et al (1954) [20] and were also simulated in the level one model of MMR Williams [1]. Since the duration of the experiment is short we ignore heat losses other than the escape of water vapour out of the solution. We choose as our initial condition for the power pulse the preceding super-heat (approximately 0.35 Deg. C.) and void fraction of 1%. The latter is arbitrary and chosen to help match the experimental results. Detailed modelling in this situation would often take a nucleation site density which can again be arbitrarily defined to the estimated number density and therefore match the experiments, see [?]. We do not do this as the presence of radiolytic gas bubbles within the fissile solution transients provide plenty of nucleation sites.

A quick calculation reveals that for the 17.1 kW/litre experiment 0.034 g per 1 g of water will be vapourized and the resulting vapour takes up about 50 times the volume of the liquid water. The 4.8 kW/litre experiment will result in 14 times as much water vapour than water by volume. Thus, very substantial amounts of water vapour will result in both experiments.

We measure the volume fraction of vapour at a height of 12.5cm above the base of the container in figure 2, against time, and compare our results with MMR Williams (2012) [1] theory and Greenfield et al (1954) [20] experiments. Ignoring slip velocity on these time scales and since the vapour fraction is in agreement with the experiments the temperature or superheating at these points will also be due to the fact that the vapourization controls the temperature or superheating in these experiments - latent heat reducing the temperature of the liquid. In figure 3, the maximum temperature versus time for both experiments simulated are shown.

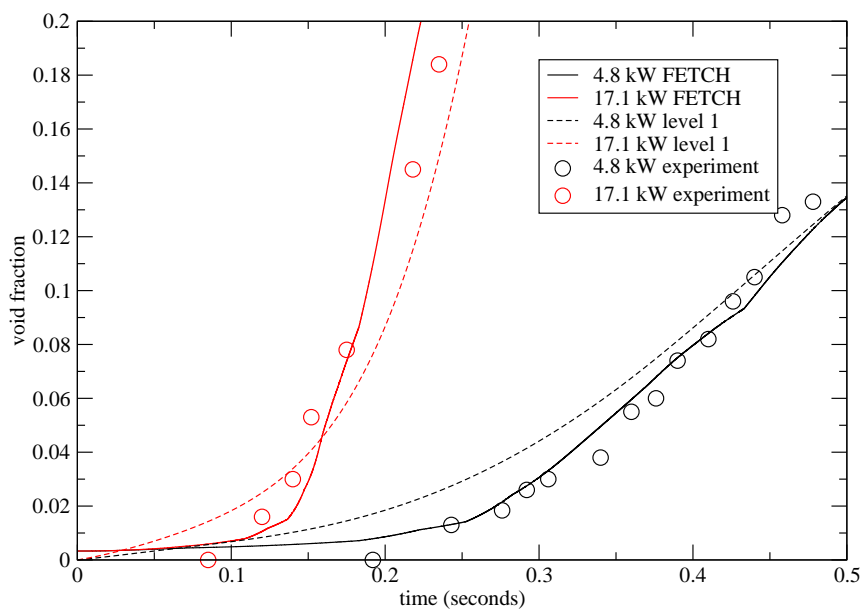


Figure 2: Volume fraction of vapour versus time. MMR Williams (2011) [1] theory and Greenfield et al (1954) experiments in which red circles = the experiment with 17.1kW and black circles= the experiment with 4.8kW. The FETCH-MIPS vapour fraction is taken at 12.5 cm height.

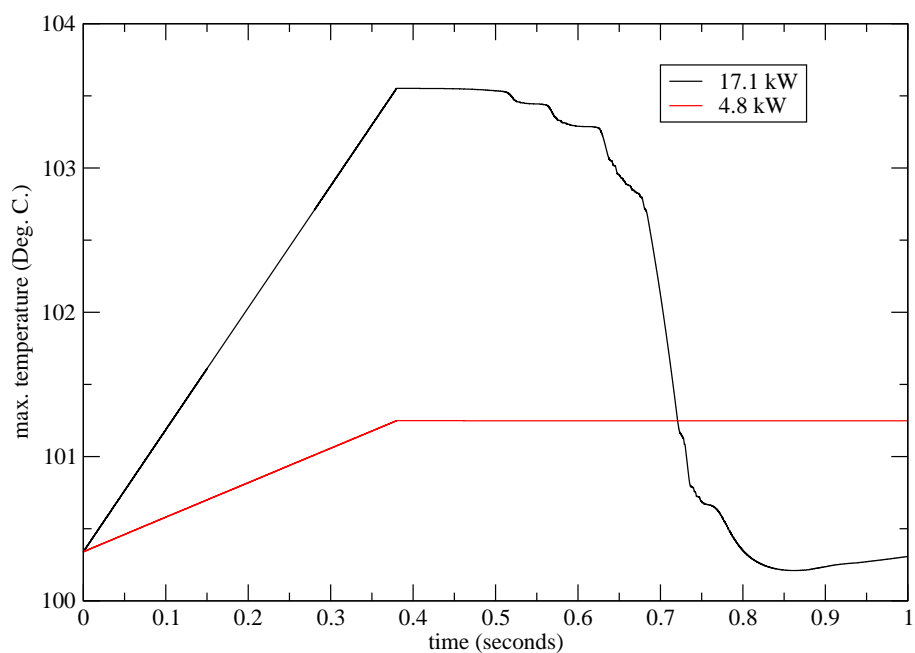


Figure 3: Maximum temperature versus time for FETCH-MIPS and the two volumetric heating experiments performed by Greenfield et al (1954).

5.2 CRAC geometry homogeneous boiling simulations with netronics coupling

Here a number of transients within the CRAC38 geometry and solution are modelled with varying step reactivity insertions of 1.9\$, 2.1\$, 2.3\$. The solutions are preheated to 60 Deg. C. in order for the radiolytic gases not to dominate the transients and allow the boiling physics to be observed. The aim of these simulations is to explore the physics of boiling, in the presence of radiolytic gases produced by rapid transients.

5.2.1 Time variation graphs

Graphs of power, maximum temperature, maximum pressure and maximum velocities *versus* time are shown in Figs. 4, 5, 7, 8 up to 1.4 seconds into the transients. Within these transients boiling of the solution reduces the reactivity of the systems due to increase in neutron leakage. However, this negative feedback has a time delay associated with it allowing substantial super-heating of the solutions up to a maximum of 15 Deg. C. above the saturation vapour temperatures, see Fig.5. The time delay also means that there is little difference observed between the maximum fission rates for simulations performed with and without boiling. However, there is a substantial difference in the total yields of these simulations with and without boiling, as the expansion of the solutions with vapour production after the first fission spike more rapidly reduce the reactivity and therefore power of the systems. In addition, the pressure of the system in the larger reactivity insertions is large and does effect the saturation vapour temperature, see Fig.1, which means that there are oscillations in the generation and condensation of vapour. Notice also the very substantial liquid and even greater gas velocities generated for the larger reactivity insertions, Figs. 7,8.

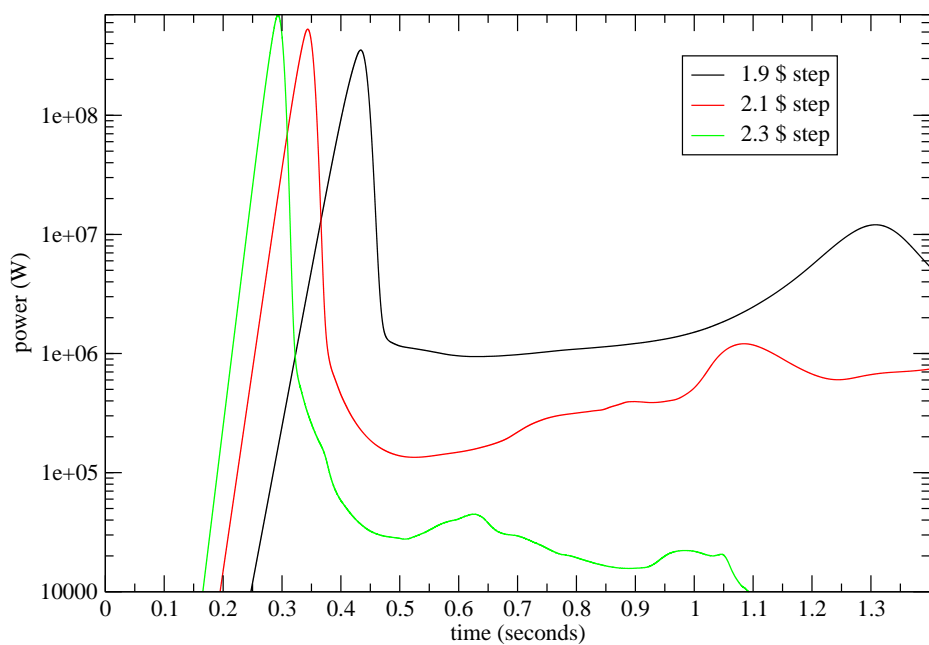


Figure 4: Power versus time for varying step reactivities and for the CRAC 38 geometry and solution.

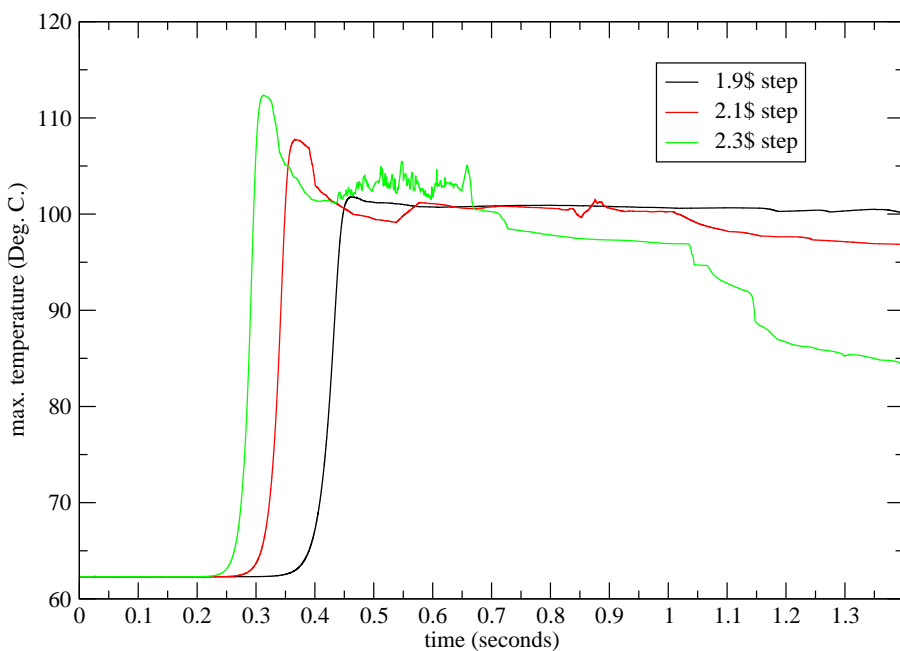


Figure 5: Maximum liquid temperature versus time for varying step reactivities and for the CRAC 38 geometry and solution.

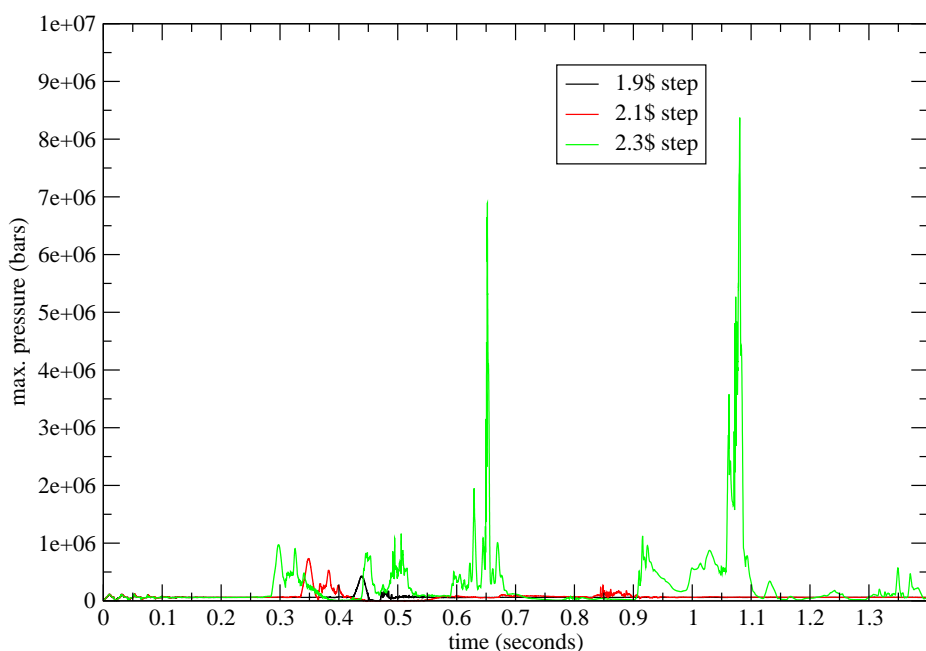


Figure 6: Maximum pressure deviation from atmospheric pressure versus time for varying step reactivities and for the CRAC 38 geometry and solution.

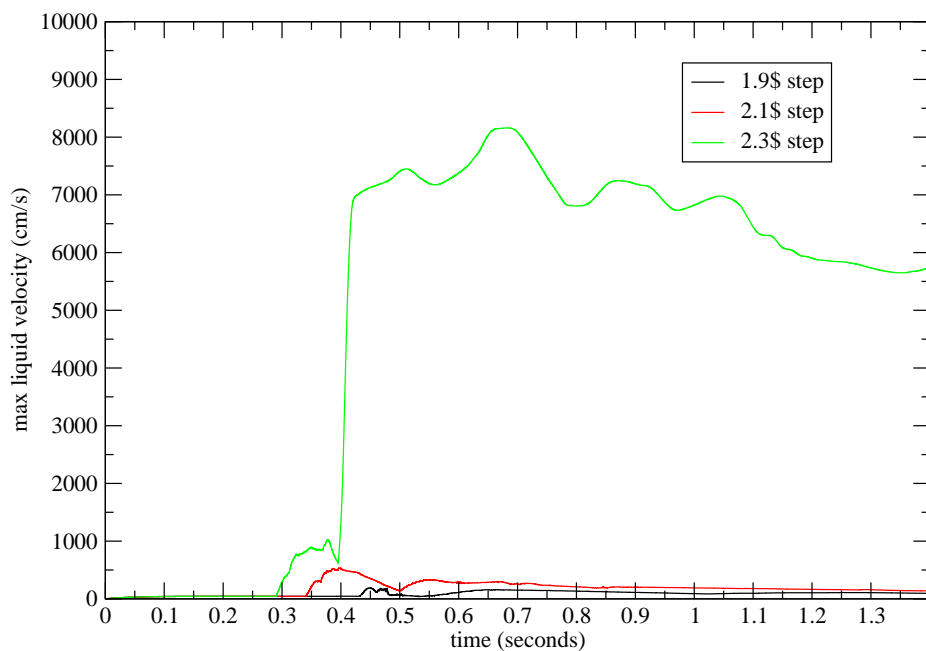


Figure 7: Maximum liquid velocity versus time for varying step reactivities and for the CRAC 38 geometry and solution.

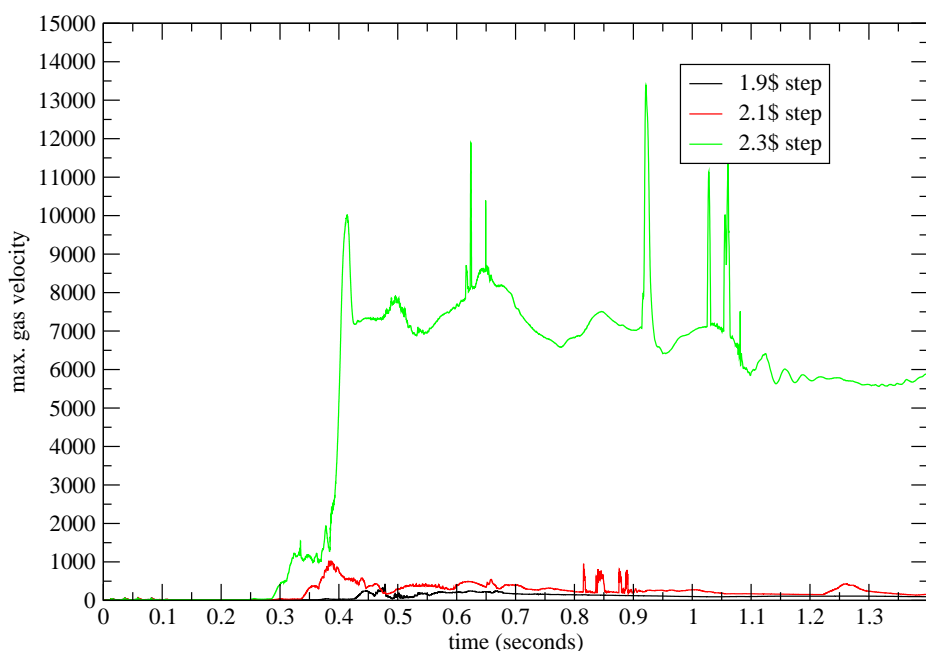


Figure 8: Maximum gas velocity versus time for varying step reactivities and for the CRAC 38 geometry and solution.

5.2.2 Snapshots of spatial distributions

We have shown a number of key fields (liquid volume fraction, liquid temperature, normalized vapour concentration, normalized radiolytic gas concentration in the gas phase) at six instances in time for the 1.9 \$ step in Figs. 9,10,11,12,13 for the 2.1 \$ step in Figs. 14,15,16,17,18 and for the 2.3 \$ step in Figs.19,20, 21,22,23. These three simulations are believed to cover a wide range of the dynamics of step reactivities with boiling.

For the 1.9\$ step we have only a small amount of super-heating of the order of a degree, which quickly disappears, as vapour is produced and the maximum temperature relaxes towards the saturation vapour temperature. This results in a pocket of gas being deposited inside the solution, see Fig.9c. The gas in this pocket contains a mixture of vapour, see Fig.11c, and radiolytic gases Fig.12c. The normalization coefficients are such that at atmospheric temperature and pressure the normalization results in the volume fractions of these two gas components. Thus, these may be seen as volume fractions in this instance as the pressures in the system are not large enough to substantially change the gas volumes. Much of the radiolytic gases are those initially dissolved in the solution and liberated into the gas phase when the liquid vapourises. As the pocket of gas rises the vapour condenses leaving mostly radiolytic gases in the pocket.

The 2.1\$ step reactivity insertion deposits enough energy for there to be substantial super-heating (max of about 10 Deg. C) which again quickly relaxes towards the saturation vapour temperature as the liquid turns to vapour. This generates a large quantity of water vapour trapped in the solution which undergoes an oscillatory expansion Fig. 14b and contraction Fig.14c as subsequently the trapped pocket of vapour rises to the surface. Again, the vapour rapidly condensing at it approaches the free surface, see Fig.14d,e,f. It should be noted that the vapour just after the fission spike is close to the saturation vapour temperature, see Fig.15c, although it does undergo small changes due to the work done by pressure, see r.h.s. of equations 31, 32. Notice that the radiolytic gas bubbles mostly exist on the fringes of the large pockets of gas, see Fig. 17 and in particular Figs. 17c,d. This seems to be true of all of the larger reactivity insertions simply due to the large quantities of vapour produced. Interesting flow patterns can be seen inside the gas pocket that are characteristic of the flow of gases in vapour bubbles, see Figs. 18 and in particular Fig. 18e.

For the largest 2.3\$ step reactivity insertion simulation there is substantial super-heating of the order of 15 Deg. C. which again quickly relaxes towards the saturation vapour temperature. The quantity of vapour produced is enough to throw much of the liquid out of the container.

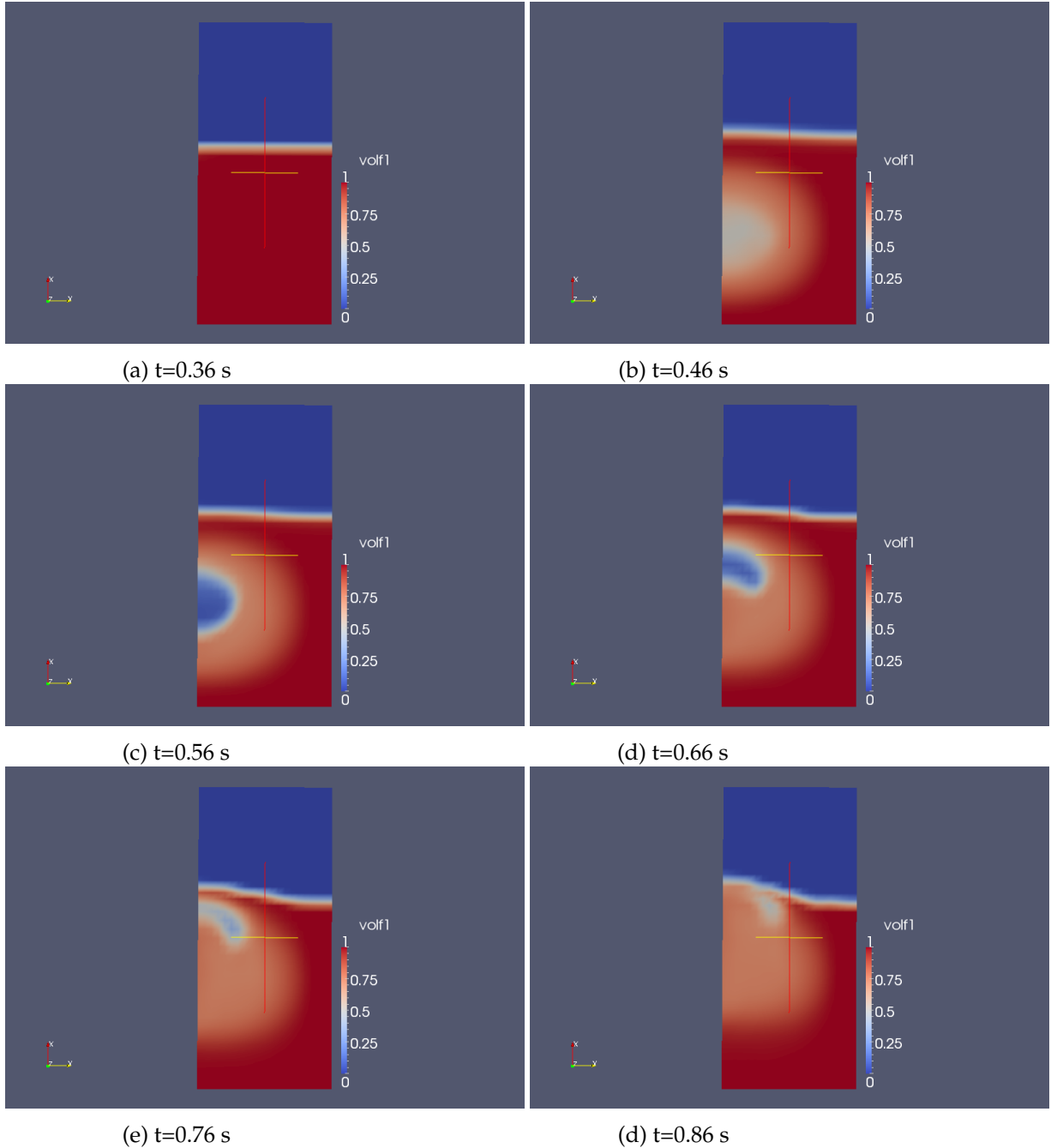


Figure 9: For the 1.9% step reactivity insertion and CRAC geometry and solution the snapshots of volume fraction at various instances in time.

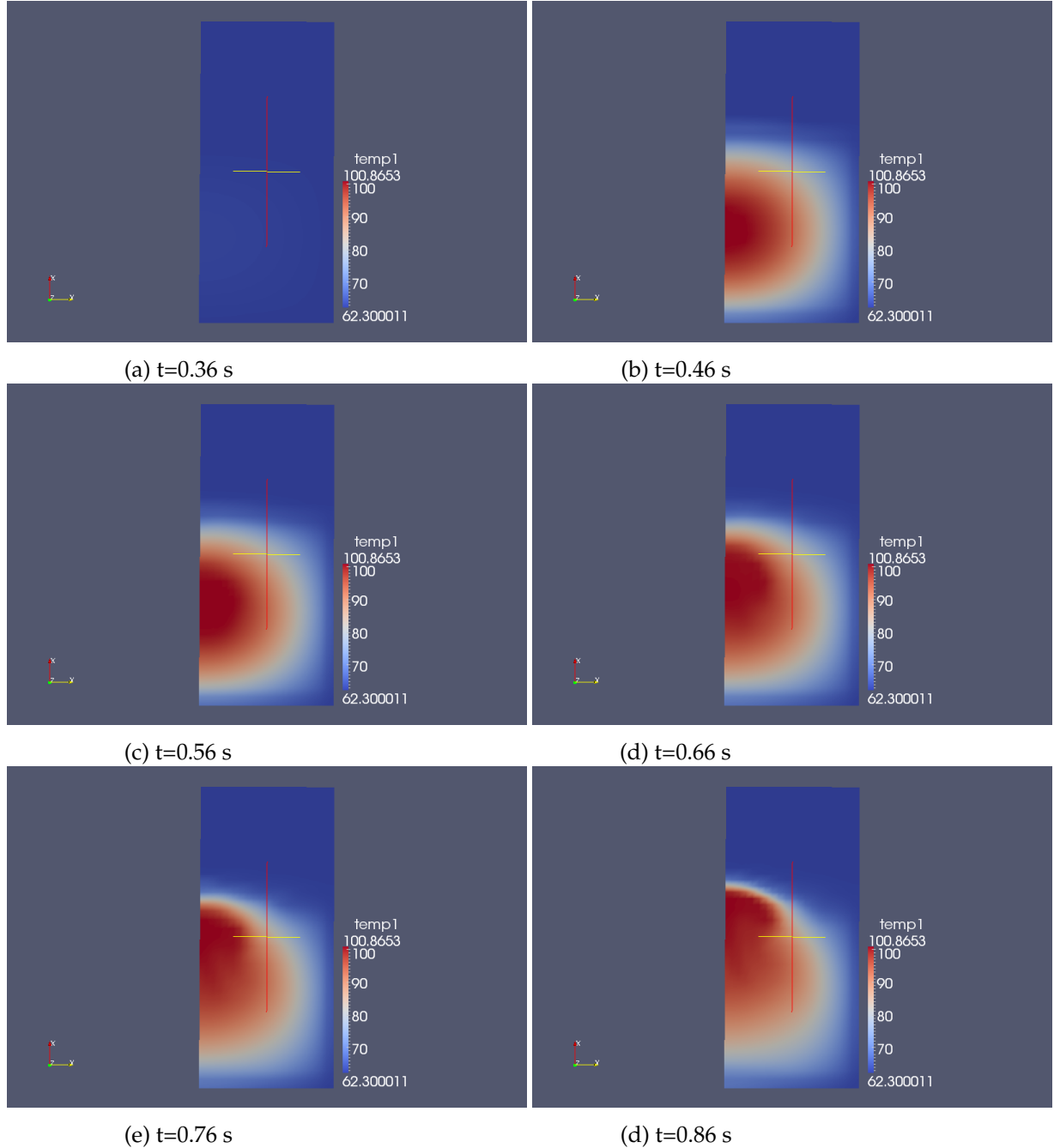


Figure 10: For the 1.9\$ step reactivity insertion and CRAC geometry and solution the snapshots of liquid temperature at various instances in time.

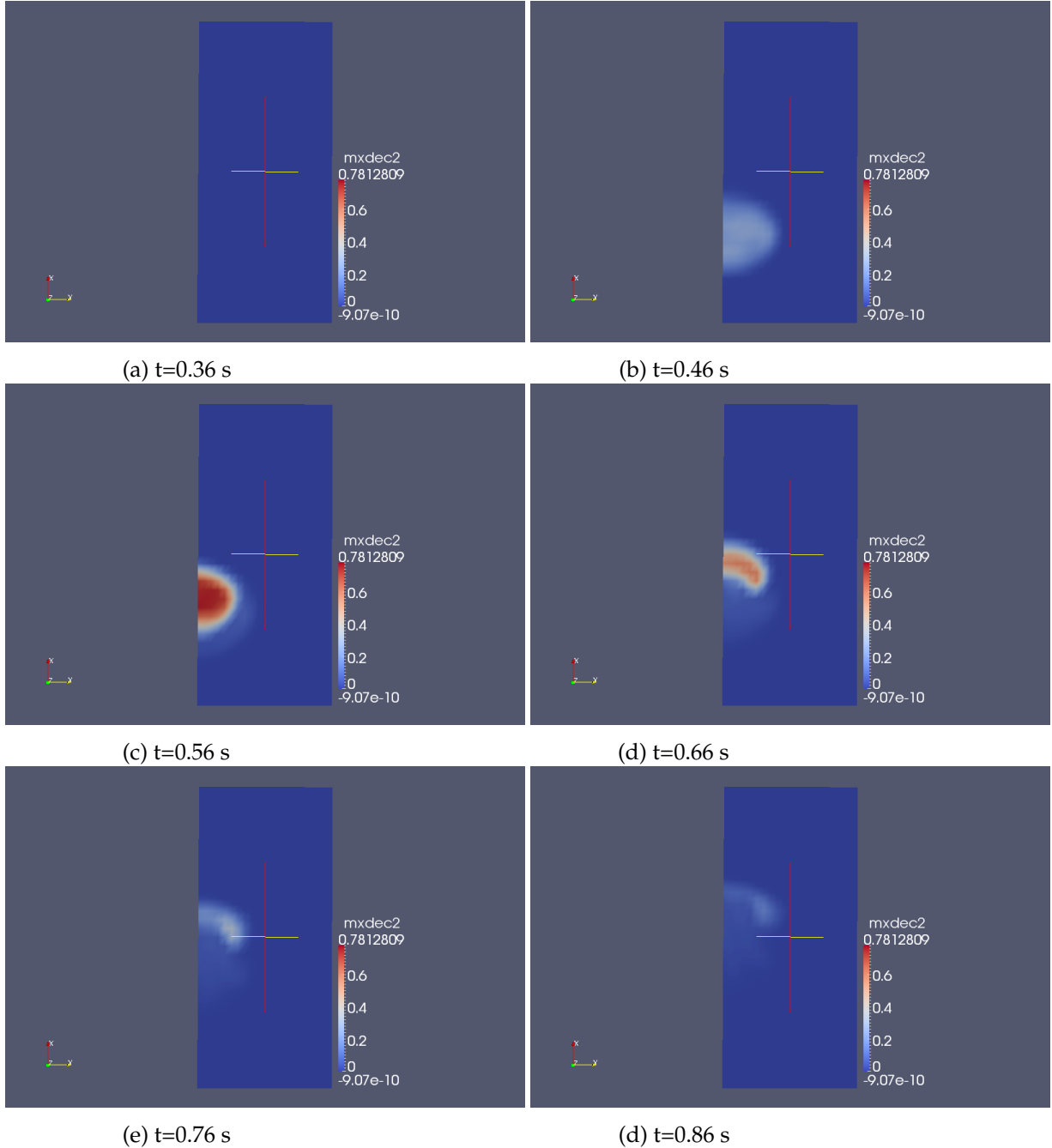


Figure 11: For the 1.9\$ step reactivity insertion and CRAC geometry and solution the snapshots of normalized vapour concentration at various instances in time.

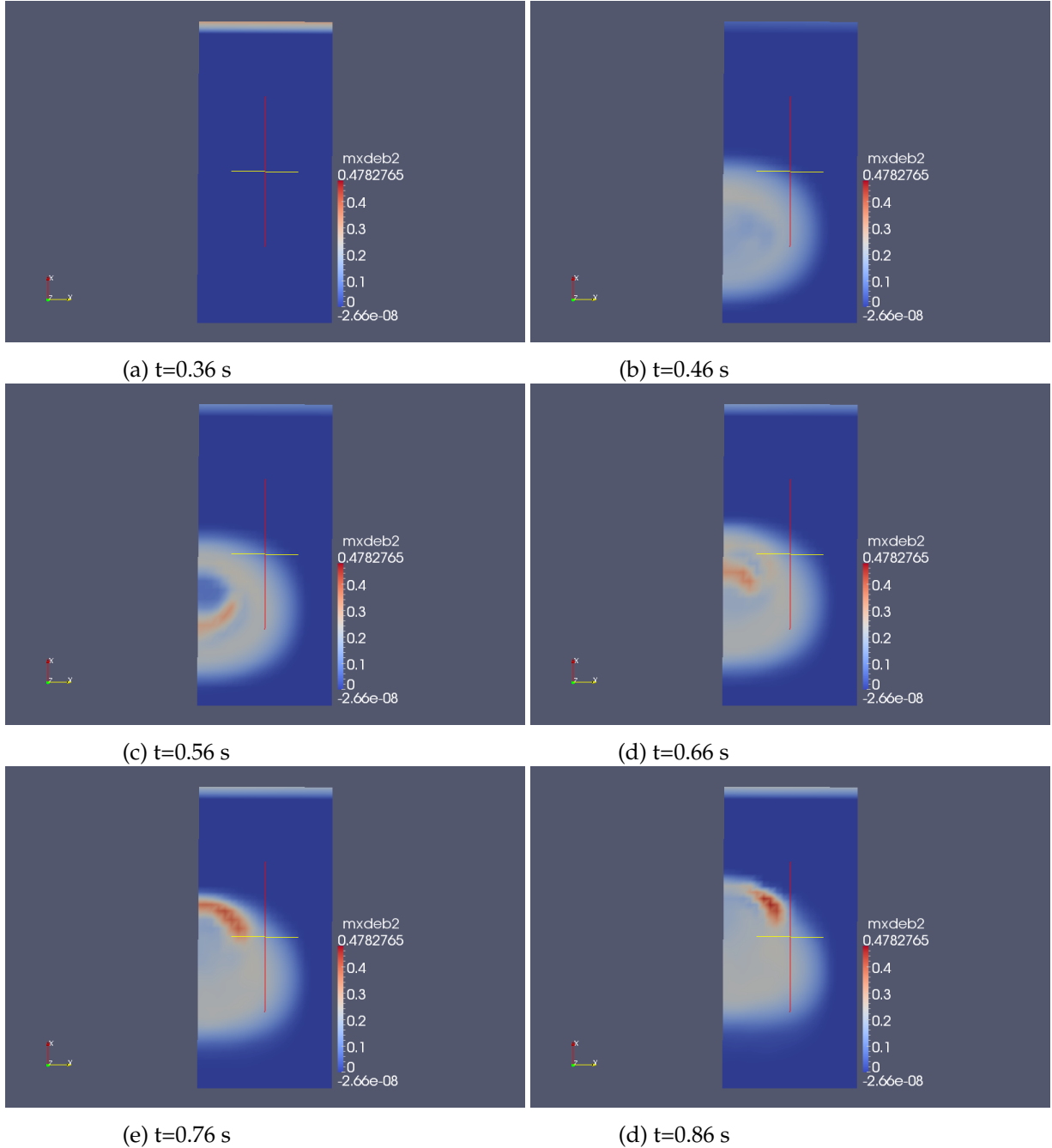


Figure 12: For the 1.9\$ step reactivity insertion and CRAC geometry and solution the snapshots of normalized radiolytic gas in gas phase concentration at various instances in time.

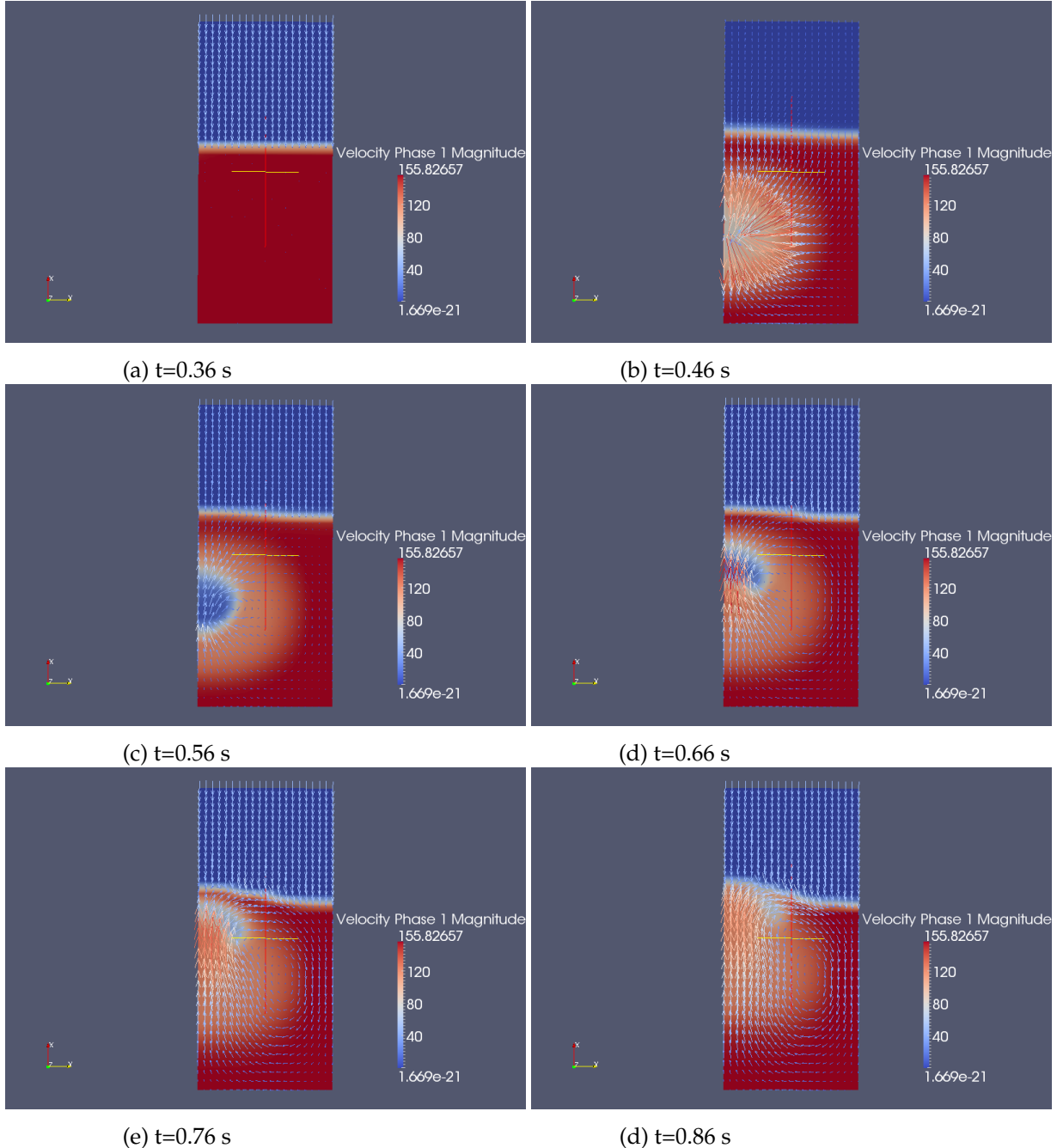


Figure 13: For the 1.9\\$ step reactivity insertion and CRAC geometry and solution the snapshots of liquid velocity and volume fraction at various instances in time.

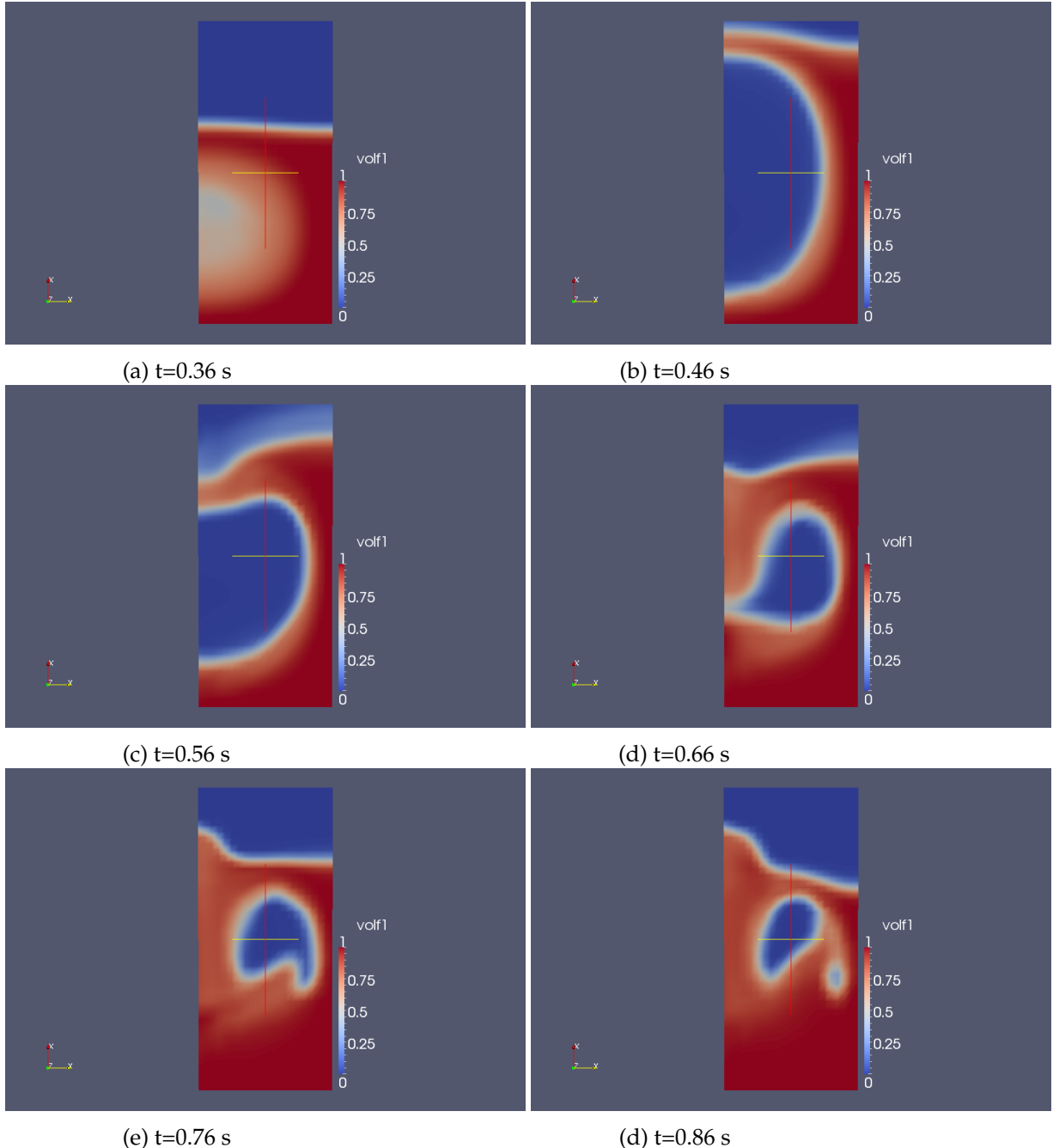


Figure 14: For the 2.1\$ step reactivity insertion and CRAC geometry and solution the snapshots of volume fraction at various instances in time.

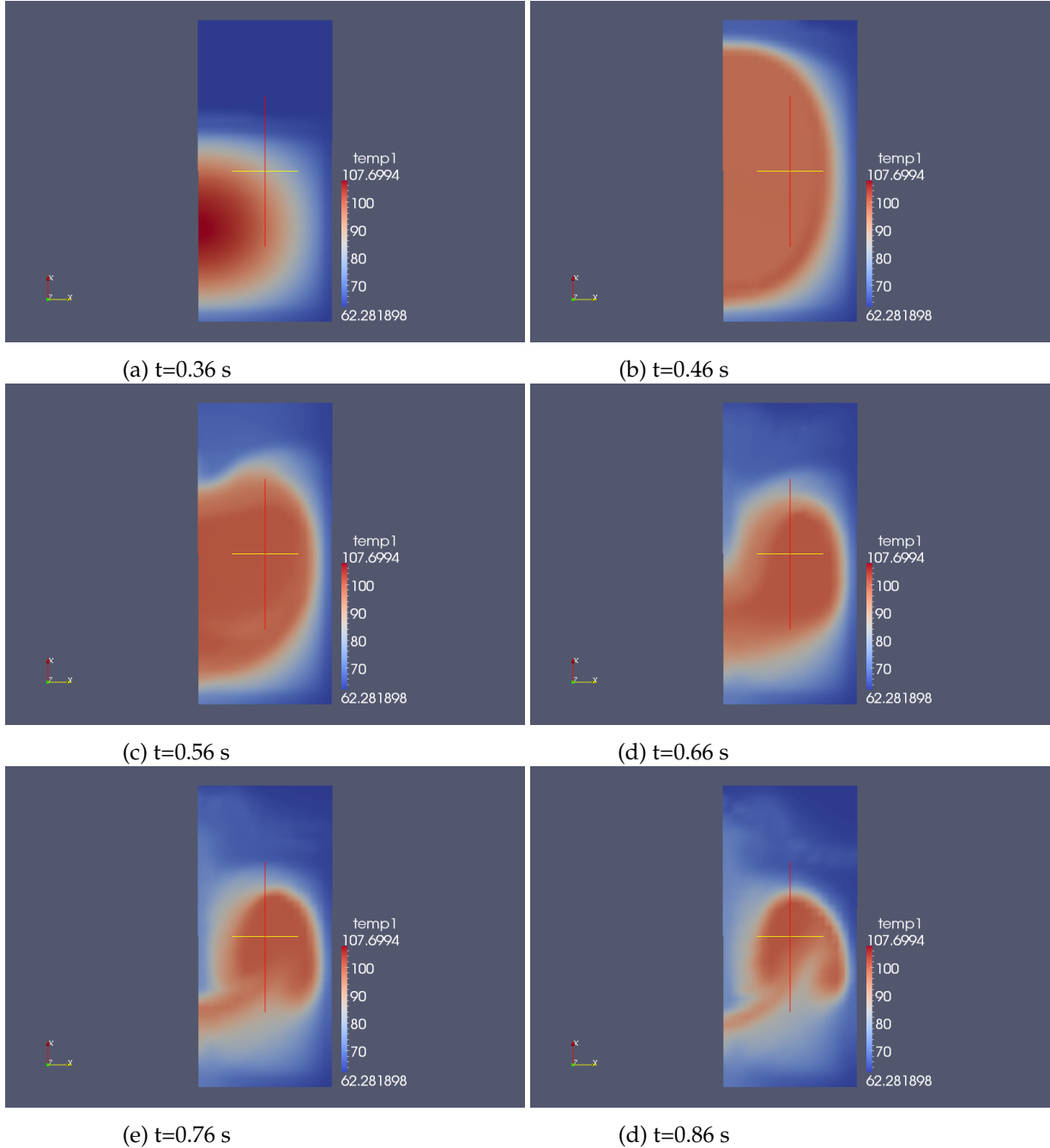


Figure 15: For the 2.1\$ step reactivity insertion and CRAC geometry and solution the snapshots of liquid temperature at various instances in time.

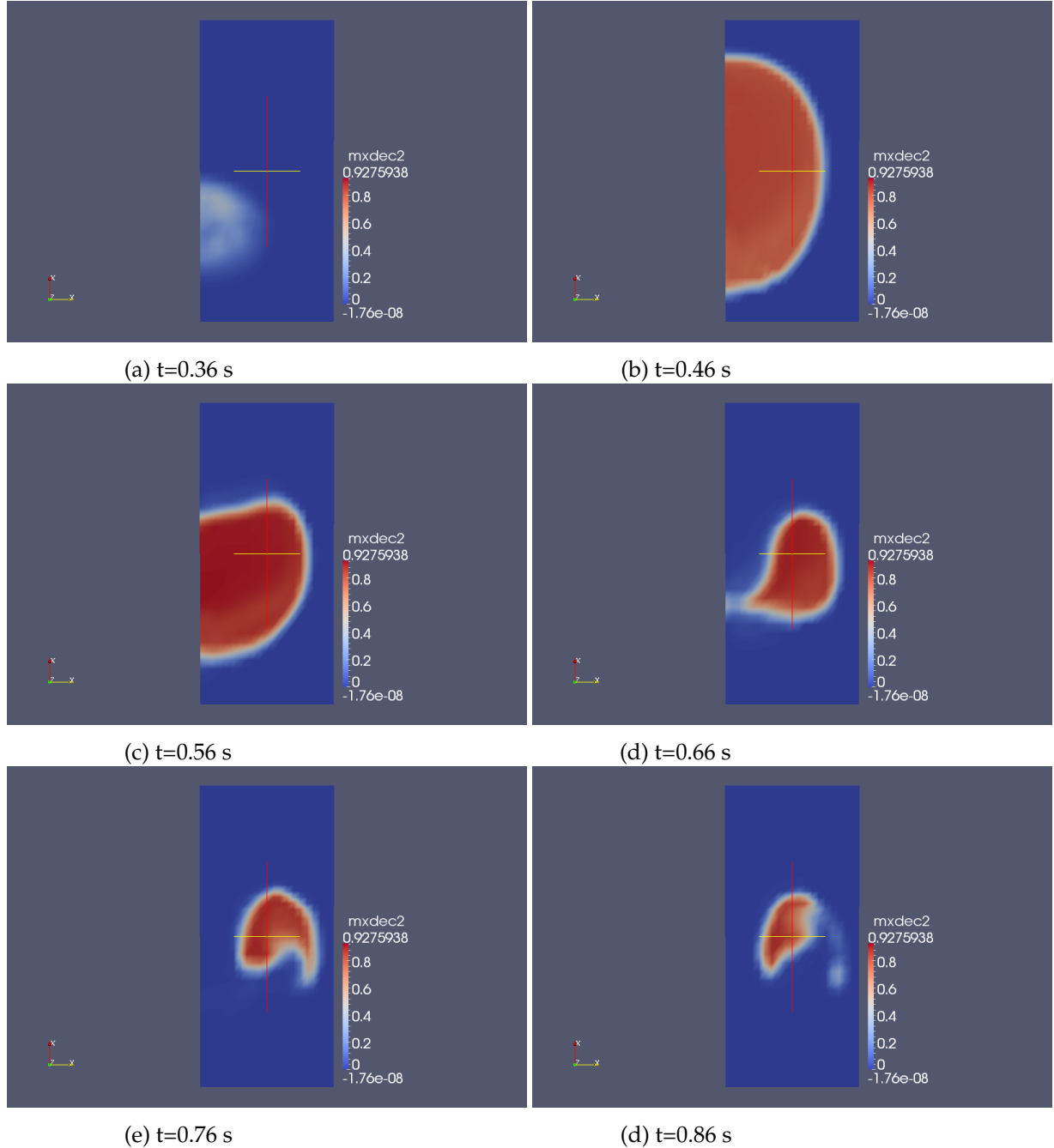


Figure 16: For the 2.1\$ step reactivity insertion and CRAC geometry and solution the snapshots of normalized vapour concentration at various instances in time.

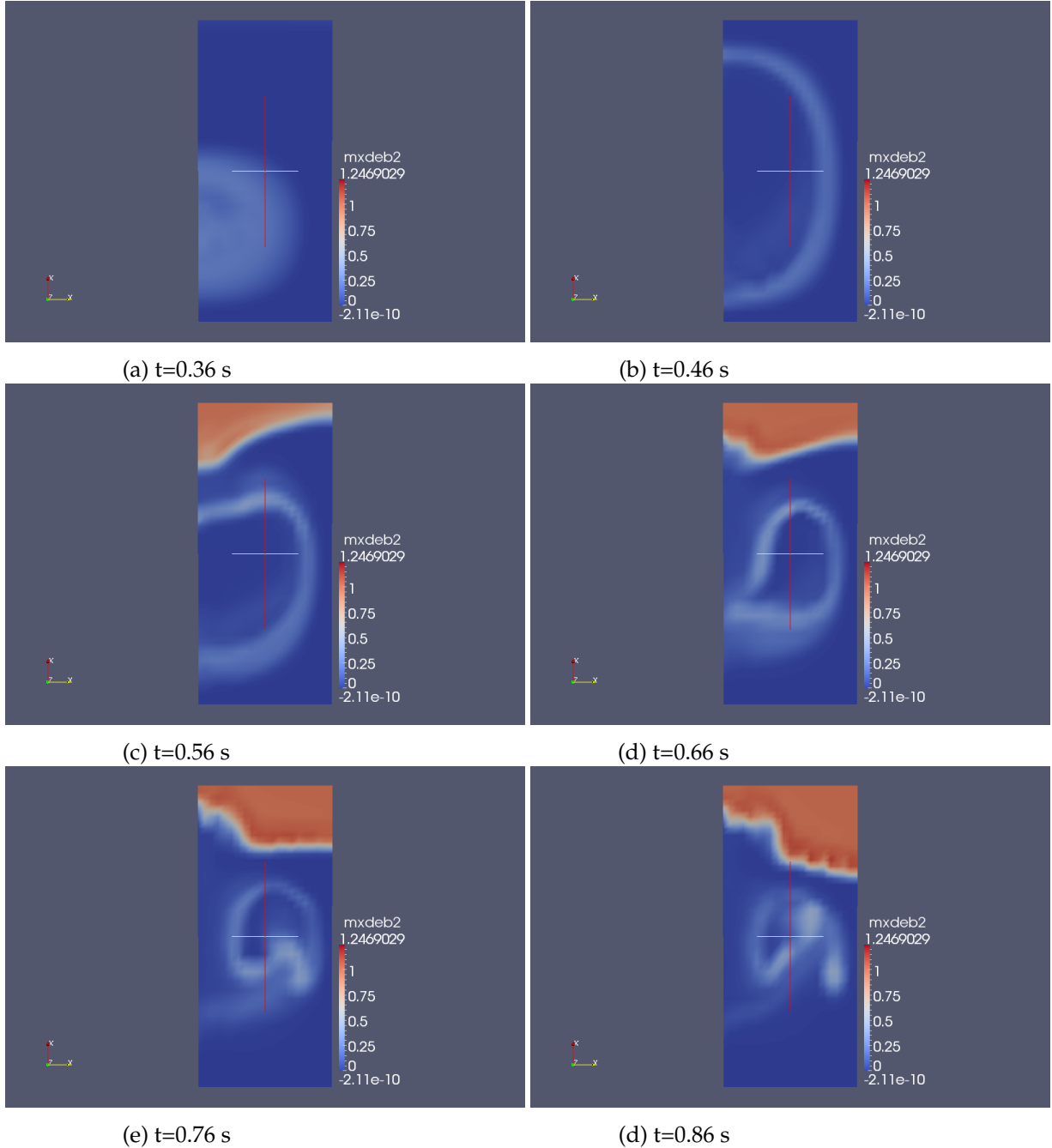


Figure 17: For the 2.1\$ step reactivity insertion and CRAC geometry and solution the snapshots of normalized radiolytic gas in gas phase concentration at various instances in time.

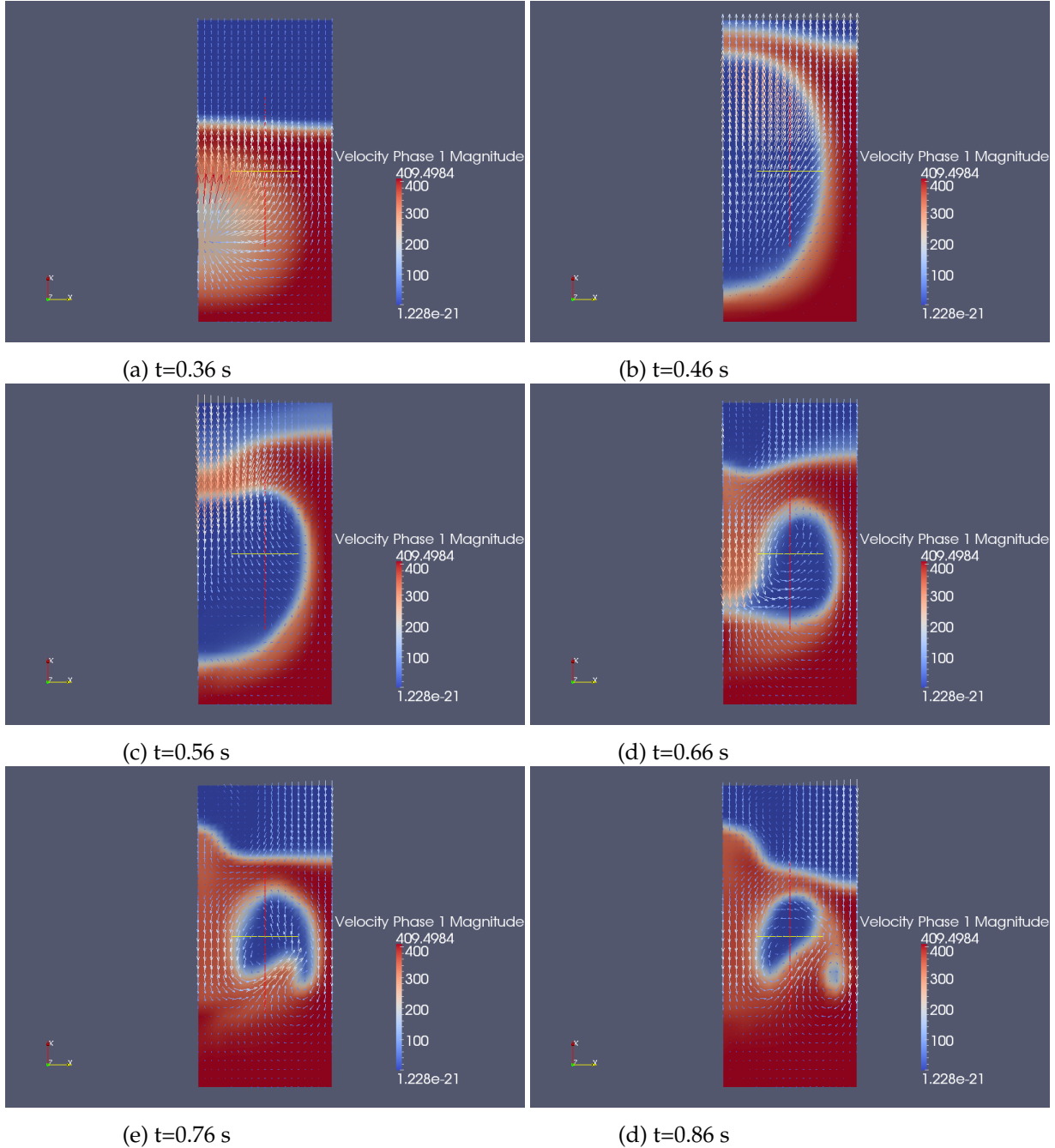


Figure 18: For the 2.1\$ step reactivity insertion and CRAC geometry and solution the snapshots of liquid velocity and volume fraction at various instances in time.

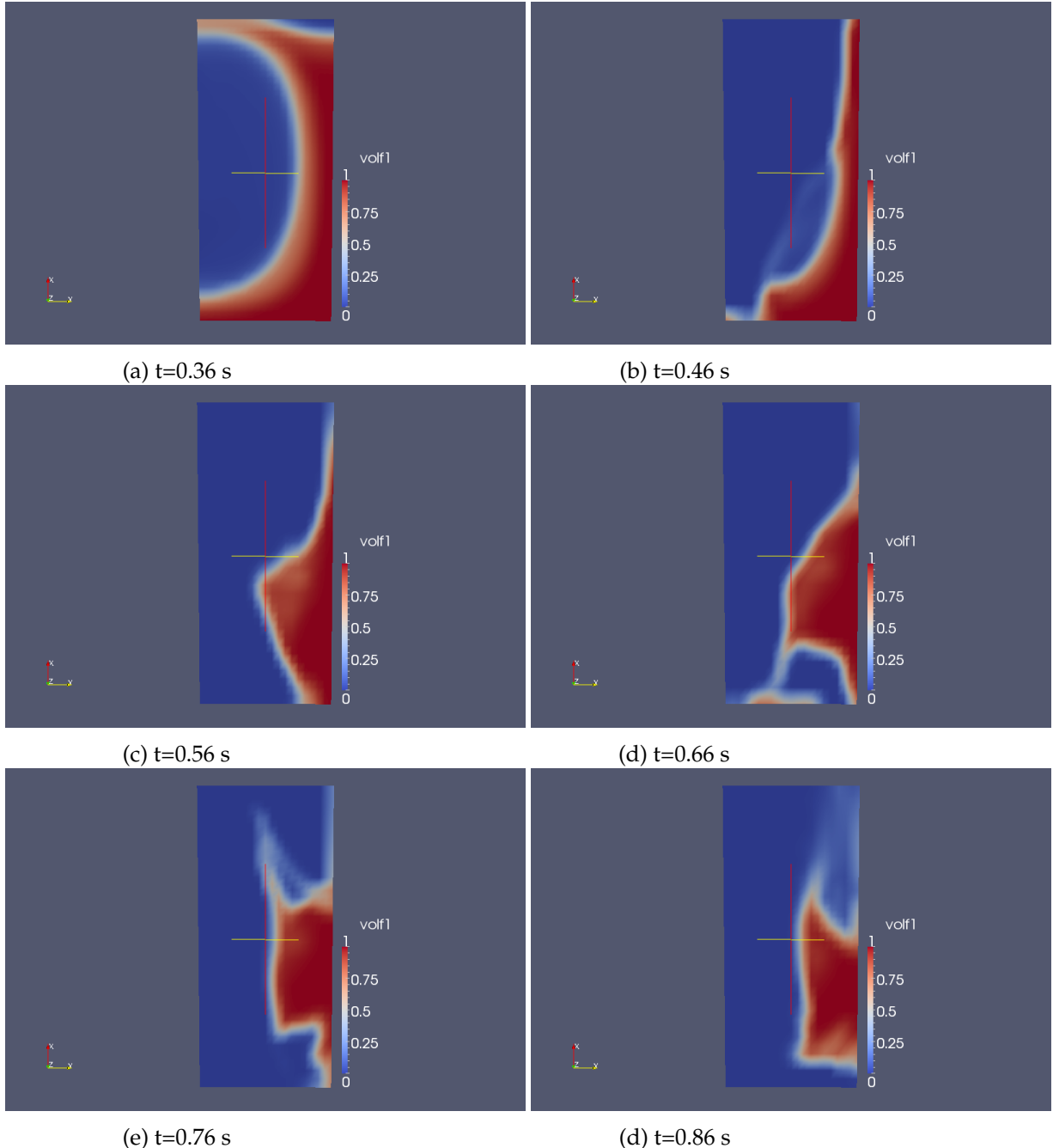


Figure 19: For the 2.3\\$ step reactivity insertion and CRAC geometry and solution the snapshots of volume fraction at various instances in time.

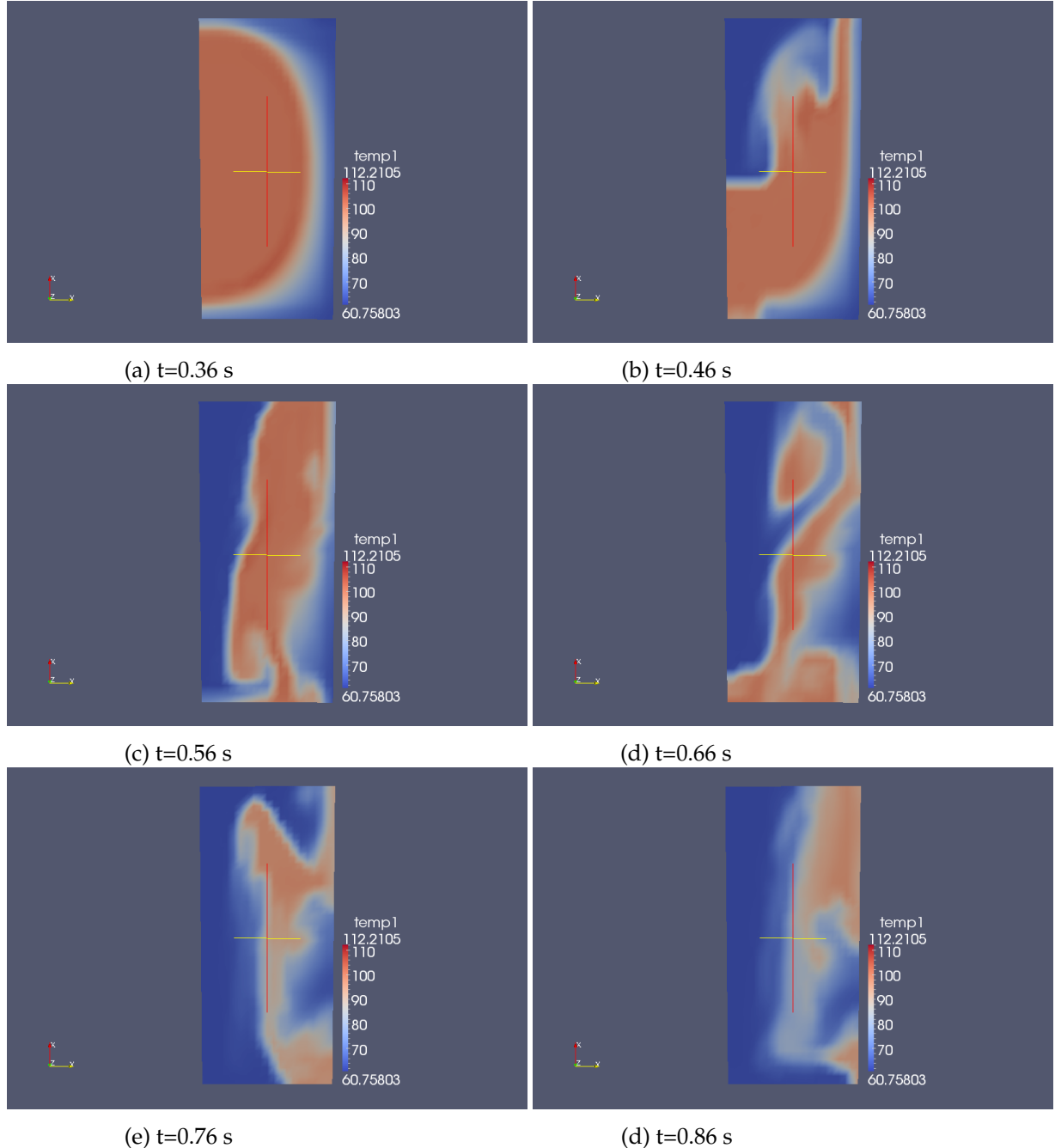


Figure 20: For the 2.3\$ step reactivity insertion and CRAC geometry and solution the snapshots of liquid temperature at various instances in time.

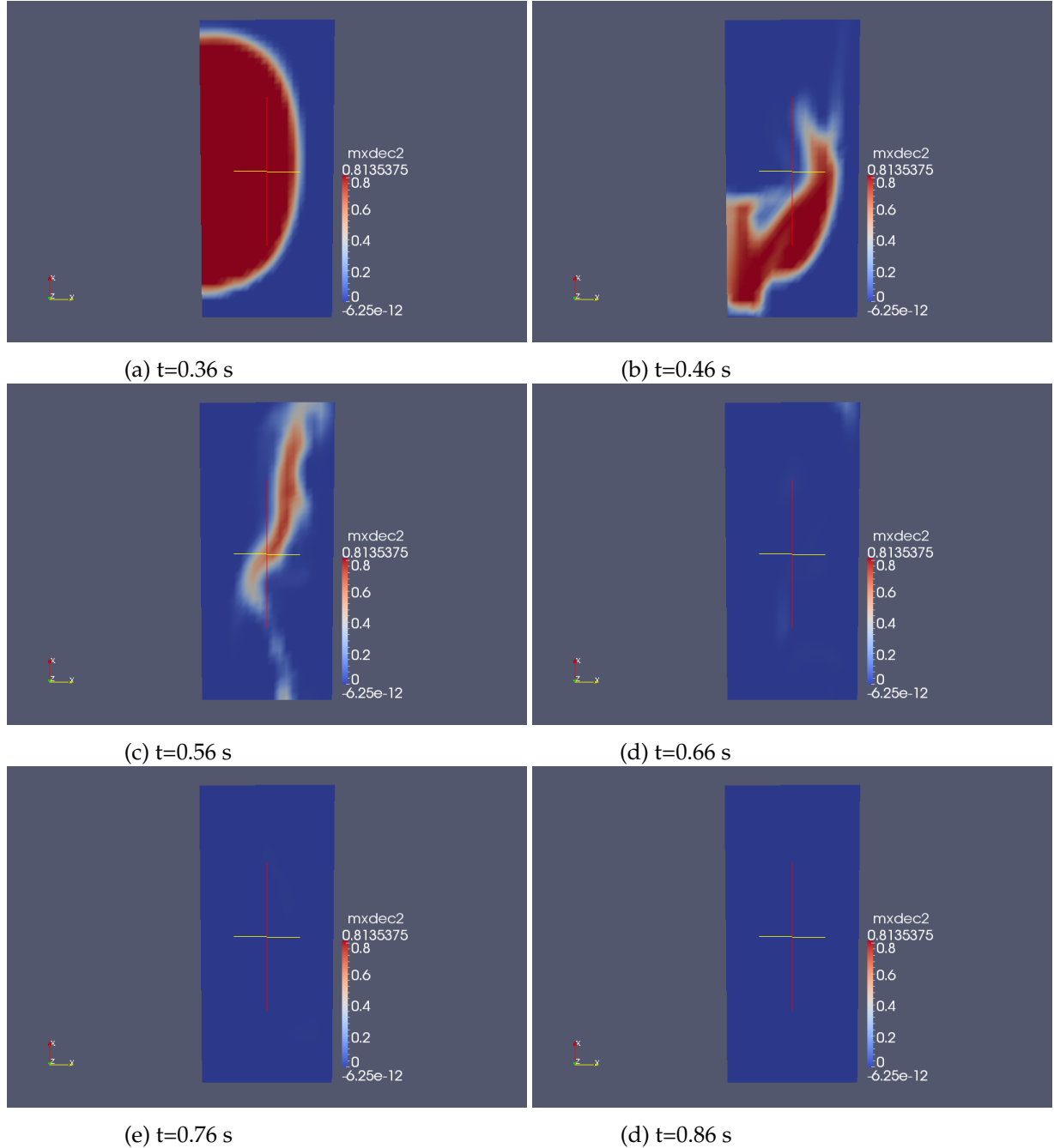


Figure 21: For the 2.3\$ step reactivity insertion and CRAC geometry and solution the snapshots of normalized vapour concentration at various instances in time.

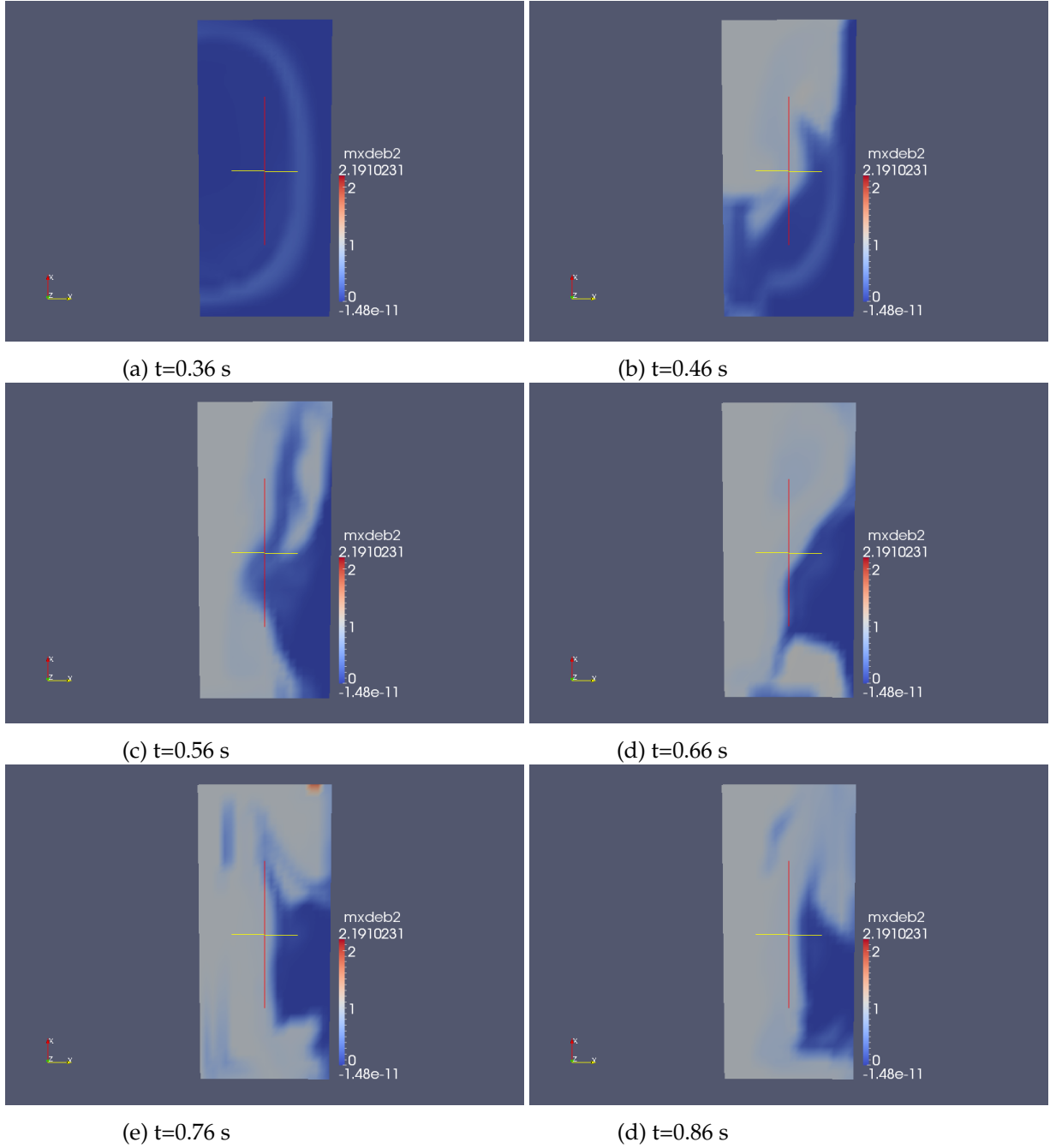


Figure 22: For the 2.3\$ step reactivity insertion and CRAC geometry and solution the snapshots of normalized radiolytic gas in gas phase concentration at various instances in time.

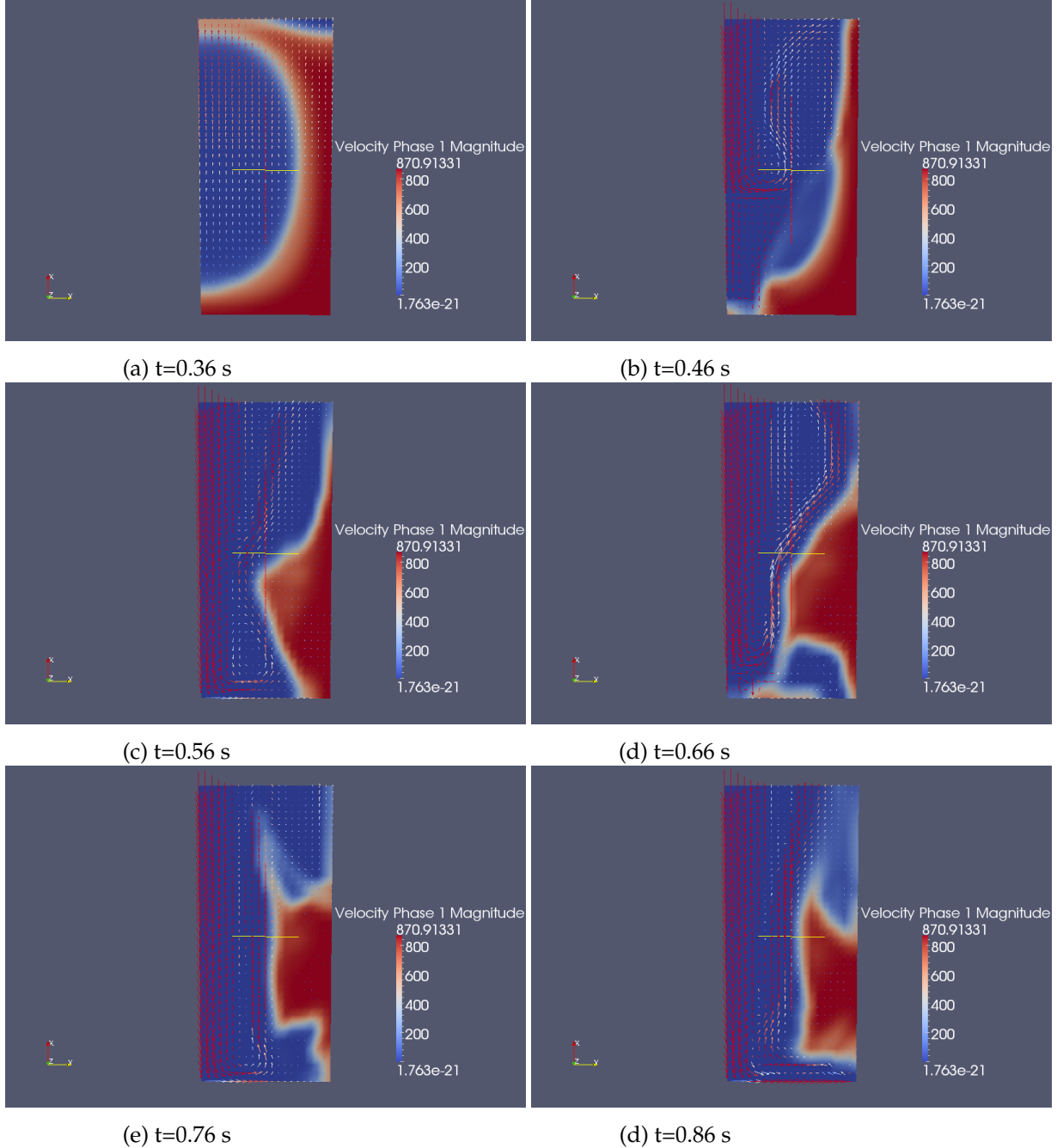


Figure 23: For the 2.3\$ step reactivity insertion and CRAC geometry and solution the snapshots of liquid velocity and volume fraction at various instances in time.

5.3 CRAC 43 simulation with boiling

The experiment CRAC 43, described by Barbry et al. (1971), was performed in a vessel of 80 cm diameter. See also the CRAC43 modelling work of [2] and experimental results in [21], [22], [23], [24]. The liquid is uranyl nitrate solution, 93 percent enrichment, a concentration of 200 g/litre of uranium and with a free acid molarity of 2. The tank, of diameter 80cm, is filled with solution at room temperature, from the base of the drum at a rate of 1410 l/h. Liquid addition was terminated 19 s after the solution became critical. A 2-D axi-symmetric (R-Z) simulation is reported here. The solution has an initial height of 15.6cm, at which $K_{eff} = 1$, according to diffusion theory, and the neutron source was uniformly distributed. Thus, no attempt at simulating pre-critical multiplication is made. Converged angular resolution, using transport theory, provides a critical height of 14.4 cm, in agreement with the measurement of 14.38cm. Other tests indicate that, despite this small height difference, effects due to energy and void deposition will be similar for both cases - and it is on these that we have focussed. The variations of K_{eff} with temperature and solution height are shown in figure 24.

Boiling occurred between 40 and 60 s in the experiment. After about 60 s some unexpected power bursts occurred, followed by a sudden superheat which was measured by a thermocouple. Barbry et al. (1971) reported that an unknown amount of liquid was ejected from the vessel at that time.

Barbry et al. (1971) stated: "For power excursions subsequent to high reactivity (several \$), it was observed during the CRAC and SILENE experiments that the boiling temperature of the solution was reached for an energy corresponding to about 1.1×10^{16} fissions per litre. These data are valid for a power excursion lasting for a few minutes and for a system without any forced cooling"

5.3.1 Bubbles

There is a relatively long delay after the first power spike, shown in figure ??, before radiolytic gas is released into bubbles; this is due to the small number of nucleation sites (modelled by small volume fraction of gas), absence of bubbles, and low radiolytic gas concentration. When subsequent fission spikes appear the solution is saturated with radiolytic gas and there is at least a small quantity of gas in bubbles, both promoting more rapid bubble production.

Fresh solution (at room temperature) can be seen in the vicinity of the inlet pipe, see figures ?? (a),(b),(c). The longest lived delayed neutron concentration reflects the temperature distribution: both have essentially the same source distribution and are affected similarly by advection - the release of delayed neutrons from the longest lived group being small on these time scales. The power spatial distribution reflects the shortest lived delayed precursor concentration.

5.3.2 Dynamics

The deposition of radiolytic gas and rapid conversion into bubbles near the free surface provides the dominant negative feedback effect and induces regular oscillations in the fission rate. There appears to

be a characteristic frequency of oscillation of fission spikes in figure ?? . This frequency will depend on the dimensions of the domain occupied by the liquid and the interphase drag on bubbles. Interphase drag determines the terminal velocity of bubbles and therefore the rate of release of bubbles out of the liquid. A bubble size of approximately $\frac{1}{2}\text{mm}$ was thought to be a representative bubble radius in the liquid, for the purposes of calculating interphase drag forces. The terminal velocity of a single bubble would then be 14 cm s^{-1} . This assumption proved to be incorrect as explained in this section.

Eventually, as the quantity of liquid inside the drum is increased, temperature effects are no longer sufficient to restrain the criticality of the system so that k_{eff} is approximates unity. Voidage due to bubbles takes on the restraining role and thus the quantity of bubbles present increases as more liquid is pumped into the system, see figures ?? (e),(f).

In this simulation, sloshing of the free surface is also a factor in determining the criticality of the system. Inspection of the time-dependent free-surface voidage maps highlights the effect of sloshing in leading to individual power peaks having significantly high or low amplitudes.

5.3.3 Advection processes

The liquid sets up a permanent recirculation (of negative vorticity) in which the liquid rises near the central axis, due to drag forces from rising bubbles (and to a lesser degree reduction in liquid density with increased temperature), and moves towards the wall at and near the free surface and then moves down the wall. Some of the bubbles can be seen to be dragged down the wall, see figure ?? (d). This circulation pattern smooths the radial distribution of gas in bubbles making it more one dimensional, see figure ?? (f). This recirculation pattern of the liquid can be seen superimposed on the temperature and longest lived delayed neutron precursor concentration fields, see figures ?? (b),(c).

Figures ?? shows various fields at $t=12.0$ seconds into the simulation. The concentration of dissolved radiolytic gas at the centre of the fluid domain, and towards the free surface, has been depleted because diffusion is larger (more bubbles having greater overall interphase surface area) and more time is available for the bubbles to form as the fluid rises. The shortest lived delayed neutron concentration, figure ?? (d), as always reflects the power distribution. The longest lived delayed group is more interesting, it contains mostly delayed neutrons from a previous large fission spike, which have been transported via advection, so that the largest concentration is nearer the walls. Figure ?? shows the fission rate versus time for this simulation.

5.3.4 Free surface waves

The oscillatory structure to the time series can be attributed to periodic bubble generation and loss out of the liquid and sloshing of the free surface. However, the waves travelling towards the central axis are often damped by rising bubbles before they reach the central axis. The time oscillations in power are qualitatively similar to those observed in CRAC 43, but the frequency is a factor of 1.5 larger. This

largeness is considered to be due to a too great a characteristic rise time (determined from the drag laws) used in the model, but the use of an axially symmetric model (which prevents waves from travelling across the whole vessel diameter) may also be a factor.

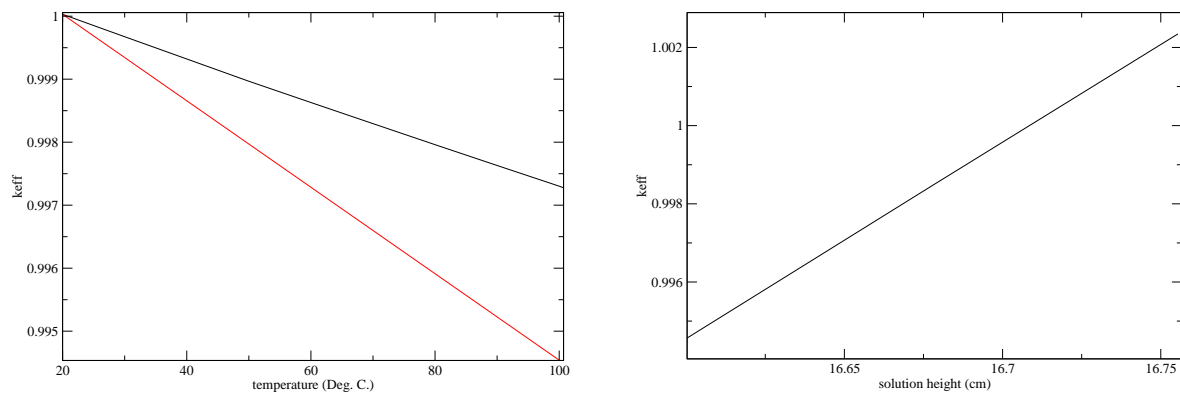


Figure 24: Left: K_{eff} against temperature - just the neutron temperature effect and the total effect (including density changes with temperature assuming atmospheric pressure) on K_{eff} of temperature changes. Right: K_{eff} against fissile liquid height at atmospheric pressure and a temperature of 20 Deg. C.

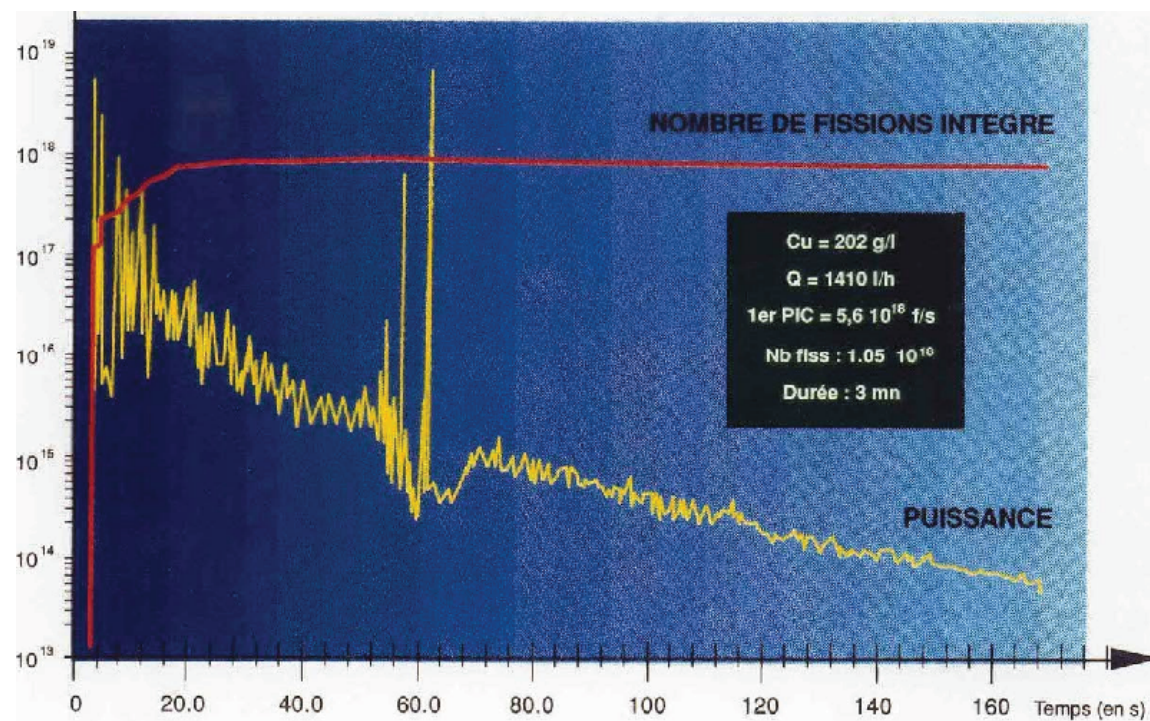


Figure 25: Fission power versus time for the CRAC 43 experiment taken from T. SCHULENBERG and J. DOHLER 1986 [2]

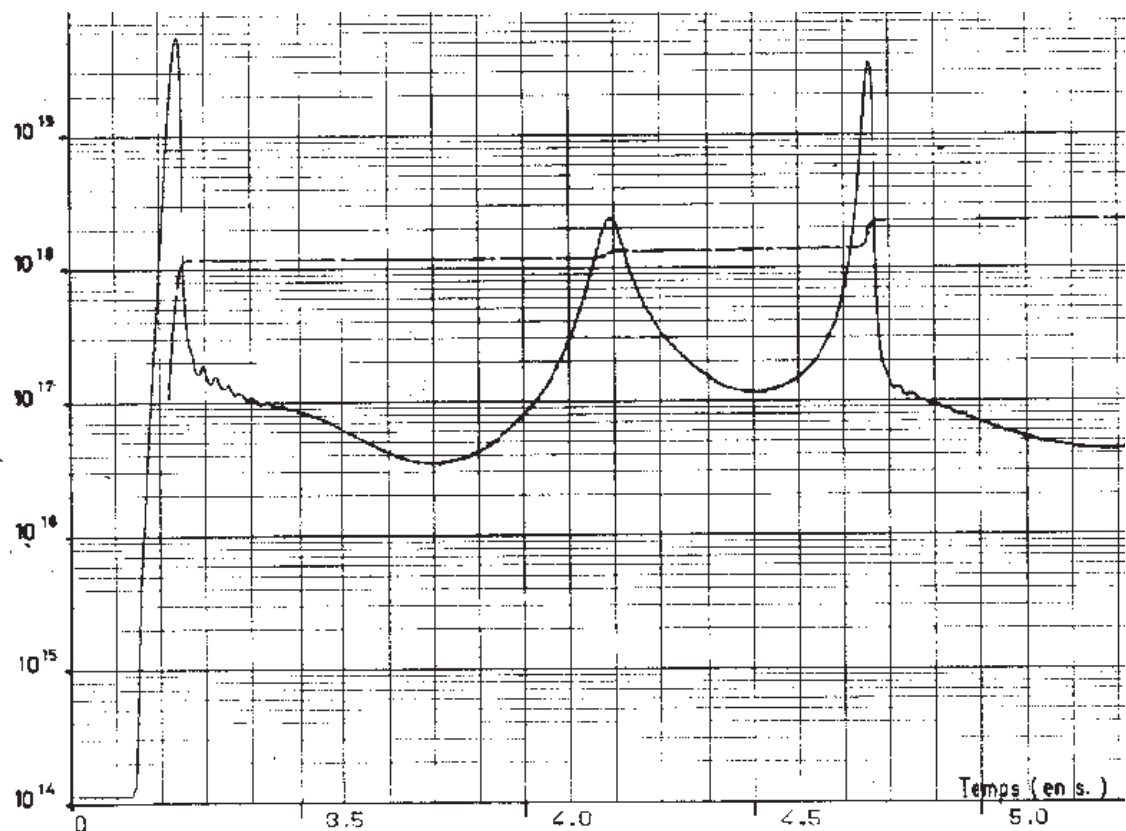


Figure 26: Fission power versus time for the CRAC 43 experiment taken from T. SCHULENBERG and J. DOHLER 1986, [2].

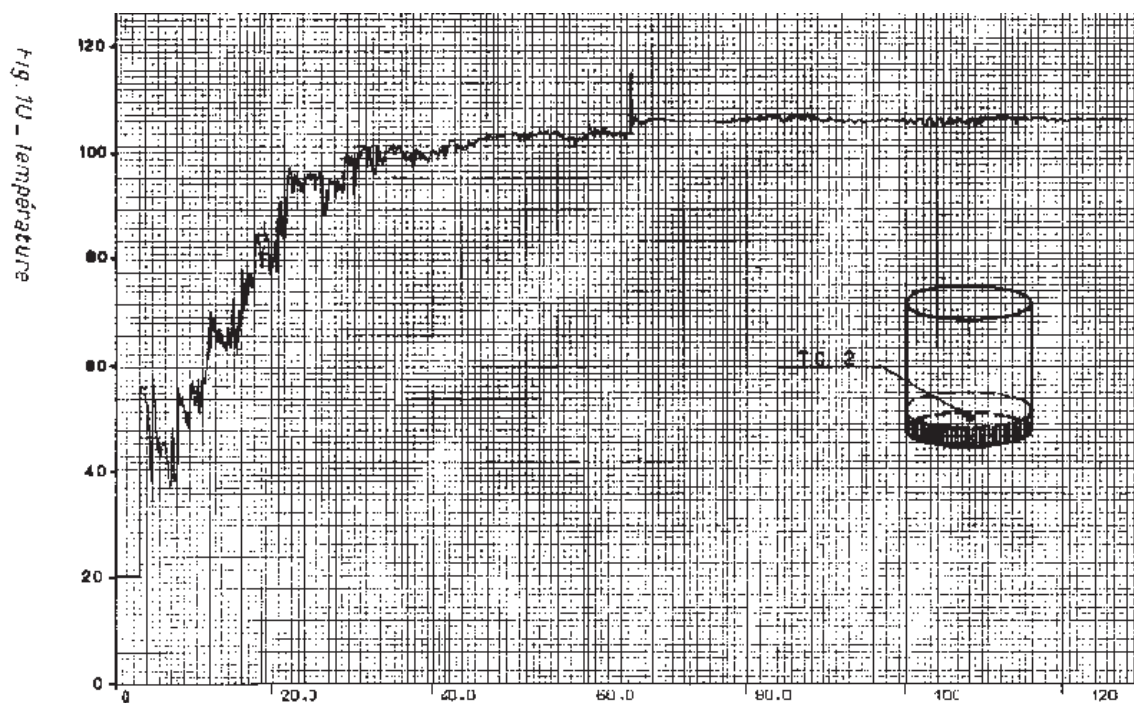


Figure 27: Temperature Deg. C. versus time for the CRAC 43 experiment taken from T. SCHULENBERG and J. DOHLER 1986, [2]. The position of the temperature measurement is indicated in the cylinder.

5.4 440kW MIPS simulation with boiling

The set up and material properties of this reactor are as described in previous topical reports. The major difference between this, and previous simulations, is that the control rode adjustment algorithm aims to produce a power output of 440kW and moves the control rode tip at a maximum velocity of 10cm/s. In addition, the simulation is initialized with a 90 Deg. C. temperature to minimize the spin up time of the reactor. The reactor will need to operate at around the boiling point of the solution to produce the 440kW power output and the boiling will contribute to the enhanced solution mixing that will enhance the heat transfer to the cooling coils. It may be possible to operate the reactor at larger powers, with even more vigorous boiling and radiolytic gas production, generating increased liquid velocities, which would further enhance the heat transfer to the cooling coils/pipes.

5.4.1 RZ MIPS configuration

The default set of conditions for the MIPS reactor simulations is described here. The geometry, showing the position of the cooling coils and the initial position of the fissile solution, is shown in Fig. 28. This geometry is discretised with 12265, 11988 rectangular bi-linear finite elements and nodes, respectively, in the fluids occupied part of the domain (inner vessel) and 19683, 20008 elements and nodes in the full domain. The inlet cooling water temperature to the pipes is 15.5 °C. There are 12 cooling pipes (Fig. 28) in which cooling water flows vertically upwards in the rz-geometry and each has a length of approximately 1200cm. The inner diameter of the pipes is 0.63 cm, which is cooling water occupied, and the outer diameter (the pipe is made of steel) is 0.9525cm. The mean cooling water speed in the pipes is 385 cm/s.

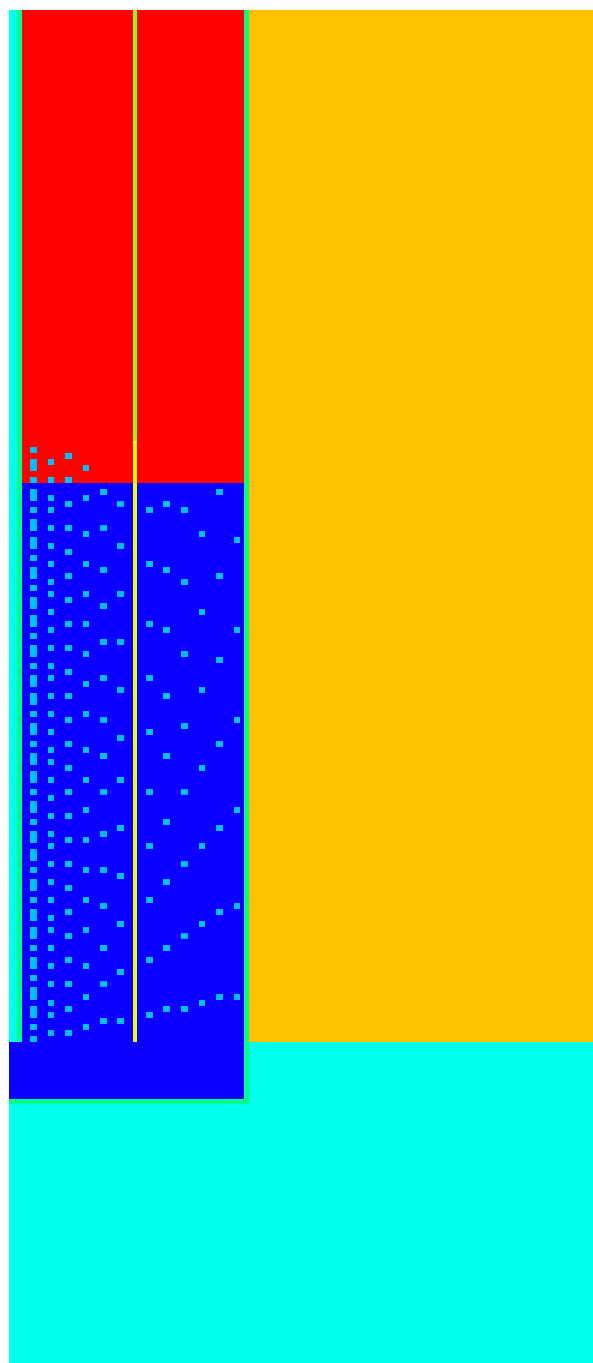


Figure 28: Geometry of the MIPS reactor used in the FETCH-MIPS model. Dark Blue: fuel solution; Red: gas; Yellow: Graphite; Light Blue: Water Reflector; Grey: Control rods

5.4.2 Time variation graphs

Graphs of power, maximum temperature, maximum normalized vapour concentration, maximum normalized radiolytic gas concentration in the gas phase, mean and outlet pipe temperatures, mean heat transfer coefficient with the pipes, control rod tip position, maximum pressure, maximum velocities and time step size *versus* time are shown in Figs. 29, 30, 31, 32, 33, 34, 35, 36, 37, 38 up to 28 seconds into the MIPS reactor simulation.

As the simulation starts the control rod adjustment algorithm gradually withdraws the control rod in order to try to produce a power output of 440kW. The power increases exponentially until the solution heats up and large temperatures result (in access of the saturation vapour temperature, see figure 30) and radiolytic gases and vapour are deposited preferentially in the high power central region of the solution. The central region is where these negative reactivity effects are most effective at reducing the reactivity of the system due to increased neutron leakage. The control rods are gradually inserted as a result of the initial power spike, see power versus time in Fig. 29. This control rode movement along with the other negative reactivity effects rapidly reduces the reactivity of the system which then results in the control rodes being gradually withdrawn once again, see Fig. 35. The control rod is eventually pulled completely out of the solution as it tries to maintain the power level at 440kW which it does between 5 and 20 seconds into the simulation. However, after this time the control rod is not effective at controlling reactivity (due to it being out of the solution) and thus it cannot maintain the 440kW power output and thus the power starts to decrease at about t=23 s. The largest maximum temperature occurs just after the fission spike, see power 29 and maximum liquid temperature 30 graphs.

In the maximum normalized vapour concentration versus time graph there is a sharp transition to a more vigorous boiling regime at about 19 seconds into the simulation, see Fig. 31. The radiolytic gas bubbles are being continuously deposited into the solution and tend to accumulate over this time period resulting in the general increase in radiolytic gas bubble concentration as seen in figure 32. During the more vigorous boiling regime there is an increase in the water temperature in the cooling coils (see, Fig.33) resulting in greater power being extracted out of the system from the cooling water. This is confirmed by the increase in liquid-cooling coils heat transfer coefficient in Fig. 34. It should be noted that the heat transfer coefficient for the 220kW simulation was approximately $0.89 \text{ W cm}^{-2} \text{ K}^{-1}$ compared to $1.3 \text{ W cm}^{-2} \text{ K}^{-1}$ for this 440kW simulation. At the 19 s transition point there is also a sharp increase in the solution and gas velocity which helps increase the heat transfer coefficient, see Fig. 37. The heat transfer increase with increased liquid velocity. The time step size also responds by decreasing its size during the vigorous boiling, see Fig. 38.

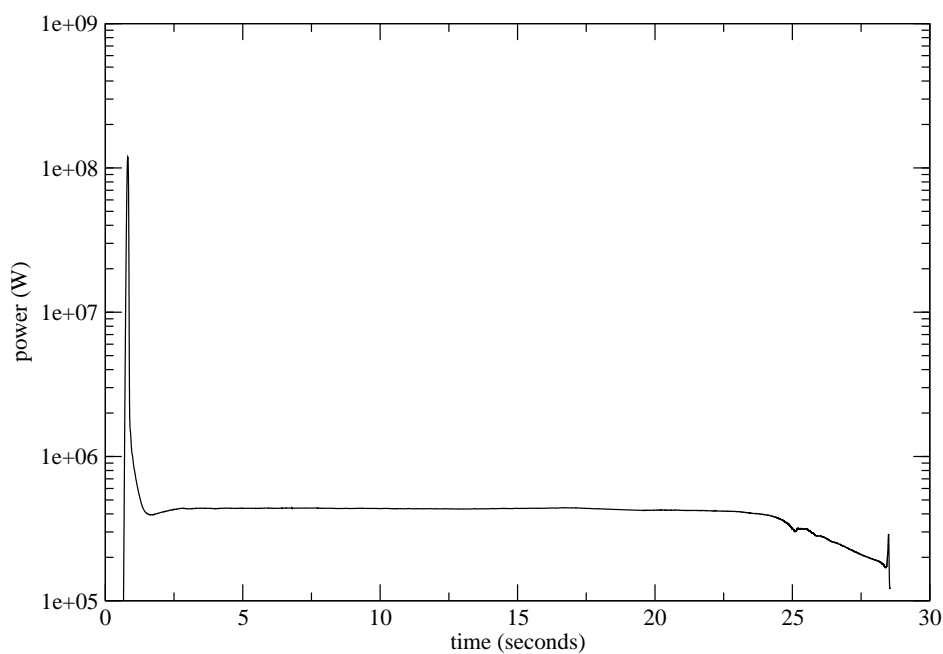


Figure 29: Power versus time for the MIPS reactor.

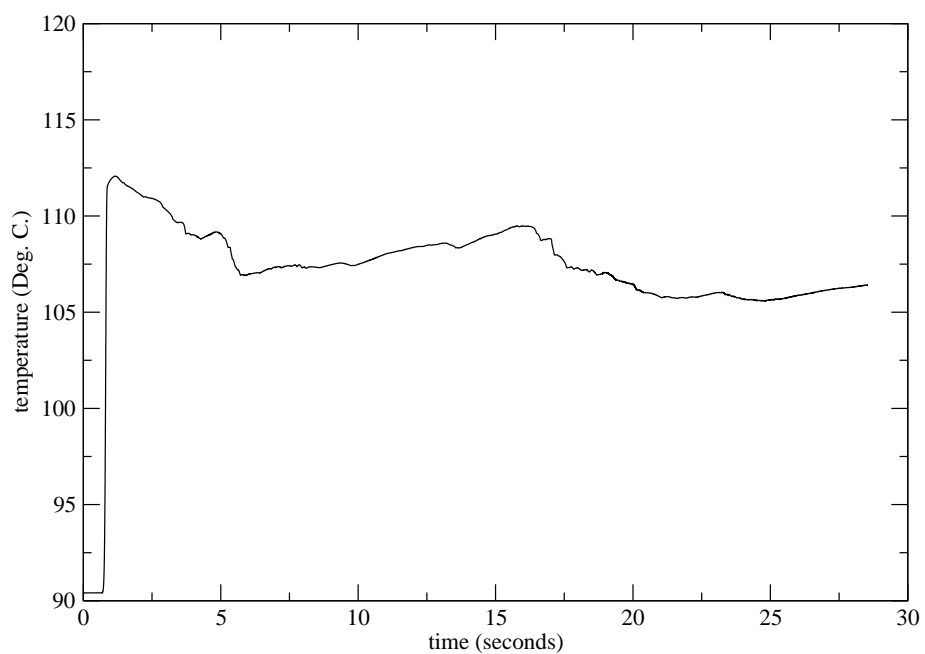


Figure 30: Maximum liquid temperature versus time for the MIPS reactor.

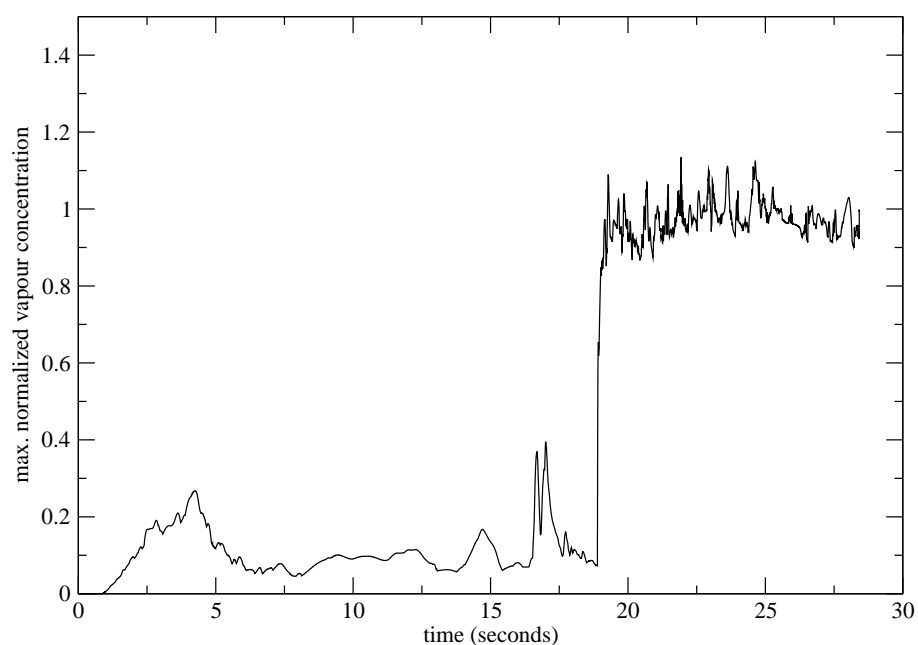


Figure 31: Maximum normalized vapour concentration versus time for the MIPS reactor.

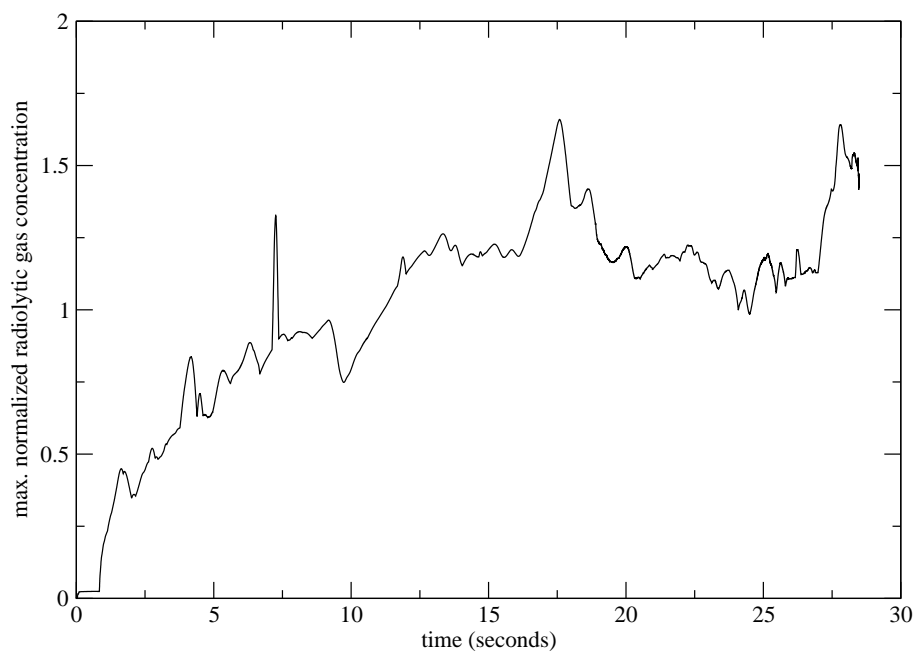


Figure 32: Maximum normalized radiolytic gas concentration in the gas phase versus time for the MIPS reactor.

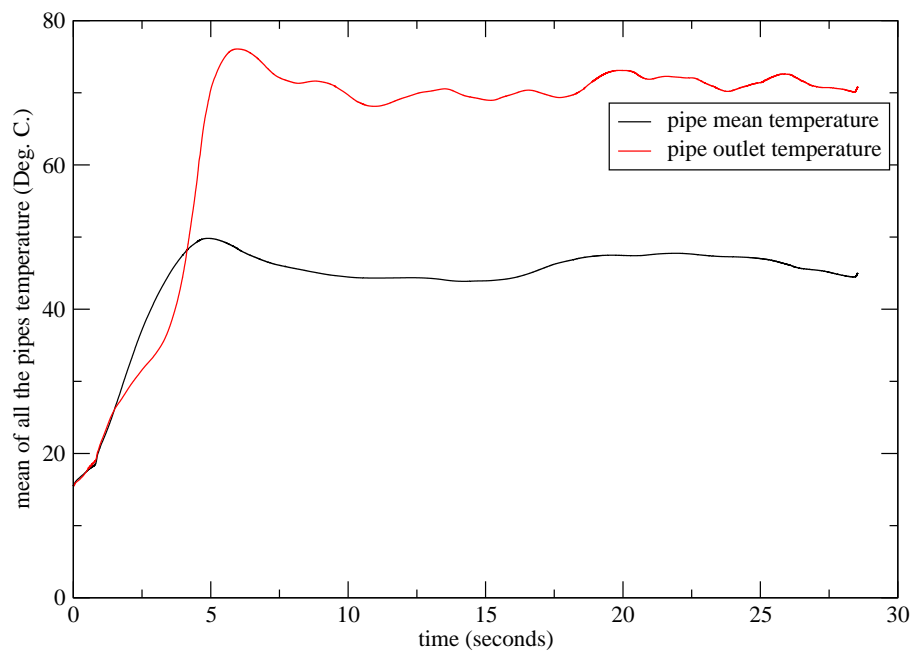


Figure 33: Water pipe outlet temperature and water mean temperature versus time for the MIPS reactor.

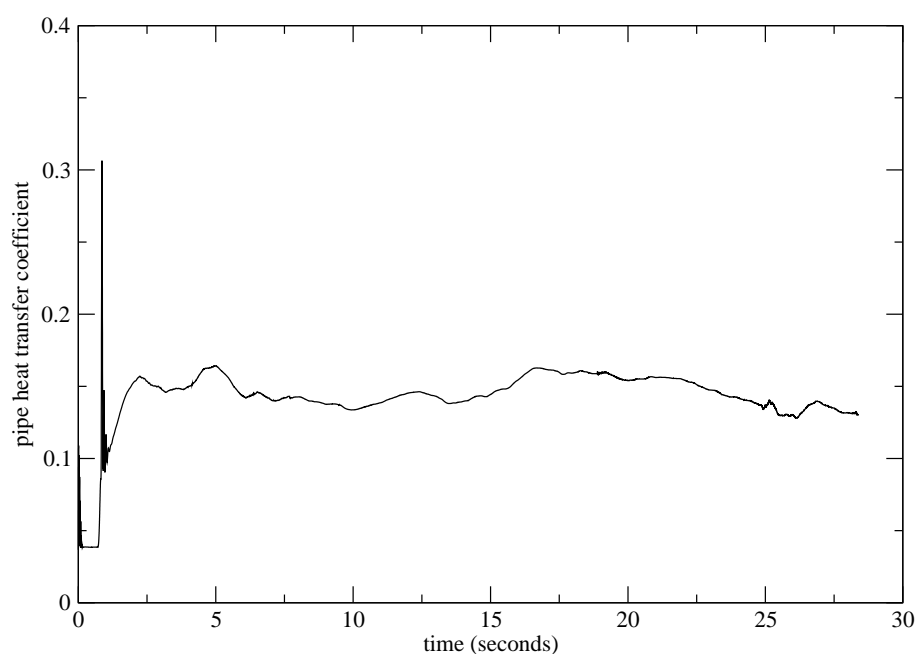


Figure 34: Mean heat transfer coefficient with the pipe versus time for the MIPS reactor.

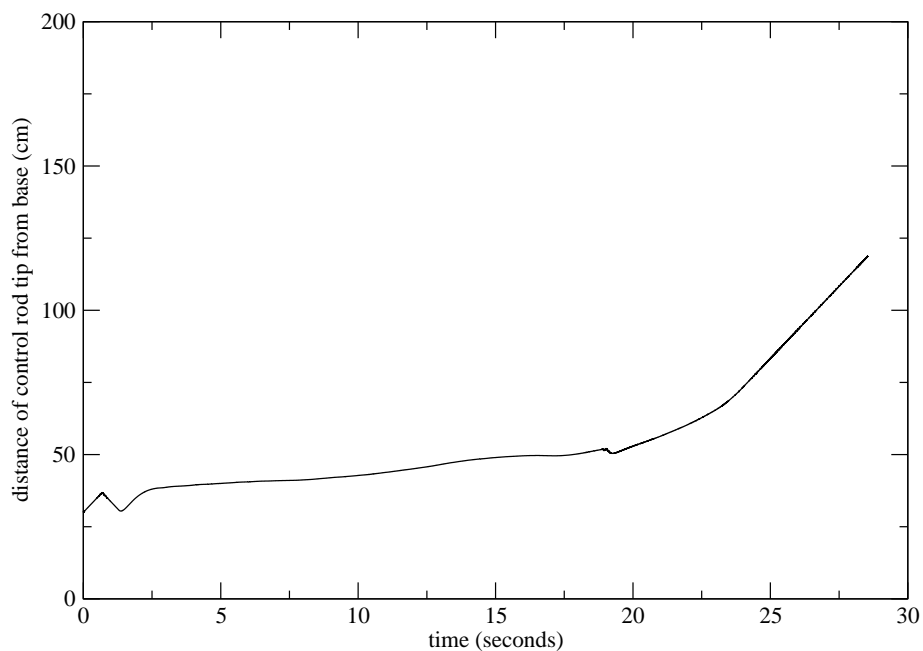


Figure 35: Control rod tip position (distance of tip from the base of the fluid filled cavity of MIPS) versus time. The control rod comes in from the top of the reactor.

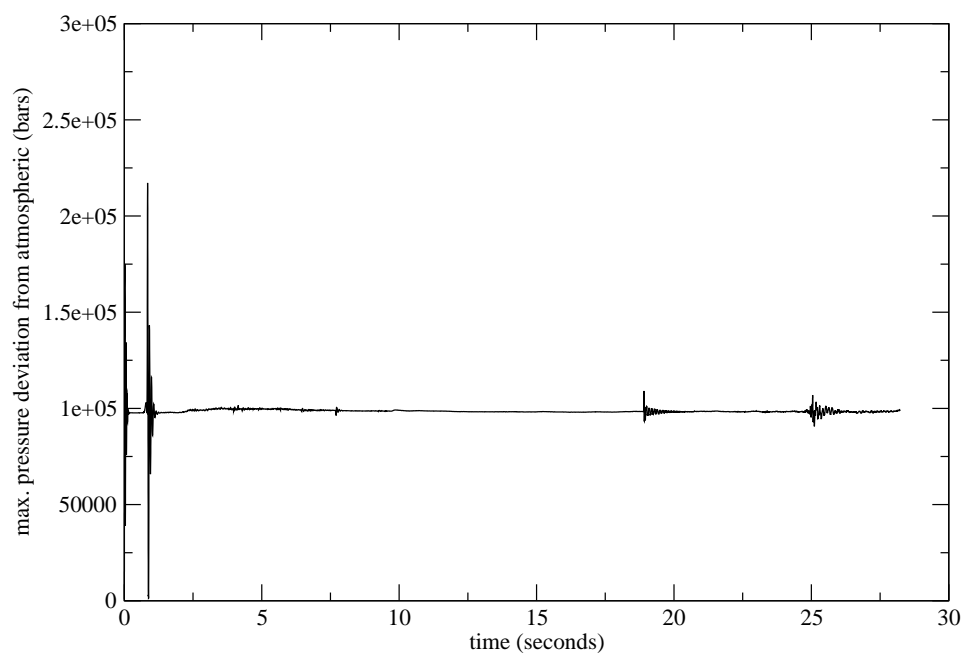


Figure 36: Maximum pressure versus time for the MIPS reactor.

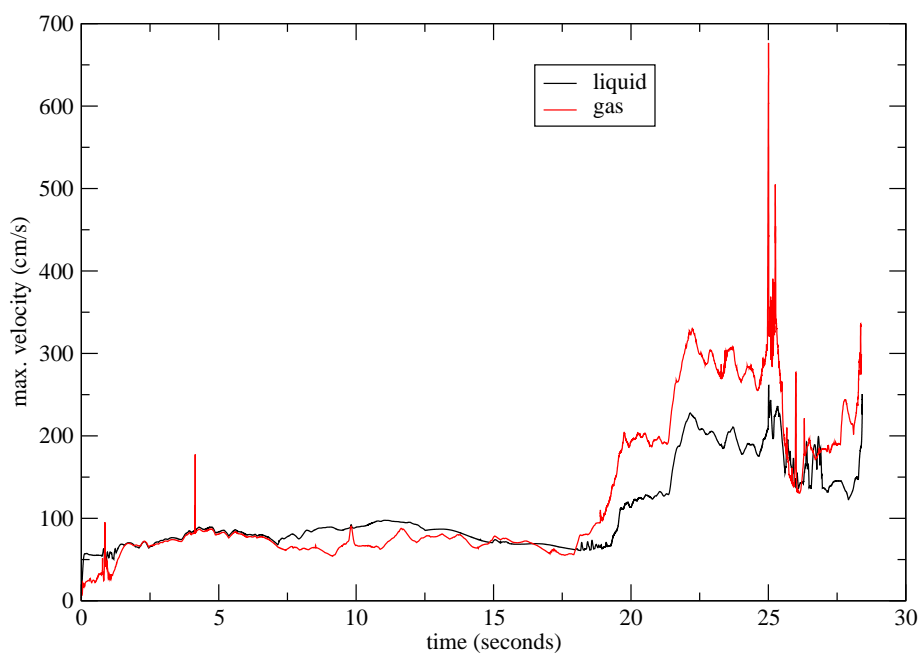


Figure 37: Maximum liquid and gas velocity versus time for the MIPS reactor.

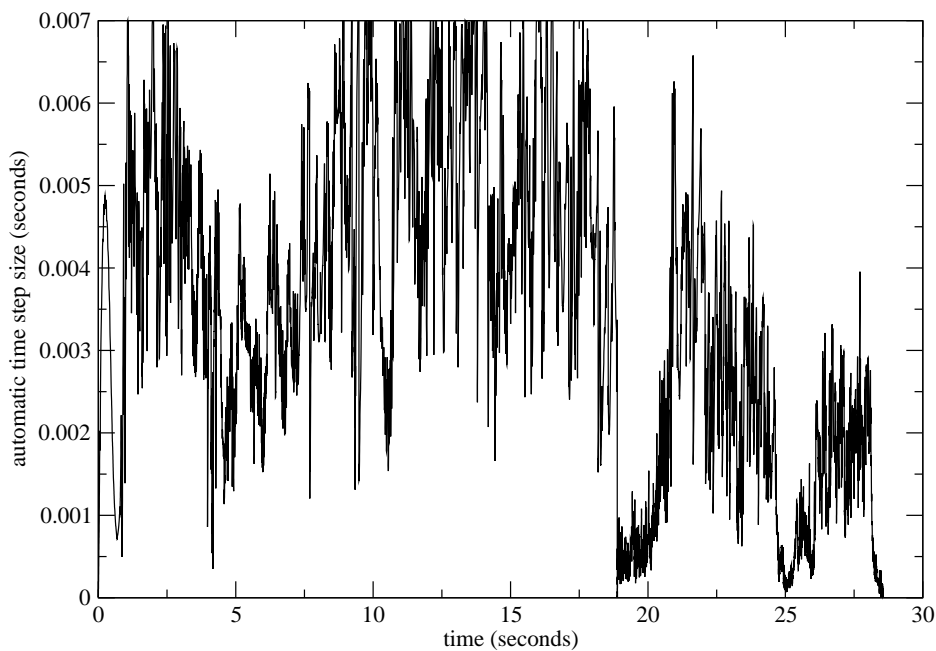


Figure 38: Automatic time step size versus time for the MIPS reactor.

5.4.3 Snapshots of pipe water temperature for the MIPS reactor

The water temperature in the cooling coils versus distance along the cooling coils are shown in figures 39, 40, 41, 42, at 4 instances in time $t=15, 20, 25, 28$ s respectively into the simulation. The pipe numbers are ordered from closest to the central axis outward. It is interesting to contrast the $t=150$ s pipes temperature with the other plots, as it is only this plot that shows the temperature distribution before there is a sudden change in the magnitude of vapour production at about $t=19$ s, see the maximum normalized vapour concentration graph 31 and the graph of the cooling coil outlet temperature 33, which both show a marked increase at this time. At $t=15$ s there is a slightly decrease temperature compared to the other time levels shown and a narrower spread of temperatures of the cooling coils. Moreover, on more vigorous boiling (starting at about 19 seconds) the water temperatures increase on average and the range of temperatures also increases due to inhomogeneities in the mixing (caused by boiling) in the solution.

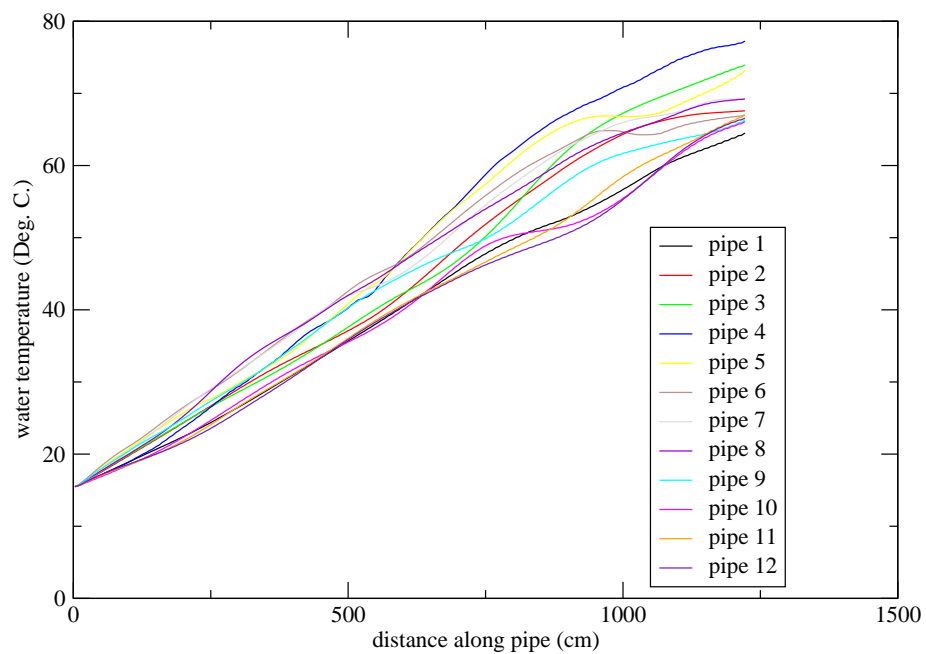


Figure 39: Water temperature in each of the 12 cooling coil pipes versus distance along each pipe for the MIPS reactor at $t=150$ seconds.

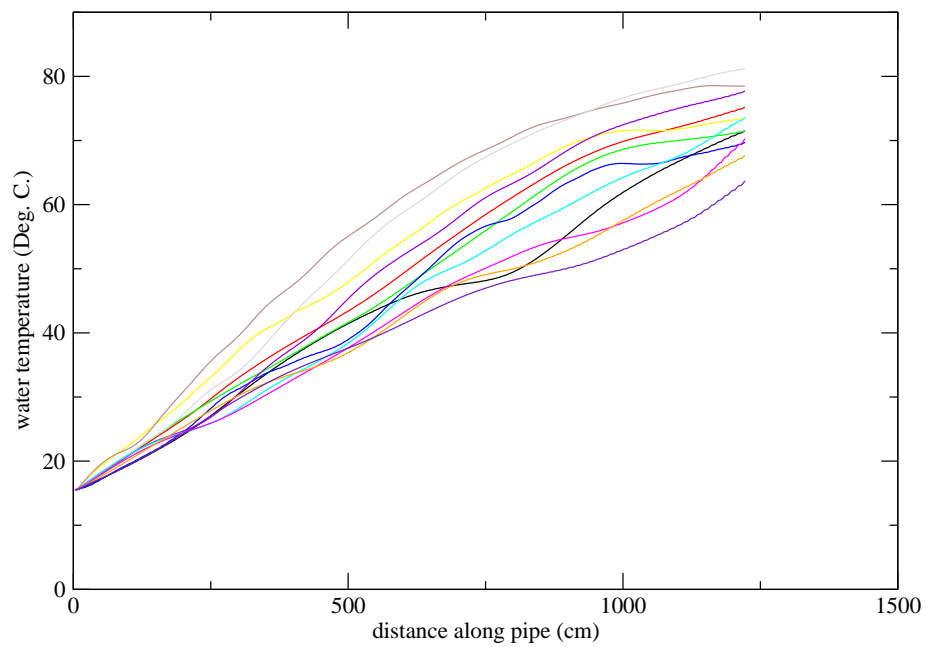


Figure 40: Water temperature in each of the 12 cooling coil pipes versus distance along each pipe for the MIPS reactor at $t=200$ seconds.

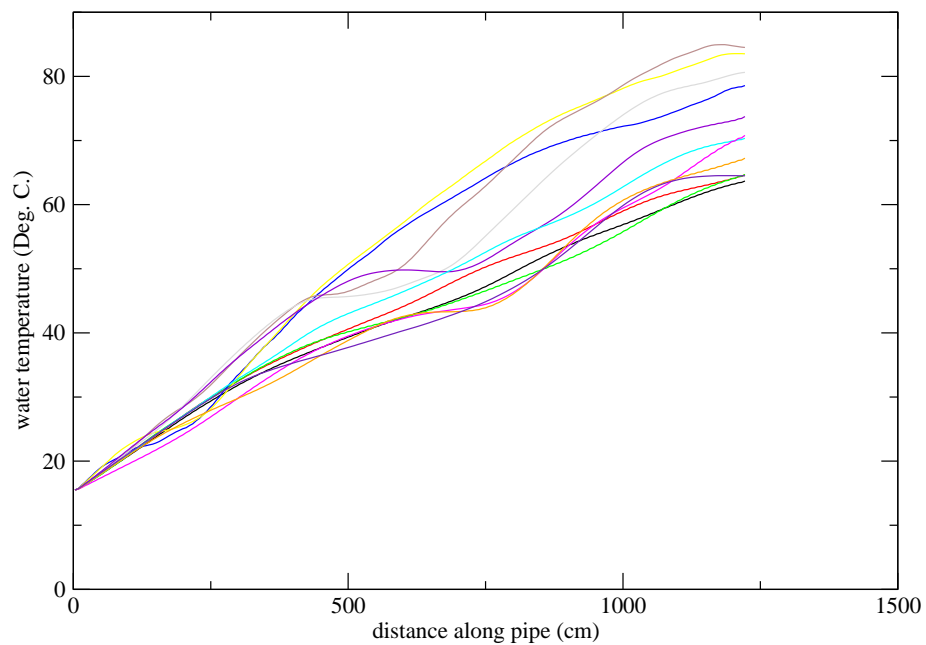


Figure 41: Water temperature in each of the 12 cooling coil pipes versus distance along each pipe for the MIPS reactor at $t=250$ seconds.

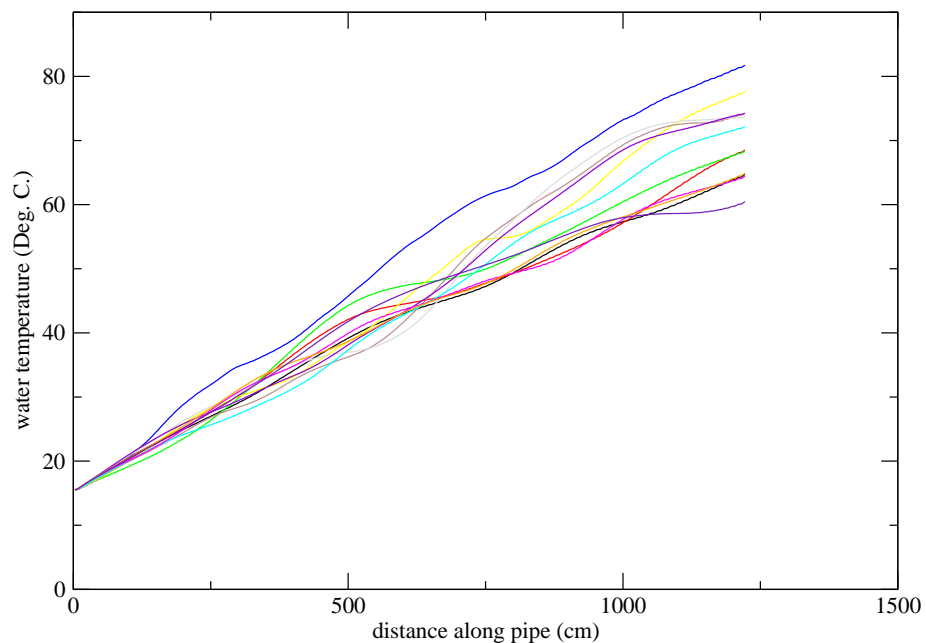


Figure 42: Water temperature in each of the 12 cooling coil pipes versus distance along each pipe for the MIPS reactor at $t=280$ seconds.

5.4.4 Snapshots of spatial distributions of the MIPS reactor

A number of fields at various instances in time are shown in the figures. The volume fraction fields around the time of two rapid boiling events are shown in figures 43, for the first, and figures 44, for the second boiling event. This boiling tends to occur near the surface of the fissile liquid. The volume fraction at instances in time between these boiling events can be seen in figures 44a,b. The boiling rapidly moves the liquid upwards as the vapour bubbles approach the free surface and burst. The temperatures at these same instances in time are shown in figures 45, 46. These show the good mixing within the reactor as the temperatures are fairly uniform, other than near the central axis. Near the central axis is where the drag forces exerted by the densely packed cooling coils reduce mixing. There is also a relatively low power density in this region again due to the presence of the densely packed cooling coils. The maximum temperatures are observed near the bottom of the reactor, possibly because of the increase in the saturation vapour temperature with the larger hydrostatic pressures here. The large temperature hot spots at the bottom of the reactor may also occur because of the reduced presence of radiolytic gas bubbles providing nucleation sites for vapour production. The vapour can be readily seen in the bubbles in the plots of the normalized vapour concentration in figures 47, 48. The rapid boiling near the surface can be clearly seen in these figures but notice also that some boiling occurs deeper down within the solution. As with radiolytic gas bubbles (see figures 49, 50) the vapour bubbles tend to accumulate below the cooling coils as the vapour bubbles rise. Large masses of water vapour tend to grow from these regions just below the cooling coils. The radiolytic gas concentration is more uniform throughout the reactor than the vapour at all time levels.

The rapid mixing within the reactor is shown in the liquid velocity vectors at various instances in time in figures 51, 52. Notice also that the mixing is suppressed (due to drag forces) near the central axis, where there are densely packed cooling coils, although the liquid can move more freely up and down in these regions than across - partly due to imposition of axi-symmetry onto the solution fields. The power distribution which is also the distribution of the shortest delayed group (group 6) has a dip near the central axis, see 53f. Snapshots of the six delayed neutron precursor concentration groups at t=27.9 s for the MIPS reactor with boiling are shown in 53. The other delayed groups show the mixing of the reactor on the time scales associated with these delayed groups.

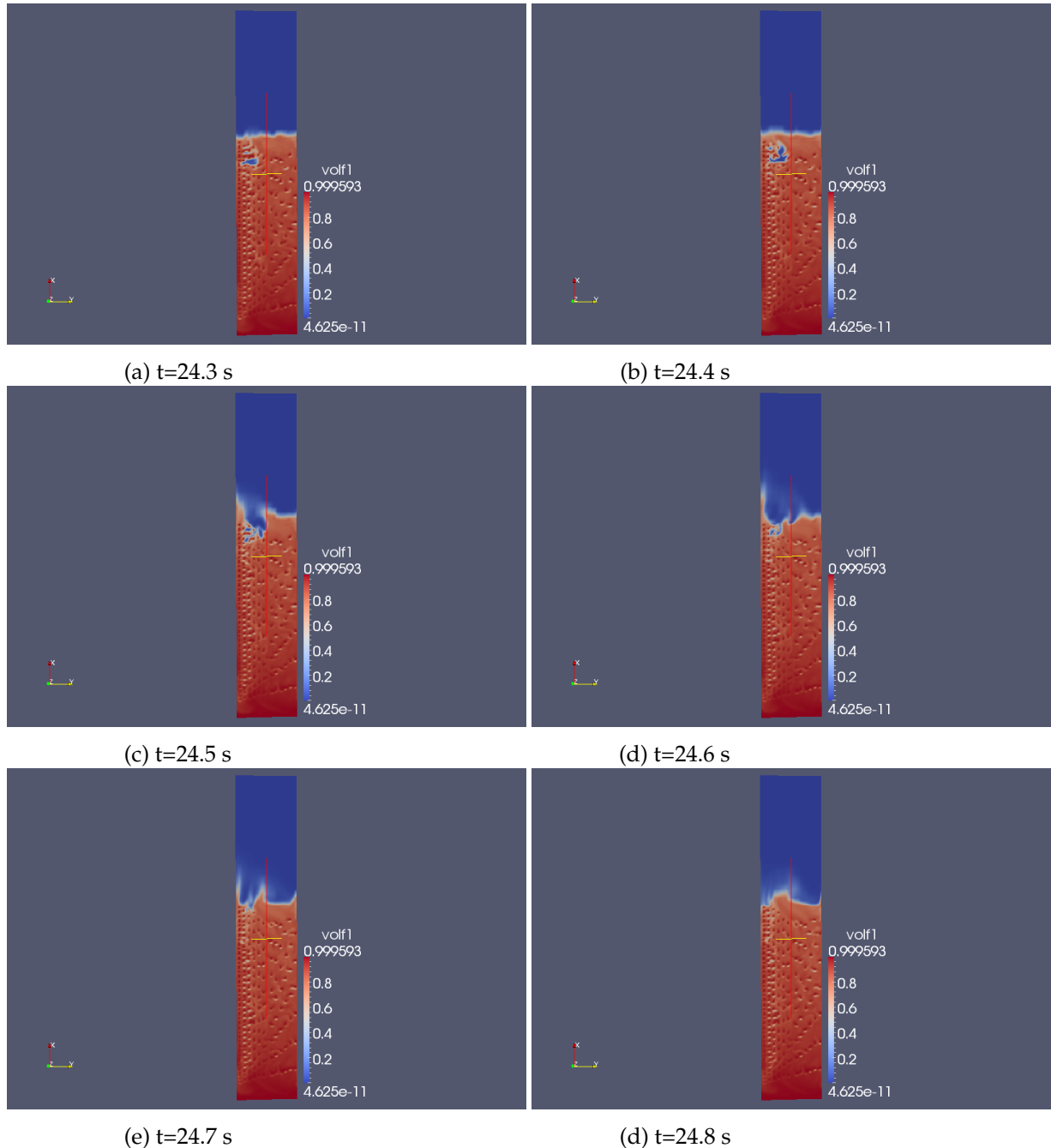


Figure 43: Snapshots of liquid volume fraction at various instances in time for the MIPS reactor with boiling.

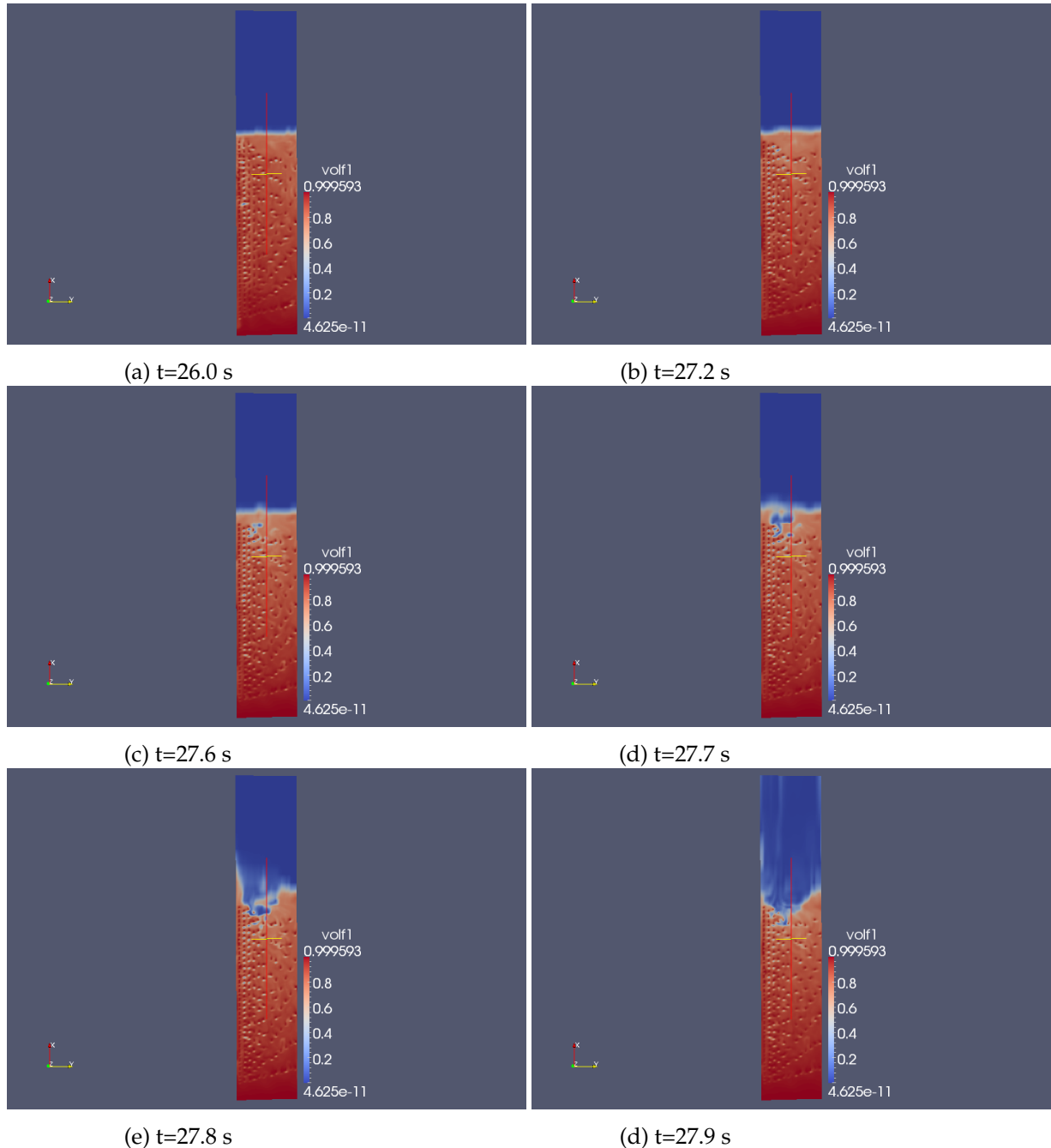


Figure 44: Snapshots of liquid volume fraction at various instances in time for the MIPS reactor with boiling.

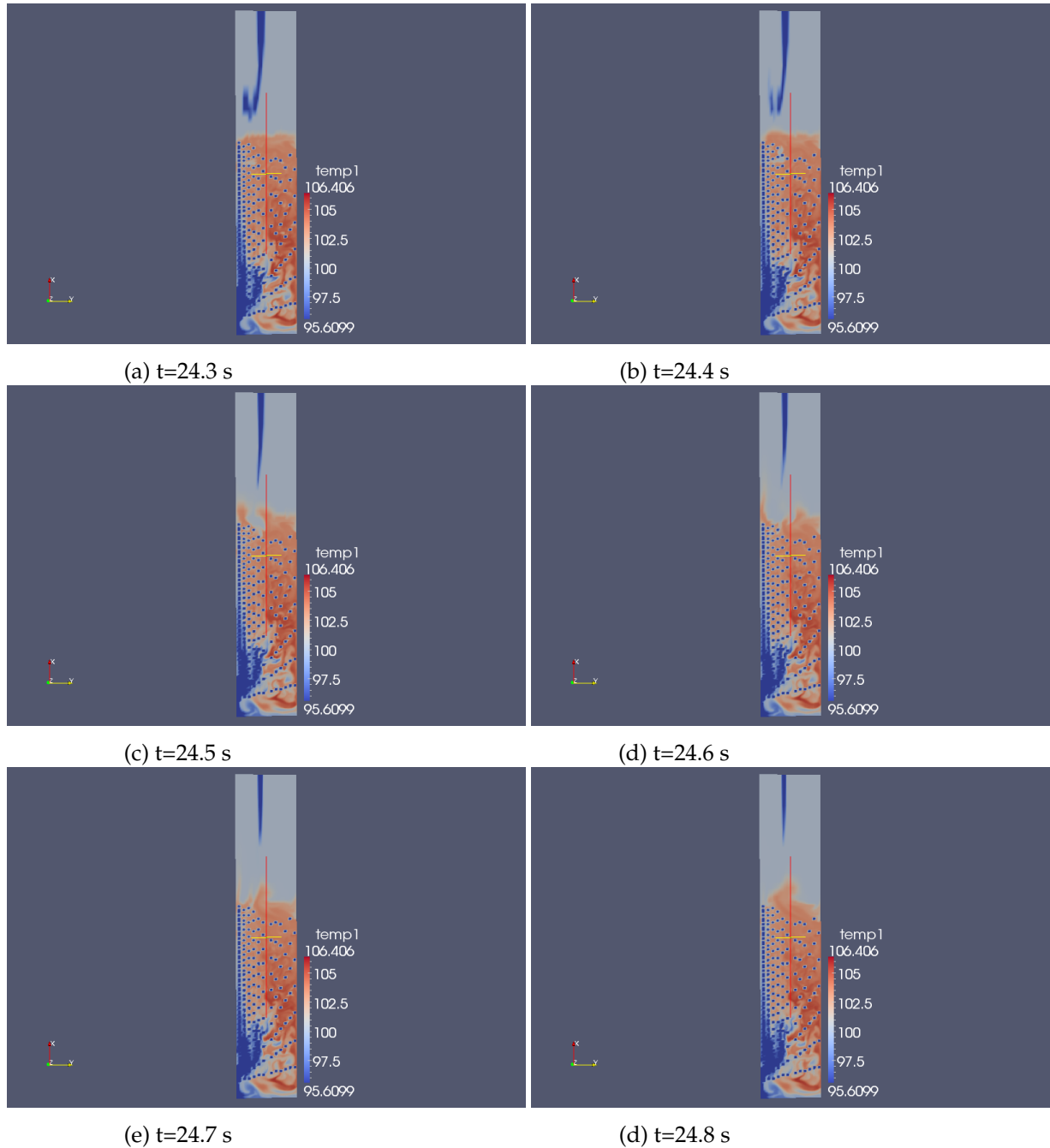


Figure 45: Snapshots of liquid temperature (close to the gas temperature) at various instances in time for the MIPS reactor with boiling. The temperature of the legend has been limited to between 95 Deg and the maximum temperature over the last 20 seconds of the simulation.

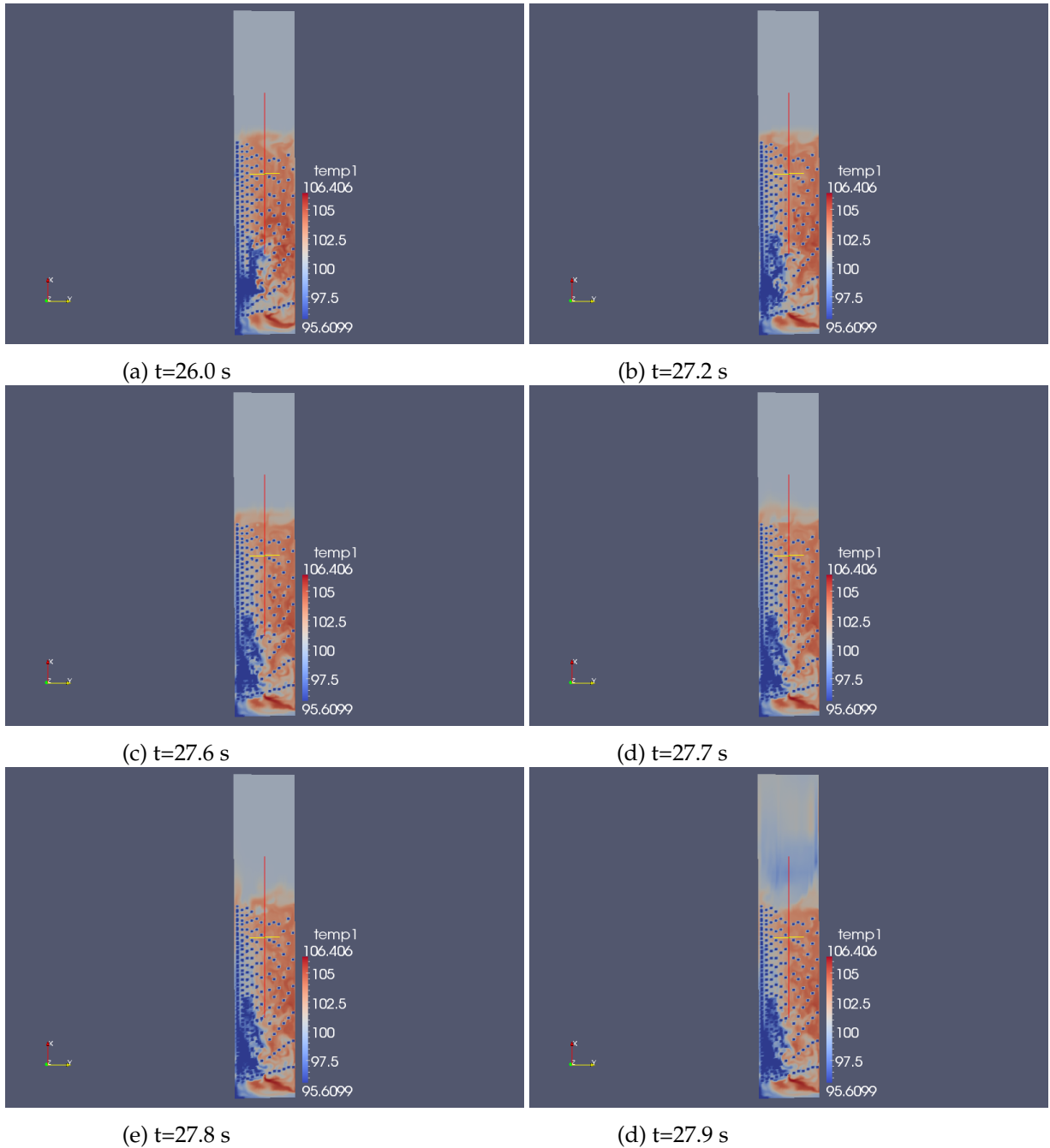


Figure 46: Snapshots of liquid temperature (close to the gas temperature) at various instances in time for the MIPS reactor with boiling. The temperature of the legend has been limited to between 95 Deg and the maximum temperature over the last 20 seconds of the simulation.

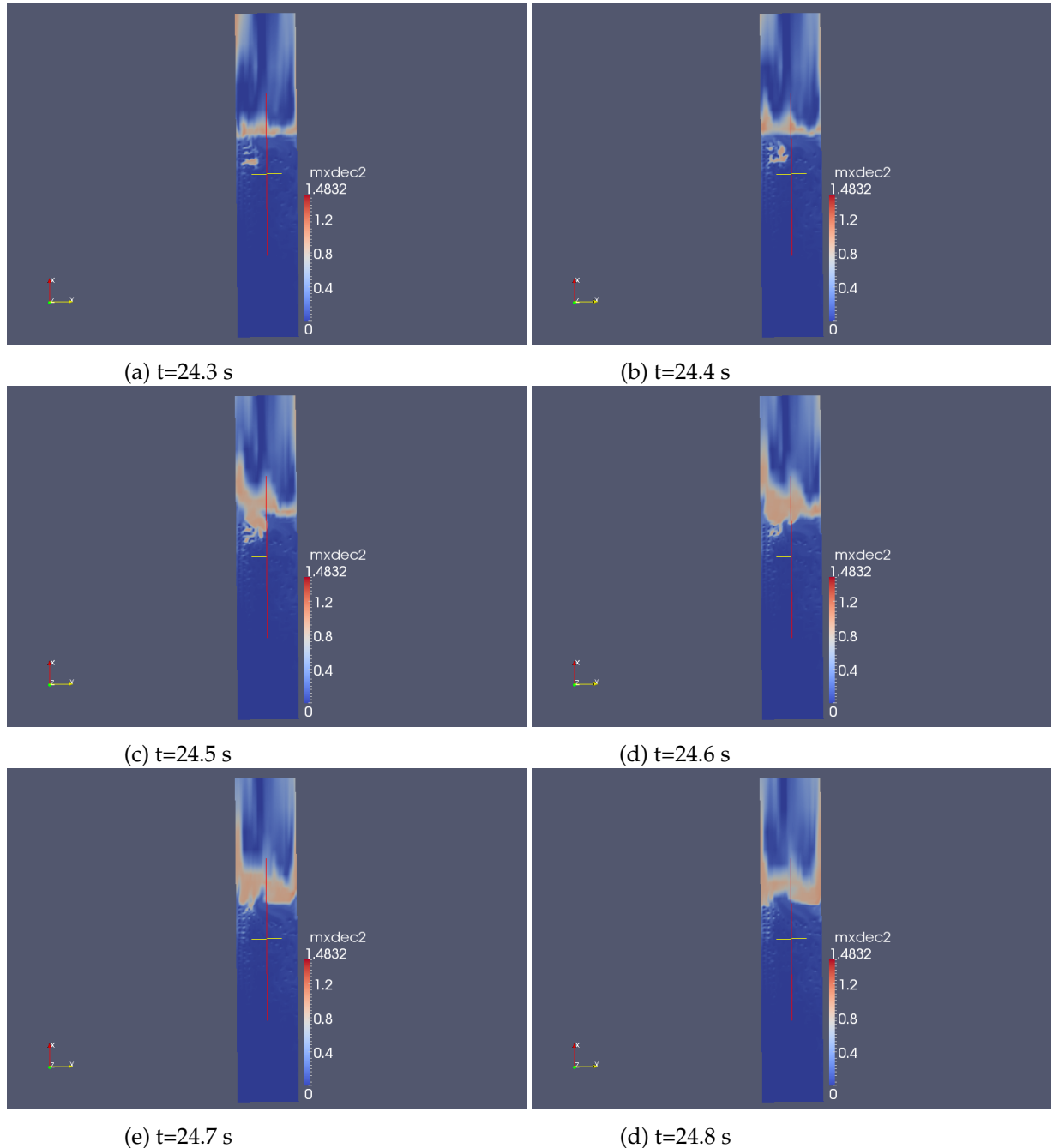


Figure 47: Snapshots of maximum normalized concentration of vapour (akin to vapour volume fraction) at various instances in time for the MIPS reactor with boiling.

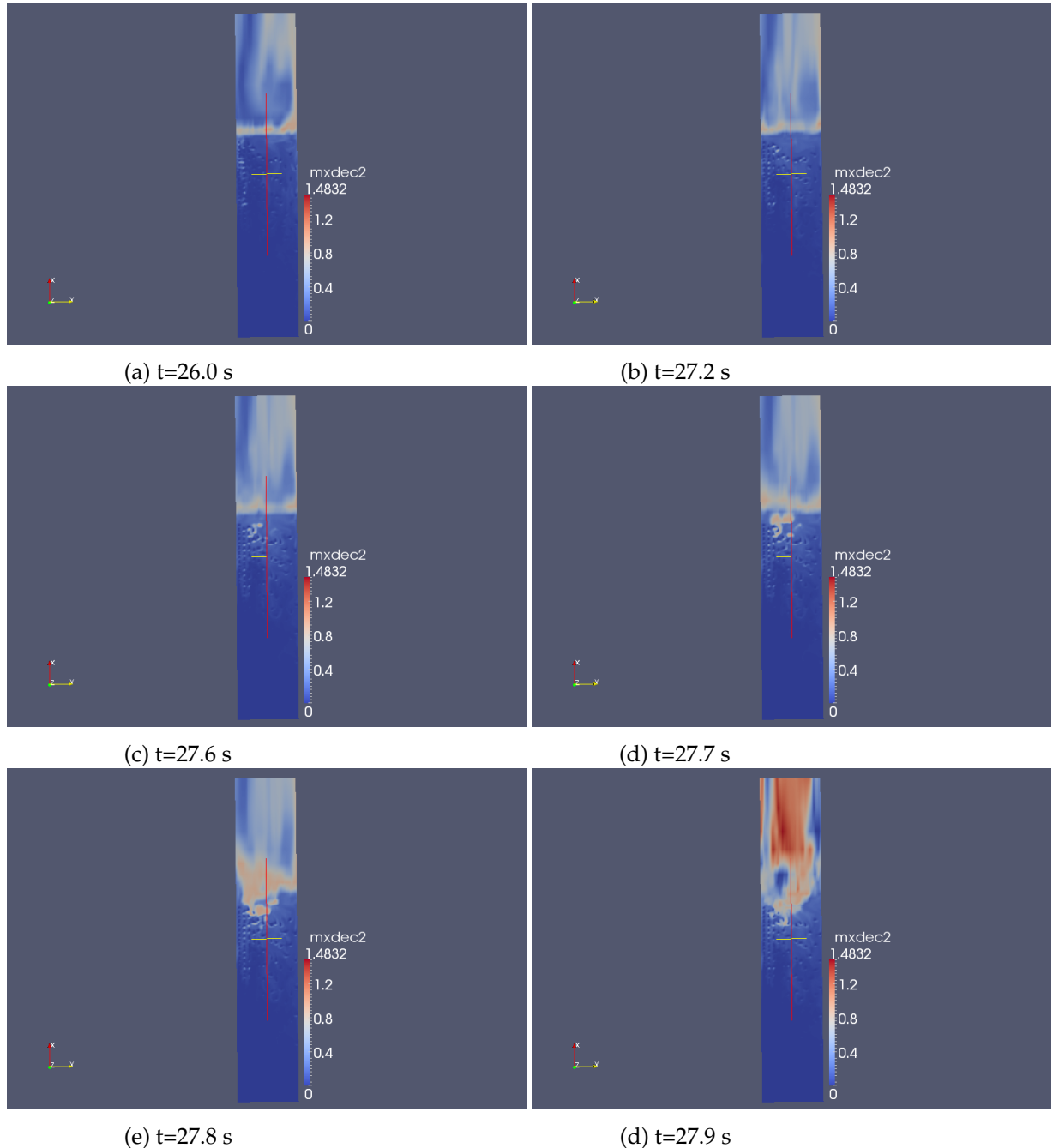


Figure 48: Snapshots of maximum normalized concentration of vapour (akin to vapour volume fraction) at various instances in time for the MIPS reactor with boiling.

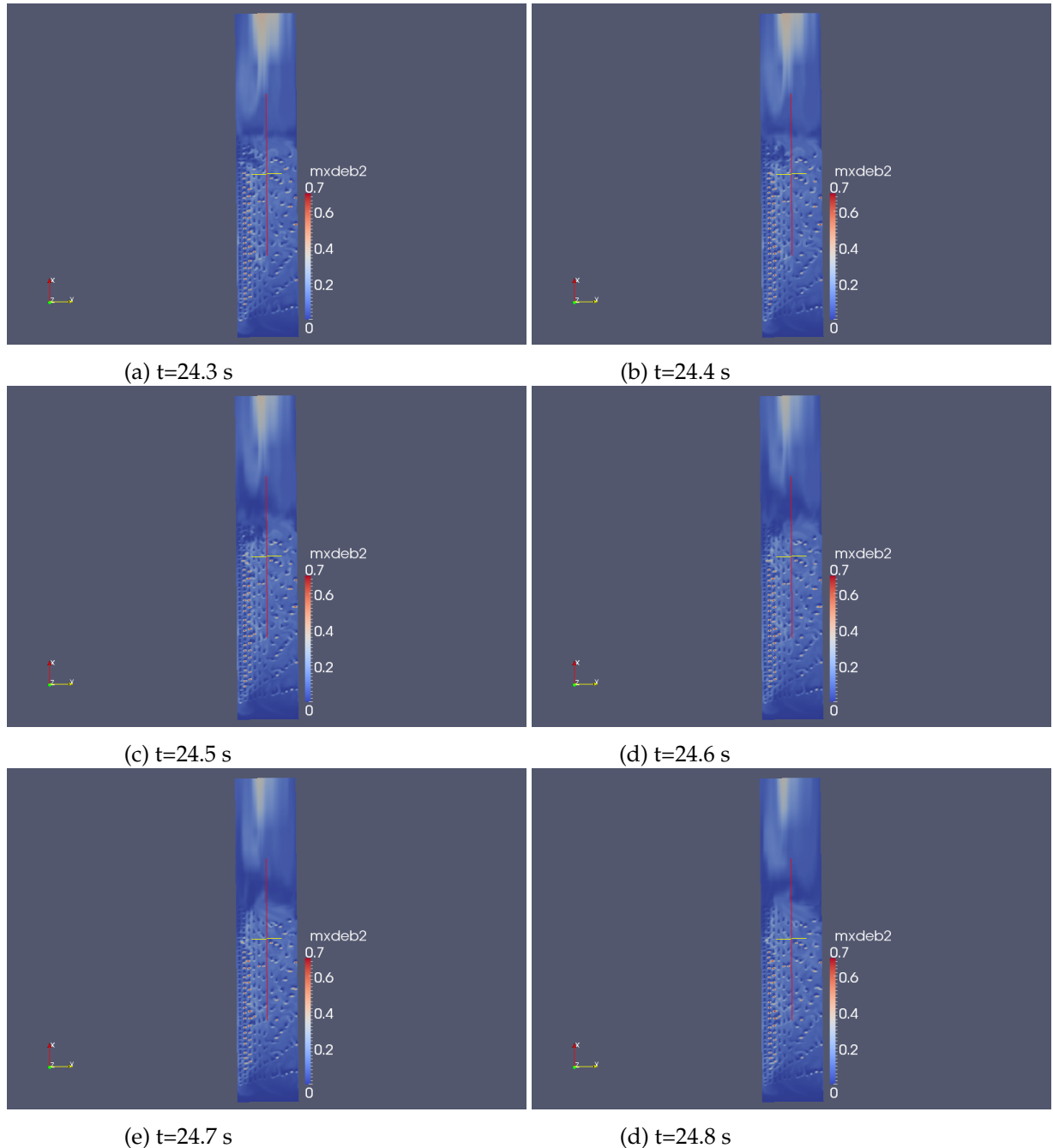


Figure 49: Snapshots of maximum normalized radiolytic gas concentration (akin to radiolytic gas volume fraction) in the gas phase at various instances in time for the MIPS reactor with boiling.

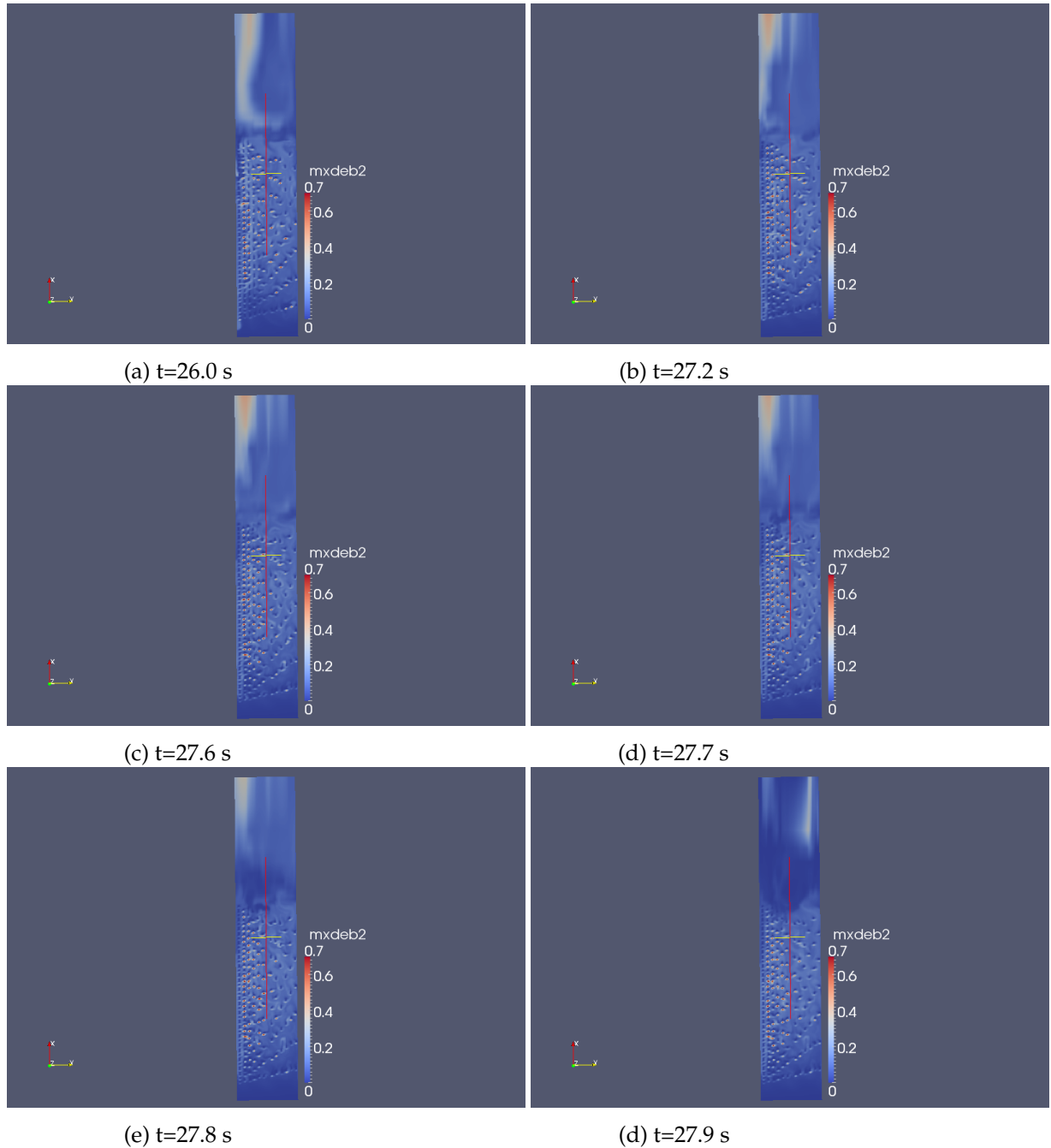


Figure 50: Snapshots of maximum normalized radiolytic gas concentration (akin to radiolytic gas volume fraction) in the gas phase at various instances in time for the MIPS reactor with boiling.

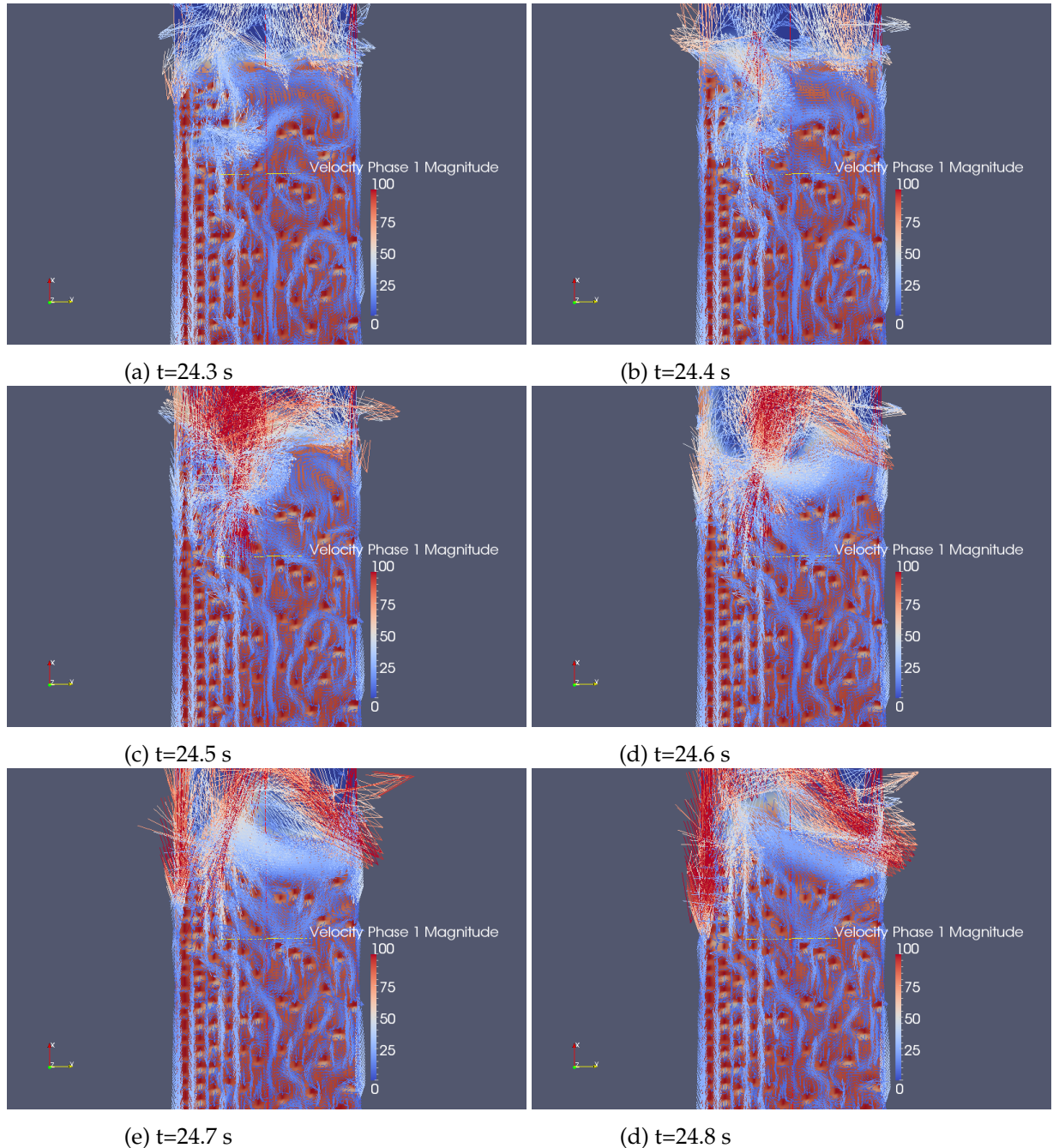


Figure 51: Snapshots of liquid velocity as well as liquid volume fraction at various instances in time for the MIPS reactor with boiling.

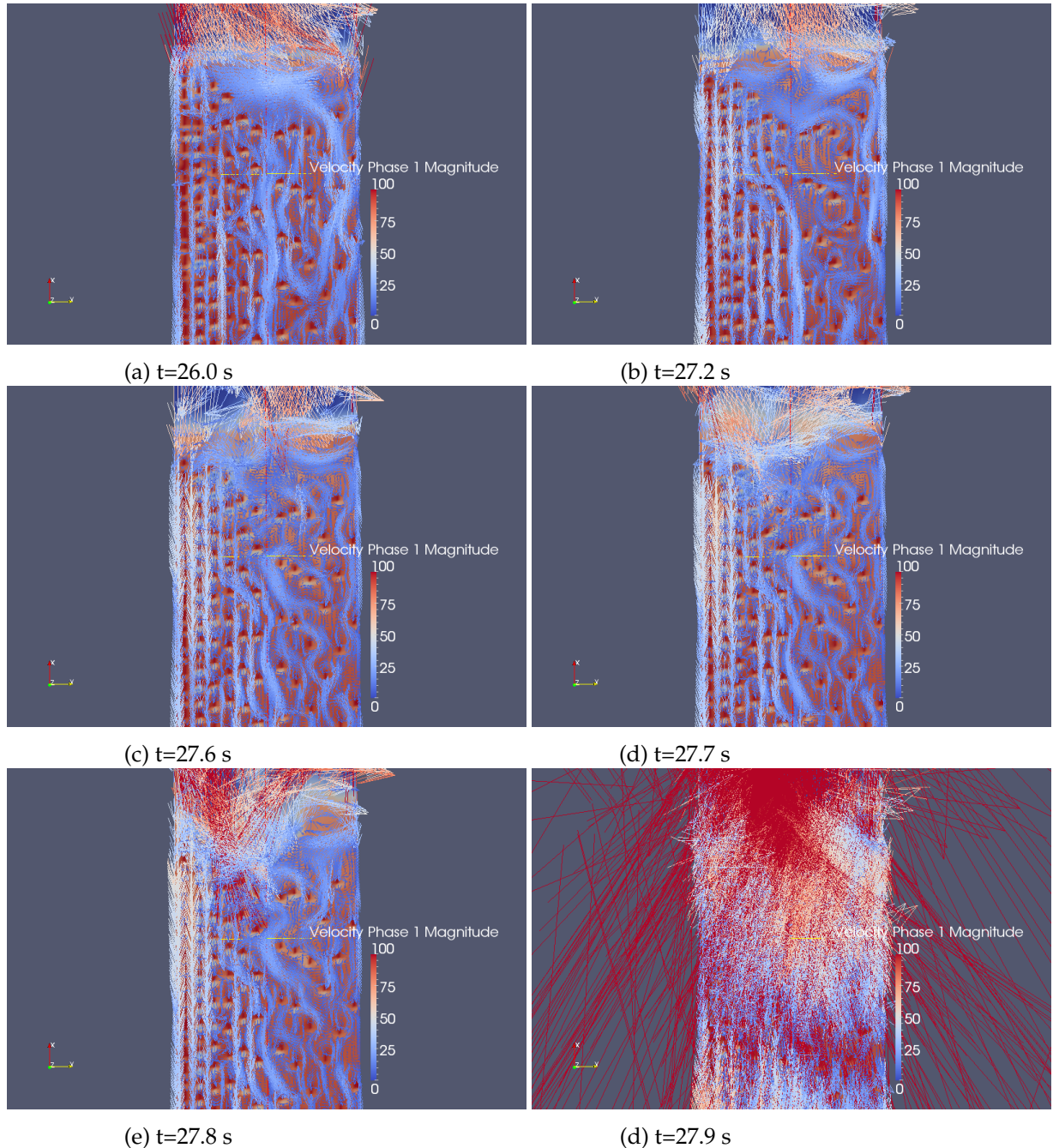


Figure 52: Snapshots of liquid velocity as well as liquid volume fraction at various instances in time for the MIPS reactor with boiling.

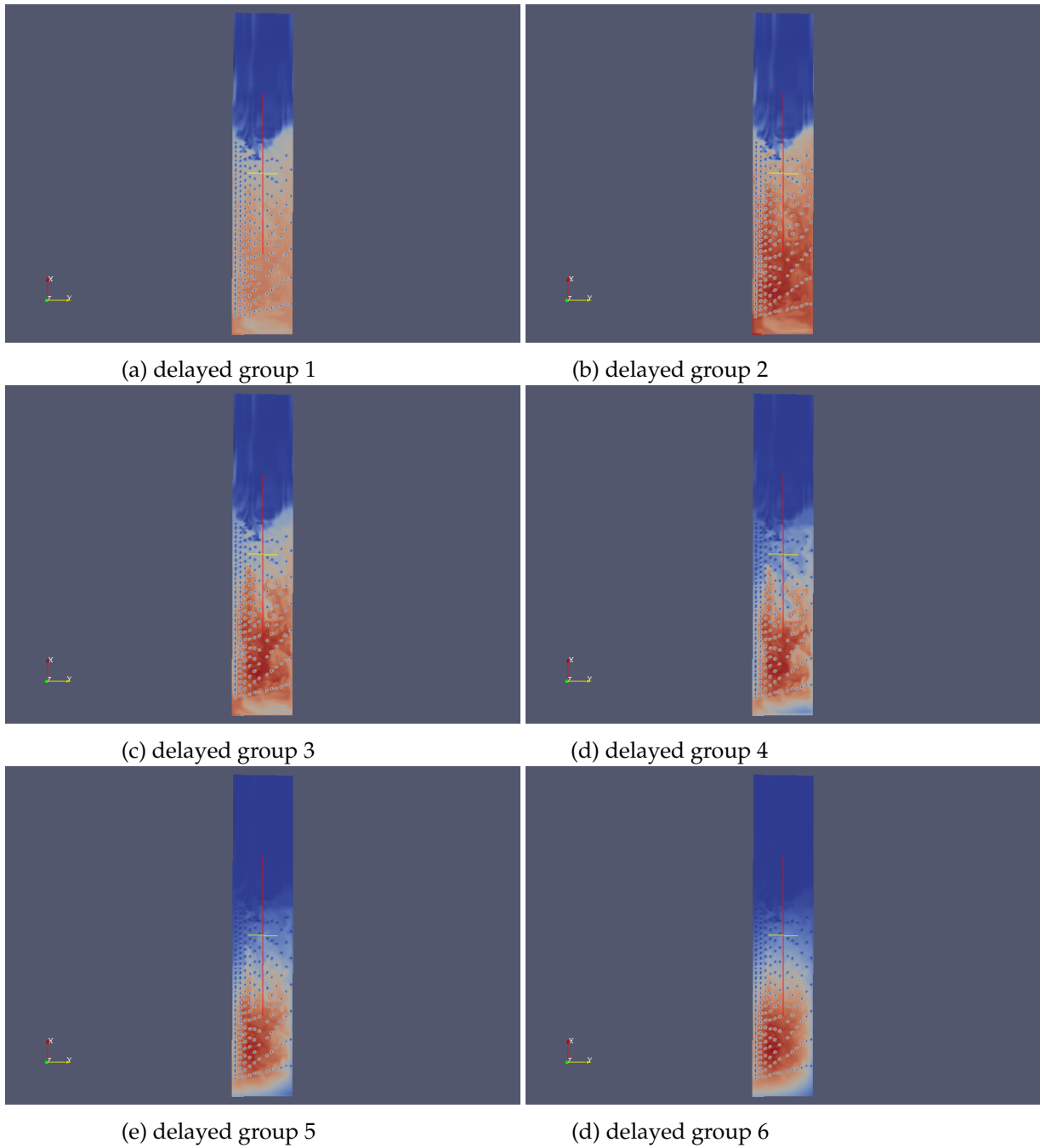


Figure 53: Snapshots of delayed neutron precursor concentration at $t=27.9$ s for the MIPS reactor with boiling. Delayed group 1 has a half life of 55 seconds and delayed group 6 has a half life of 0.2 seconds. The shortest lived delayed group 6 shows the power distribution in the reactor.

5.5 FETCH-MIPS applied to a postulated accident

FETCH-MIPS is applied, in this section, to model a rod ejection accident. The initial fissile liquid level is further increased by 5 cm from that of the previous section. The corresponding simulation is performed as described also in the previous section, aiming for a 440kW power output, and in which the reactor simulation is assumed to reach a 'steady state' at 19 seconds into the transient. At this point the control rod(s) is/are ejected producing an estimated 3\$ step reactivity insertion. There is then a rapid deposition of energy followed by rapid boiling of the solution, as seen in the liquid volume fraction distributions at various instances in time, Figs 54, 55. One can see that some of the solution is thrown into the upper regions of the reactor.

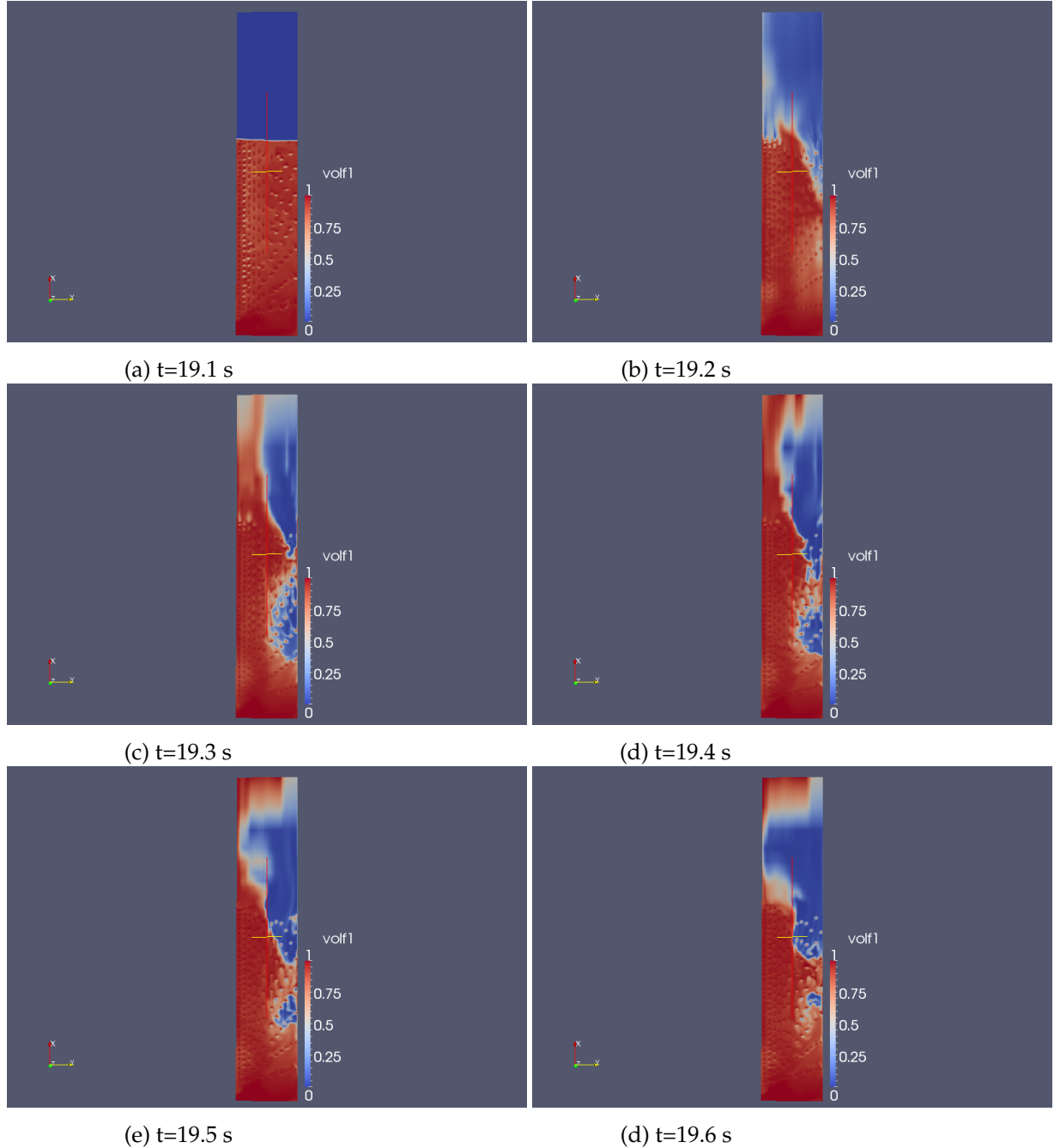


Figure 54: Snapshots of liquid volume fraction at various instances in time for the MIPS reactor and with boiling with a large reactivity insertion applied during 'steady' conditions.

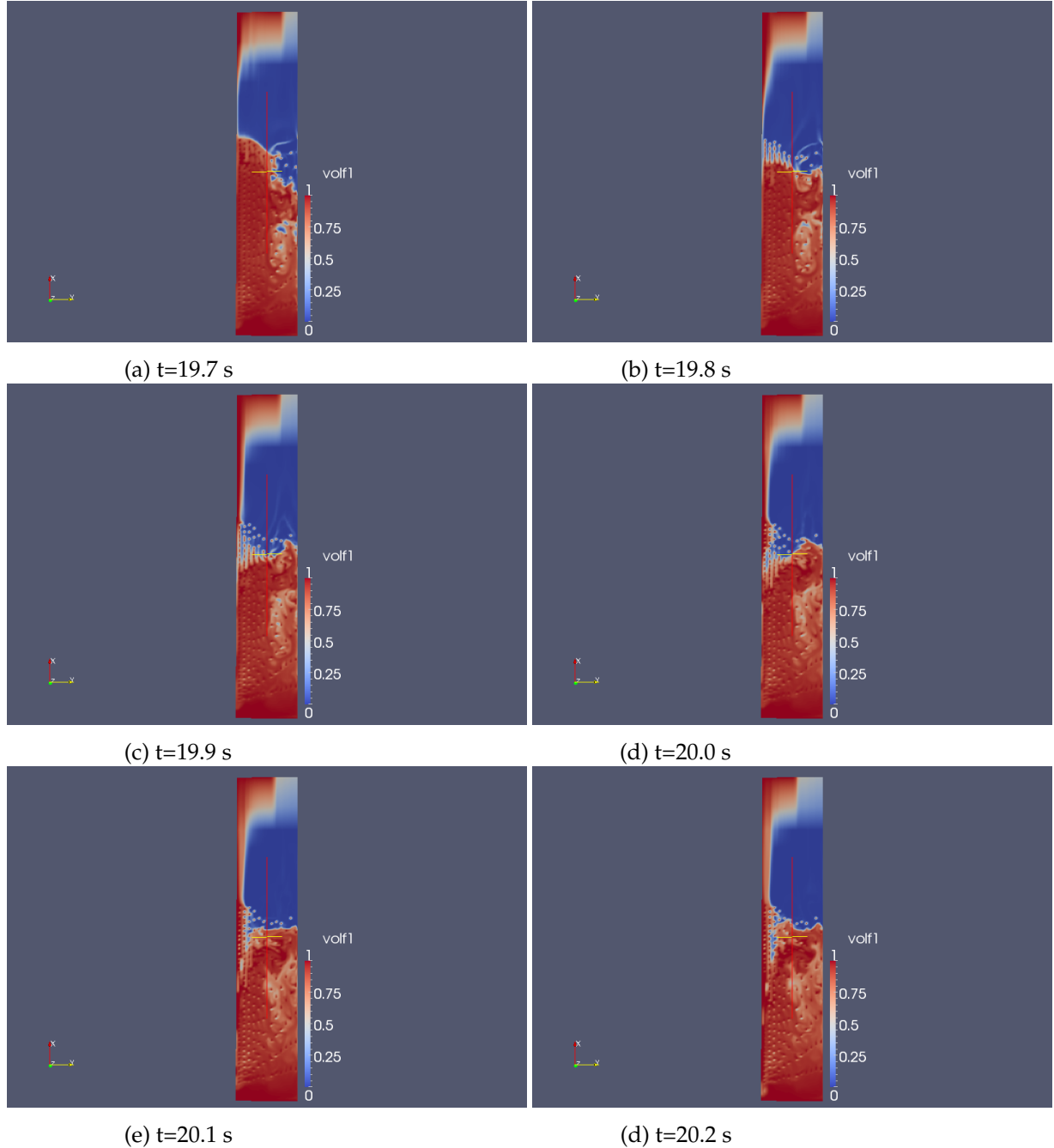


Figure 55: Snapshots of liquid volume fraction at various instances in time for the MIPS reactor and with boiling with a large reactivity insertion applied during 'steady' conditions.

6 Conclusions

The boiling model developed here has been tested against a volumetric boiling experiment to provide some confidence in its predictive ability. The rest of the model has been tested and validated elsewhere in numerous papers and conference reports and compares well against available experimental data e.g. from SILENE, TRACY, CRAC solution criticality experiments. The detailed FETCH-MIPS results have modelled and revealed some of the physical characteristic of the MIPS reactor under solution boiling conditions. These include:

- (a) There is high heat transfer rates to the cooling coils observed under boiling conditions which helps to produce a 440kW power output in the simulation.
- (b) The radiolytic gas presence tends to suppress the heat transfer on the vapour side of the liquid/-vapour interface and therefore (according to the Stefan condition which is a statement of energy conservation across the interface) suppresses the mass transfer rate too or from vapour bubbles.
- (c) There is evidence of intermittent boiling in which a few seconds of little boiling is proceeded by a rapid boiling event.
- (d) Very substantial superheating was observed in the MIPS simulations, but not in the CRAC geometry criticality experiments, which needs further investigation as this has significant accident and reactor stability implications.
- (e) The simulation results of the postulated accident problem solved with FETCH-MIPS suggests that it may be suitable for accident modelling, as well as modelling 'steady' and 'normal' transient conditions.
- (f) Future work needs to look carefully at the stability of the reactor under boiling conditions.
- (g) The very detailed modelling provided by FETCH-MIP provides confidence in its accuracy, but it does come at a large computational expense with long run times. To make progress with detailed modelling the simulations need to be run on parallel machines rather than in serial.
- (h) The heat transfer coefficient between the fissile solution and the cooling coils is perhaps the key parameter. This is resolved in FETCH-MIPS as much as currently possible but the details of the heat transfer between the cooling coils and solution are still modelled/parameterized and depend on the local conditions. This parameterization should be validated/improved with detailed numerical simulation, provided by Direct Numerical Simulation DNS and Large Eddy Simulation LES methods, including the presence of both radiolytic and vapour gases. However, relatively simple improvements to the modelling of the radial distribution of the key variables in the pipes and around them - the water and the steel and the surrounding fissile solution could contribute significantly to the accuracy of the FETCH-MIPS modelling.

- (i) The heat and mass transfer coefficients between the liquid and gas phases may be improved with recently popularized bubble size distribution models, see Multiple Size Group MUSIG models for polydispersed bubbly flow [25] (each bubble size group is attached to a bubble/gas velocity distribution group), combined with fundamental one dimensional or point modelling of the gas(vapour/radiolytic gas)-liquid interface. This would help reduce some of the uncertainties associated with the gas-liquid area density as well as heat and mass transfer coefficients. The presence of both radiolytic gases and vapour substantially complicates this situation. However, detailed DNS and LES modelling may help to improve these parameterizations and our understanding of these processes.

References

- [1] M.M.R. Williams. A study of oscillatory behaviour events associated with boiling in the mips at level 1. Technical Report EA01084, Imperial College, 2011.
- [2] J. Dohler T.Schulenberg. Heating-up, nucleation and boiling of a critical solution of fissile material. *Int. J. Multiphase Flow*, 12:759–770, 1986.
- [3] C.C. Pain, C.R.E. de Oliveira, and A.J.H. Goddardand A.P. Umpleby. Transient criticality in fissile solutions – compressibility effects. *Nuclear Science and Engineering*, 138:78–95, 2001.
- [4] Y. Tsuji C. Crowe, M. Summerfield. *Multiphase flows with droplets and particles*. CRC Press, 1998.
- [5] J. Cortes. On the construction of upwind schemes for non-equilibrium transient two-phase. *Computers and Fluids*, 31:159–182, 2002.
- [6] J. Lavieille S. Mimouni, A. Foissac. Cfd modelling of wall steam condensation by a two-phase flow approach. *Nuclear Engineering and Design*, 26:1377–1387, 2010.
- [7] INL. *RELAP5-3D CODE MANUAL VOLUME I: CODE STRUCTURE, SYSTEM MODELS, AND SOLUTION METHODS*, Sep 2009.
- [8] Imperial College London. *FETCH-MIPS MANUAL*, Aug 2012.
- [9] A. Prosperetti. The equation of bubble dynamics in a compressible liquid. *Phys. Fluids*, 30:3626–3628, 1987.
- [10] T.R.Bott G.F. Hewitt, G.L. Shires. *Process Heat Transfer*. CRC Press, Inc., 1994.
- [11] D.E.Kornreich D.L.Hetrick, R.H.Kimland. Computer simulations of homogeneous water solution pulse reactors and criticality accidents. In *ANS Topical Meeting on Physics, Safety and Applications of Pulse Reactors*.
- [12] A.Bickley D.Mather and A. Prescott. Critex - a code to calculate the fission release arising from transient criticality in fissile solutions. Technical Report CS/R1007/R, AEA, 1994.
- [13] A.Bickley D.Mather and A. Prescott. Validation of the critex code. In *International Seminar on Nuclear Criticality Safety*.
- [14] A.Bickley D.Mather and A. Prescott. Examination of some fissile solution scenarios using critex. In *International Seminar on Nuclear Criticality Safety*.
- [15] D.Mather A.Bickley. Study of the phenomenology of an accidental criticality excursion capable of occurring during transport or storage of fissile materials in the form of a solution. Technical report.

- [16] A. Bensalem G. Yadigarogula. Interfacial mass generation rate modelling in non-equilibrium two-phase flow. *Multiphase Science and Technology*, 3:85–127, 1987.
- [17] S.S. Doerffer I.L. Pioro, W. Rohsenow. Nucleate pool-boiling heat transfer. ii: assessment of prediction methods. *International Journal of Heat and Mass Transfer*, 47:5045–5057, 2004.
- [18] J. G. Collier. *Convective Boiling and Condensation, second Edition*. McGraw Hill Book co., 1981.
- [19] C. Hirsch. *Numerical Computation of Internal and External Flows, vol 2: Computational methods for Inviscid and Viscous Flows*. John Wiley sons, 1984.
- [20] Chien Liu M.L. Greenfield, R.P. Lipkis and N. Zuber. Studies on density transients in volume-heated boiling systems. Technical Report 2950, AECU, 1954.
- [21] F. BARBRY. A review of the silene criticality excursions experiments. In *Proc. Topical Meeting on Physics and Methods in Criticality Safety*.
- [22] F. BARBRY. Fuel solution criticality accident studies with the silene reactor : Phenomenology, consequences and simulated intervention. In *International Seminar on Criticality studies programs and needs*.
- [23] ROZAIN JP. BARBRY, F. Formation of radiolysis gas and the appearance of a pressure increase during a criticality excursion in a fissile solution. In *Trans. Am. Nucl. Soc.*
- [24] F. BARBRY. Model to estimate the maximum fission yield in accidental solution excursions. In *Trans. Am. Nucl. Soc.*
- [25] E. Krepper H.M. Prasser D. Lucas T.h. Frank1, PJ. Zwart. Validation of cfd models for mono- and polydisperse air-water two-phase flows in pipes. Technical Report 2950, ANSYS Germany GmbH, 2006.